



# The Backward Silicon Track Trigger of the HERA Experiment H1

von

I. Tsurin



# The Backward Silicon Track Trigger of the HERA Experiment H1

## DISSERTATION

zur Erlangung des akademischen Grades  
**doctor rerum naturalium**  
(Dr. rer. nat.)

im Fach Physik

eingereicht an der  
**Mathematisch-Naturwissenschaftlichen Fakultät I**  
**der Humboldt-Universität zu Berlin**

von

**Ilya Petrovich Tsurin**

geboren am 25. Februar 1972 in Verhnaya Tura, UdSSR

Präsident der Humboldt-Universität zu Berlin  
**Prof. Dr. Jürgen Mlynek**

Dekan der Mathematisch-Naturwissenschaftlichen Fakultät I  
**Prof. Dr. Michael Linscheid**

Gutachter/innen:    **1. Prof. Dr. Hermann Kolanoski**  
                              **2. Prof. Dr. Christian Kiesling**  
                              **3. Prof. Dr. Nikolaj Pavel**

Tag der mündlichen Prüfung:    21 Oktober 2003



## Abstract

The Backward Silicon Tracker of the H1 experiment is being used in conjunction with a lead-fiber Calorimeter for detailed investigations of inclusive deeply inelastic scattering of leptons from protons,  $e^\pm P \rightarrow e^\pm X$ , and of charm production at small values of the Bjorken variable  $x$ ,  $x \leq 10^{-3}$ . In this thesis the development of a trigger for the Backward Silicon Tracker is described. The detector was installed in 2001 and started to operate in H1 after the HERA upgrade. Exploiting the low noise performance and fast time response of solid state semiconductors, a silicon pad detector telescope was developed for the first level trigger on tracks scattered in the backward region of the H1 detector. The design of the new trigger part of the BST consisting of silicon pad detectors and dedicated fast readout circuitry is described. Results of beam tests and first luminosity data are presented.

## Zusammenfassung

Die Dissertation beschreibt die Entwicklung eines Triggers für den Backward Silicon Tracker (BST). Der Detektor wurde im Jahre 2001 installiert und nach der Modifizierung von HERA zur Erreichung höherer Luminosität in Betrieb genommen. Der Backward Silicon Tracker des H1-Experiments wird in Verbindung mit einem Blei-Scintillationsfaser Kalorimeter zur detaillierten Untersuchung der inklusiven tief inelastischen Streuung von Leptonen an Protonen,  $e^\pm P \rightarrow e^\pm X$ , und der Charm-Erzeugung bei kleinen Werte der Bjorken Variable  $x$ ,  $x \leq 10^{-3}$  eingesetzt. Die guten Eigenschaften von Festkörper-Halbleitern, geringes elektronisches Rauschen und schnelle Signalantworten, wurden bei der Entwicklung des Silizium-Pad-Detektors zum Nachweis von Spuren in der Rückwärtsregion des H1-Experiments in der ersten Stufe des Triggersystems ausgenutzt. Der neue Triggerdetektor des BST, der Pad-Detektor und die dafür entwickelte Ausleseelektronik wie auch die implementierte Logik werden beschrieben. Resultate von Teststrahlungsmessungen und von ersten Messungen unter Luminositätsbedingungen an HERA-II werden dargestellt.

# Contents

<b>1</b>	<b>Introduction</b>	<b>6</b>
1.1	Inelastic Electron-Proton Collisions . . . . .	7
1.1.1	Kinematics of the $e^\pm P$ Scattering . . . . .	7
1.1.2	Deeply Inelastic Scattering Parameterisation . . . . .	9
1.1.3	Double-Differential Cross Section . . . . .	11
1.2	Experimentation at HERA . . . . .	12
1.2.1	Reconstruction of the Kinematic Variables . . . . .	12
1.2.2	Determination of the Structure Functions . . . . .	13
1.2.3	Background Suppression . . . . .	16
<b>2</b>	<b>The H1 Detector</b>	<b>19</b>
2.1	The H1 Experiment at HERA-II . . . . .	19
2.1.1	Calorimetry System . . . . .	21
2.1.2	Tracking System . . . . .	22
2.1.3	Luminosity and ToF Systems . . . . .	26
2.2	Data Taking Triggers . . . . .	27
2.2.1	Central Trigger . . . . .	27
2.2.2	Low $Q^2$ Triggers . . . . .	29
2.2.3	BST Triggering Concept . . . . .	31
2.3	Conclusion . . . . .	37
<b>3</b>	<b>The BST Trigger System</b>	<b>38</b>
3.1	Overview . . . . .	38
3.2	Detector Layout . . . . .	38
3.3	Detector Module . . . . .	39
3.3.1	Silicon Sensor . . . . .	40
3.3.2	Readout Chip . . . . .	41
3.3.3	PRO/A Chip Evaluation . . . . .	43
3.3.4	Pad Hybrid . . . . .	45
3.4	Front-end Interface . . . . .	46
3.4.1	Hardware Solutions . . . . .	47

3.4.2	Slow Control Processor . . . . .	48
3.4.3	Data Reduction Processor . . . . .	49
3.5	VME Interface Modules . . . . .	51
3.6	Power Supply System . . . . .	52
3.7	Operation Experience . . . . .	53
<b>4</b>	<b>Test Beam Results</b>	<b>55</b>
4.1	Beam Experiment . . . . .	56
4.1.1	Experimental Test Setup . . . . .	57
4.1.2	Electron Tagger . . . . .	58
4.1.3	Detector Alignment . . . . .	59
4.2	Measurement Programme . . . . .	61
4.2.1	Analog Amplitude Measurements . . . . .	61
4.2.2	Track Trigger Efficiency Studies . . . . .	63
4.2.3	Detector Calibration . . . . .	65
4.3	Conclusion . . . . .	66
<b>5</b>	<b>Data Analysis</b>	<b>67</b>
5.1	Single Plane Efficiency Studies . . . . .	68
5.1.1	Data Selection . . . . .	69
5.1.2	Fiducial Cuts . . . . .	69
5.1.3	Detector Alignment . . . . .	70
5.1.4	Efficiency Measurement . . . . .	74
5.2	Raw Data Analysis . . . . .	76
5.2.1	Data Readout . . . . .	76
5.2.2	Data Treatment . . . . .	77
5.3	DIS Trigger and Background Suppression . . . . .	79
<b>6</b>	<b>The H1 Radiation Monitor</b>	<b>82</b>
6.1	Radiation Sources in the Experiment . . . . .	82
6.2	Radiation Effects in the BST . . . . .	83
6.2.1	Silicon Sensors . . . . .	83
6.2.2	Readout Electronics . . . . .	84
6.3	Radiation Monitoring with Pads . . . . .	85
6.4	Further Applications for the BST-Pad . . . . .	88
6.5	Design Outlook . . . . .	90
<b>7</b>	<b>Summary</b>	<b>91</b>
<b>A</b>	<b>Subsystems of the BST-Pad</b>	<b>94</b>
A.1	Slow Control Subsystem . . . . .	94



A.1.1	PDS Control Functions . . . . .	94
A.1.2	Front-end Control Functions . . . . .	97
A.2	Data Reduction Subsystem . . . . .	105
A.2.1	Setting up the Front-end . . . . .	105
A.2.2	Setting up the Master Card . . . . .	108
A.2.3	Setting up the Repeater Card . . . . .	109
A.3	Technical documentation . . . . .	110
<b>B</b>	<b>Topological Trigger Data</b>	<b>112</b>
<b>C</b>	<b>HERA Background Control</b>	<b>115</b>



# Chapter 1

## Introduction

In 1964 the American physicists Murray Gell-Mann and George Zweig independently developed a theory of particle physics that proposed quarks as the building blocks of protons and neutrons [1]. According to the SU(3) internal symmetry scheme only two types of quarks, the up quark and the down quark, are needed for a static explanation of nucleons. Experiments conducted with high energetic colliding leptons and nucleons to probe the nucleon structure, table 1.1, supported the existence of quarks and explored their behaviour [2]-[5].

Table 1.1: Measurements of the nucleon structure functions.

Experiments	Beam	Target
E49,E61,E80,E87,E89, E130,E137,E139,E140, E142,E143,E154,E155 (SLAC)	$e$ (6..48) GeV	$H_2, D_2, {}^3He, Be, C,$ $Al, Ca, Fe, Ag, Au,$ $C_6O_4H_8, NH_3, C_2H_4$
BCDMS (CERN) NMC (CERN) EMC (CERN) SMC (CERN)	$\mu$ (100..280) GeV $\mu$ (90..280) GeV $\mu$ (100..280) GeV $\mu$ (100..190) GeV	$H_2, D_2, C, N_2, Fe$ $H_2, D_2, He, Li, C, Ca, Fe$ $H_2, D_2, C, Ca, Fe, Cu, Sn$ $H_2, D_2$
CCFR (Fermilab) E665 (Fermilab)	$\nu, \bar{\nu}$ (30..600 GeV) $\mu$ (470 GeV)	$Fe$ $H_2, D_2$
H1 (DESY) ZEUS (DESY) HERMES (DESY)	$e^\pm$ (27.5 GeV) $e^\pm$ (27.5 GeV) $e^\pm$ (27.5 GeV)	$p$ (920 GeV) $p$ (920 GeV) $H_2, D_2$

The advantage of electrons and positrons as probing tools in studying the proton structure is that these are elementary particles well understood in Quantum Electrodynamics (QED) and that their interactions with other fundamental, electrically charged particles, quarks in the quark parton model (QPM), are theoretically well defined.

Because of their stability and electric charge, electrons and positrons can be accelerated up to very high momenta which is important for deeper resolving the proton structure. The de Broglie wavelength of the probing particle,  $\lambda = h/p$ , must be much less than 1 fm that corresponds to a particle momentum greater than 1 GeV. Under this impact the nucleon target is likely to disintegrate, therefore the  $e^\pm P$  scattering at high energies shows an inelastic character.

## 1.1 Inelastic Electron-Proton Collisions

### 1.1.1 Kinematics of the $e^\pm P$ Scattering

At HERA [6] electrons (positrons) of energy  $E_l = 27.5$  GeV collide head-on with protons of energy  $E_P = 920$  GeV. The initial four-momentum of the lepton  $k \equiv (E_l, p_{x,l}, p_{y,l}, p_{z,l})$  is equal to  $(E_l, 0, 0, -E_l)$  neglecting the rest mass of the particle. On the other hand the initial four-momentum of the nucleon  $P \equiv (E_P, p_{x,P}, p_{y,P}, p_{z,P})$  obtains values  $(E_P, 0, 0, E_P)$  and the beam center-of-mass energy (CME)  $\sqrt{s}$  reaches large values,

$$\sqrt{s} = \sqrt{(k + P)^2} \approx \sqrt{4E_l E_P} = 318 \text{ GeV}, \quad (1.1)$$

which makes HERA a collider at the highest energy frontier. The  $e^\pm P$  interaction proceeds via the exchange of a virtual vector boson, as shown in fig. 1.1. The reaction mechanism uses a term "charged current" (CC) when it is mediated by  $W^\pm$  gauge bosons, otherwise it is called "neutral current" (NC) when the force carriers are virtual  $Z^0$  bosons or virtual  $\gamma$ -quanta. In these processes the lepton number has to be conserved. The neutrino (anti-neutrino) from the CC event or the scattered electron (positron) from the NC process is produced with a momentum  $k' \equiv (E'_l, p'_{x,l}, p'_{y,l}, p'_{z,l})$ . The proton fragments into a set of hadrons  $X$ ,  $e^\pm P \rightarrow l' X$ , only governed by the conservation laws.

One straightforward way to measure the proton structure is inclusive analysis of the recoil electrons (positrons) in the single-photon exchange mechanism which is dominant in the inelastic reactions. The kinematics of inclusive events is described by the following Lorentz invariant quantities:

$$Q^2 = -(k - k')^2, \quad y = \frac{P \cdot (k - k')}{P \cdot k}. \quad (1.2), (1.3)$$

Here  $Q^2$  is the mass squared of the virtual exchanged photon. The minus sign of this parameter (eq. 1.2) denotes its virtuality and the absolute value varies within the range  $0 < Q^2 < s$ . In the limit  $Q^2 \rightarrow 0$  the photon is almost real. This is the analogy to the de Broglie wavelength of the probing particle or, in other words, the resolving power of the interaction. The deep-inelastic region is defined by  $Q^2 > M_p^2$ , the square of the rest mass of the proton. The vector  $(k - k') = q$  defines the four-momentum transfer from the electron (positron) to the hadronic system. In the rest frame of the proton:  $\tilde{P} = (M_P, 0, 0, 0)$ ,  $\tilde{k} \approx (\frac{2E_P E_l}{M_P}, 0, 0, -\frac{2E_P E_l}{M_P}) = (\tilde{E}_l, 0, 0, \tilde{p}_{z,l})$  and respectively  $\tilde{k}' \approx (\tilde{E}_l', \tilde{p}_{x,l}', \tilde{p}_{y,l}', \tilde{p}_{z,l}')$ , the variable  $y$  can be rewritten as:  $y = 1 - \tilde{E}_l'/\tilde{E}_l$ . It acquires the meaning of the relative energy transfer and stands for a measure of inelasticity of the process.

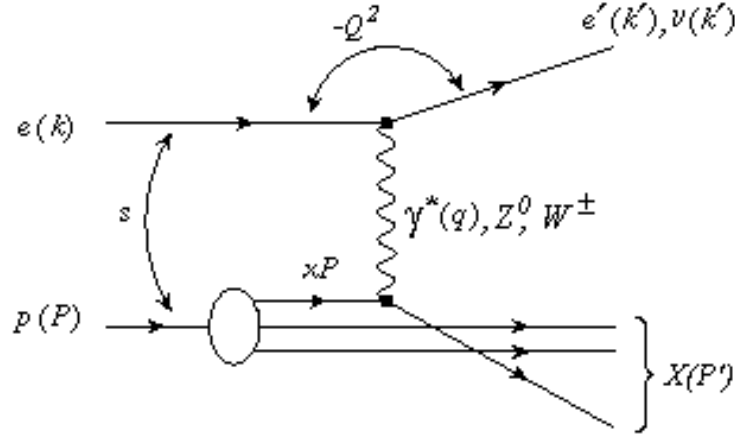


Figure 1.1: Schematic diagram for the inelastic  $eP$  scattering.  
The four-vectors of particles are given in parantheses.

Another variable, called Bjorken  $x$ , is defined as the ratio of the four-momentum and the energy transfer in the proton rest frame:

$$x = \frac{Q^2}{2y P \cdot k} = \frac{Q^2}{2P \cdot (k - k')}. \quad (1.4)$$

In the QPM it corresponds to the fraction of the proton momentum carried by the quark which took part in the interaction. By convention  $x$  and  $Q^2$ , besides the CMS energy  $s$ , are used to describe the inclusive scattering process. The kinematic region available in these variables for several deep inelastic scattering (DIS) experiments at low  $Q^2$  is shown in fig. 1.2.

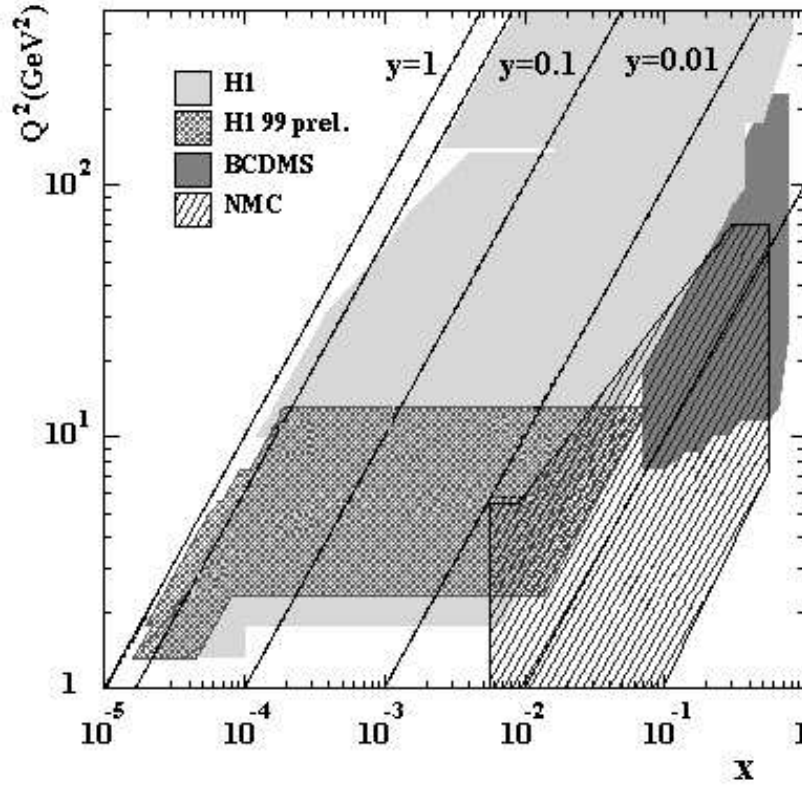


Figure 1.2: The  $x, Q^2$  kinematic plane for H1 and fixed target muon-proton experiments for studies of the nucleon structure.

### 1.1.2 Deeply Inelastic Scattering Parameterisation

An important assumption of the QPM is that the cross section for deeply inelastic scattering is a sum over individual parton interactions with the probe. Conservation of the total momentum of the proton leads to the expectation:

$$\varepsilon = \sum_q \int_0^1 x f_q(x) dx = 1, \quad q = u, d, \dots \quad (1.5)$$

where  $f_q(x)$  are the probabilities of finding  $u$  or  $d$  quarks with their fractional momenta between  $x$  and  $x + dx$ . The parton momentum density distributions  $f_q(x)$  are not determined by the QPM and the  $x$ -dependence of the DIS cross section must be directly measured. Integration over the experimental data, however, gave the result  $\varepsilon \approx 0.5$  [7]. The missing part of the proton's momentum is spread over neutral gluons which are the carriers of the strong nuclear interactions between the quarks and don't experience the electromagnetic force.

The emission of gluons and their splitting into quark-antiquark pairs is described by perturbative Quantum Chromodynamics (pQCD). It deals with the forces in a field where the interaction potential is proportional to a strong coupling constant  $\alpha_s = g_s^2/4\pi$ , where  $g_s$  is analogous to the charge  $e$  of QED. A special property of this field is that its quanta, the gluons, may directly interact with each other. This leads to a logarithmically decreasing function  $\alpha_s(Q^2)$  of  $Q^2$  for all quark flavours:

$$\begin{aligned} \alpha_s(Q^2) &\simeq \alpha_s \left\{ 1 - \frac{7\alpha_s}{4\pi} \cdot \log \left( \frac{Q^2}{Q_0^2} \right) + \left[ \frac{7\alpha_s}{4\pi} \cdot \log \left( \frac{Q^2}{Q_0^2} \right) \right]^2 + \dots \right\} \simeq \\ &\simeq \frac{\alpha_s}{1 + (7\alpha_s/4\pi) \cdot \log(Q^2/Q_0^2)} \equiv \frac{1}{(7/4\pi) \cdot \log(Q^2/Q_0^2)}, \end{aligned} \quad (1.6)$$

where the  $Q_0^2$  is a suitably chosen reference scale. The probability that the quark carrying momentum  $yp$  emits a gluon, leaving itself with momentum  $xp$  ( $0 \leq x \leq y \leq 1$ ), fig. 1.3, can be written as a power series of  $\alpha_s(Q^2)$ :

$$P(z, \alpha_s(Q^2)) = \frac{\alpha_s}{2\pi} P^{(0)}(z) + \left( \frac{\alpha_s}{2\pi} \right)^2 P^{(1)}(z) + \dots, \quad z = \frac{x}{y} \quad (1.7)$$

The pQCD theory allows probability computations for these quantum-mechanical sub-processes and their evolutions with the momentum of the probe  $Q^2$ , currently up to next to next to leading order of the splitting functions  $P^{(2)}(z)$ .

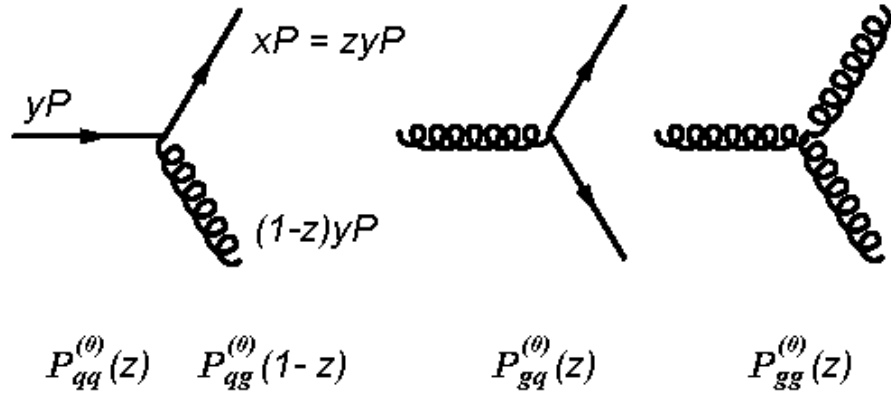


Figure 1.3: The leading-order QCD diagrams for quark and gluon sub-processes. Quarks,  $q$ , and gluons,  $g$ , are shown by straight and curly lines, respectively.

$$P_{q \rightarrow q}^{(0)}(z) = \frac{4}{3} \cdot \frac{1+z^2}{1-z^2}, \quad P_{q \rightarrow g}^{(0)}(z) = \frac{4}{3} \cdot \frac{1+(1+z^2)}{z} \quad (1.8), (1.9)$$

$$P_{g \rightarrow q}^{(0)}(z) = \frac{1}{2} \cdot (z^2 + (1-z)^2) \quad (1.10)$$

$$P_{g \rightarrow g}^{(0)}(z) = 6 \left( \frac{z}{1-z} + \frac{1-z}{z} + z(1-z) \right) \quad (1.11)$$

Thus the corrections to the universal proton momentum include a replacement  $\alpha_s \rightarrow \alpha_s(Q^2)$ , factorisation and a sum over all hadron constituents: quarks, gluons and antiquarks. The leptons not only scatter from the "valence" quarks of the proton, but also from the so-called "sea" of the quark-antiquark pairs which are created by the interaction itself. The total momentum of the probing particle must be divided between the quark and the gluon, leaving the quark with a lower fraction of the total proton momentum.

As the momentum of the probe increases further and its resolving distance becomes more minute, it may see the gluon radiated by the valence quark dissociating into a quark-antiquark pair from the vacuum sea. There will appear more quarks carrying very low fraction of the total proton momentum. The important result of the quark-gluon interactions is that the effective parton distributions depend also on  $Q^2$  when the quantities  $x$  and  $Q^2$  are evolved separately. At HERA it was discovered that the density at low  $x$  is very large [4], [5].

### 1.1.3 Double-Differential Cross Section

The DIS cross-section represents a quantum-mechanical probability of the nucleon interaction multiplied by a flux of virtual bosons. The main measurement of the experiments regards the variation of the cross section with the energy lost by the lepton during the collision and the angle through which the incident lepton is scattered. By selecting the outgoing lepton energy and the angle it is possible to vary  $Q^2$  and  $x$  (see section 1.2.1), thus sampling the parton distributions. For electromagnetic interactions of unpolarized electrons (positrons) and unpolarized protons the double differential cross-section, up to higher order corrections in QED, has a form:

$$\frac{d^2\sigma}{dx dQ^2} = \frac{4\pi\alpha^2}{xQ^4} \left[ 2xF_1(x, Q^2) \frac{y^2}{2} + F_2(x, Q^2)(1-y) \right], \quad (1.12)$$

which follows from four fundamental properties of electromagnetic interactions: Lorenz invariance, unitarity, gauge invariance and parity conservation. The unknown functions  $F_1(x, Q^2)$  and  $F_2(x, Q^2)$  are called the structure functions of the proton. The partonic expression of the structure functions is



found by adding all possible combinations of quarks and antiquarks involved in the reaction, weighted with their electric charges squared:

$$F_1 = \frac{1}{2} \sum_q e_q^2 (f_q(x) + f_{\bar{q}}(x)) \quad (1.13)$$

$$F_2 = x \sum_q e_q^2 (f_q(x) + f_{\bar{q}}(x)) \quad (1.14)$$

The sum extends over all quark and antiquark flavours. The difference  $F_2 - 2xF_1$  is named the longitudinal structure function  $F_L$  which is proportional to the absorption cross section  $\sigma_L$  of longitudinally polarized virtual photons. The function  $F_2$  contains both the transverse  $\sigma_T$  and the longitudinal  $\sigma_L$  polarization states. The double-differential cross section scaled down by a factor  $k = \frac{2\pi\alpha^2 Y_+}{xQ^4}$ , where  $Y_+ = 1 + (y - 1)^2$ , is known as the reduced cross section:

$$\sigma_r(x, Q^2) = F_2(x, Q^2) - \frac{y^2}{Y_+} F_L(x, Q^2). \quad (1.15)$$

The determination of  $F_2$  and  $F_L$  at HERA has been a major and the primary scientific task. Measurement of those functions is crucial for understanding physics at low  $x$ , i.e. the structure of high parton densities, up to high  $x$  where valence quarks determine the structure of the proton.

## 1.2 Experimentation at HERA

### 1.2.1 Reconstruction of the Kinematic Variables

There is a number of methods used by HERA experiments for the  $x$  and  $Q^2$  measurements [8]. The colliding-beam detectors H1 and ZEUS have an almost  $4\pi$  geometrical acceptance and they resolve both the leptonic and the hadronic final states.

In the **electron method** [9] the kinematic variables  $y$  and  $Q^2$  are calculated through the energy  $E'_e$  of the scattered electron (positron) and its polar angle  $\theta_e$  with respect to the proton beam direction:

$$y = 1 - \frac{E'_e}{E_e} \sin^2 \frac{\theta}{2}, \quad \frac{\Delta y}{y} = \frac{y-1}{y} \cdot \frac{\Delta E'_e}{E'_e} \oplus \frac{1-y}{y} \cdot \cot \frac{\theta}{2} \Delta \theta \quad (1.16), (1.17)$$

$$Q^2 = 4E_e E'_e \cos^2 \frac{\theta}{2}, \quad \frac{\Delta Q^2}{Q^2} = \frac{\Delta E'_e}{E'_e} \oplus \tan \left( \frac{\theta}{2} \right) \cdot \Delta \theta \quad (1.18), (1.19)$$

The third quantity, Bjorken  $x$ , can be found from the following relation neglecting the rest masses of the proton and the electron (positron):

$$x = \frac{Q^2}{ys}, \quad \frac{\Delta x}{x} = \frac{1}{y} \cdot \frac{\Delta E'_e}{E'_e} \oplus \left( \tan \frac{\theta}{2} + \frac{1-y}{y} \cdot \cot \frac{\theta}{2} \right) \cdot \Delta \theta \quad (1.20), (1.21)$$

The component  $\tan(\theta/2)$  causes large  $x$  and  $Q^2$  uncertainties at electron scattering angles  $\theta_e \rightarrow 180^\circ$  with respect to the proton beam. A precise electron track measurement in this geometry becomes essential, therefore.

The reconstruction accuracy in this method relies largely on the electron energy measurement. The bremsstrahlung in the initial and/or in the final states or emission of additional virtual photons leads to a lowering of the electron energy. The electron method is most influenced by the radiation effects since it uses the information about the scattered electron only. However, the energy-momentum balance, from the so-called  $E - p_z$  variable, is required to be fulfilled. This largely reduces the radiative corrections which are applied using Monte Carlo techniques. The main problem of the electron method is the resolution divergence  $\sim 1/y$  towards low  $y$ .

For charged current DIS in which the neutrino produced can not be detected and for neutral current DIS at low  $y$  the **hadron method** is used for kinematic reconstruction. It relies on the recognition of the final state hadrons, which are represented by tracks and/or characteristic energy losses. This method was refined for combined use of electron and hadron information.

Every reconstruction technique is effective in a certain kinematic region where it provides better accuracy. In order to optimize the resolution of the kinematic variables in the broadest range a combination of several methods is often used.

### 1.2.2 Determination of the Structure Functions

In most of the kinematic range the reduced cross section  $\sigma_r(x, Q^2)$  is given by  $F_2(x, Q^2)$ . The contribution of the  $F_L(x, Q^2)$  is small or negligible because of the quadratic  $y$  term in formula (1.15) and since  $F_L \leq F_2$ . Thus for low  $y$  the DIS measurement can be directly interpreted as a determination of the  $F_2$  structure function.

The double-differential cross section is found as a number of DIS events originating in certain region of  $x$  and  $Q^2$ , so-called "bin", on the kinematic plane divided by the total number of  $e^\pm P$  interactions given by the HERA luminosity. A variable bin size is chosen to be larger than the resolution of the kinematic variables. The statistical error in every bin should be smaller

than the systematic uncertainty where the latter depends, in particular, on the trigger efficiency.

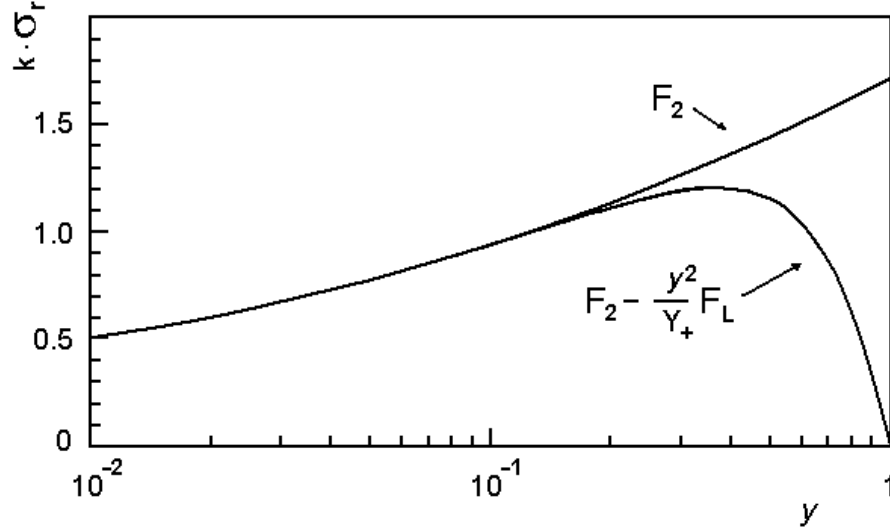


Figure 1.4: Influence of  $F_L$  on the DIS reduced cross section  $\sigma_r$ .  
The  $\sigma_r$  range at large  $y$  represents the extreme assumptions  $F_L = 0$ , upper curve, or  $F_L = F_2$ , lower curve.

In the high  $y$  region, the  $F_L$  part of the reduced cross section becomes comparable to the  $F_2$  value, see fig. 1.4. Their separate measurement is possible by changing the center of mass energy while keeping  $x$  and  $Q^2$  constant. From the definitions

$$F_L(x, Q^2) = \frac{Q^2}{4\pi^2\alpha} \sigma_L(x, Q^2) \quad (1.22)$$

$$F_2(x, Q^2) = \frac{Q^2}{4\pi^2\alpha} (\sigma_T(x, Q^2) + \sigma_L(x, Q^2)) \quad (1.23)$$

one can find the DIS cross section:

$$\sigma = \Gamma(y)(\sigma_T + \epsilon(y)\sigma_L), \quad (1.24)$$

where  $\Gamma(y) = \alpha Y_+ / (2\pi Q^2 x)$  stands for the flux factor of virtual photons with the ratio  $\epsilon(y) = 2(1-y)/Y_+$  for transverse and longitudinally polarized quanta where  $\sigma_T$  and  $\sigma_L$  define their absorption cross sections. The cross section for fixed  $x$  and  $Q^2$  is expected to depend lineary on  $\epsilon(y) \equiv \epsilon(s)$  according to formula (1.20). Thus one can fit the ratio  $R$  and extract  $F_2$  from:

$$R = \frac{\sigma_L}{\sigma_T} = \frac{F_L}{F_2 - F_L} \quad (1.25)$$

In experiments with a non-variable beam energy a model is needed for the  $R(x, Q^2)$  in order to obtain  $F_L(x, Q^2)$  or  $F_2(x, Q^2)$  [10], which are given by formulas:

$$F_2(x, Q^2) = \frac{\sigma_r}{1 + \frac{y^2}{1 + R(x, Q^2)}} \quad (1.26)$$

$$F_L(x, Q^2) = \left( F_2(x, Q^2) - \sigma_r \right) \frac{y^2}{Y_+} \quad (1.27)$$

The measurement error is then a superposition of the systematic, statistical and parameterization errors. In the absence of data with varied beam energy at HERA the well known behaviour of  $F_2$  was extrapolated to lowest  $x$  or high  $y$ , i.e.  $F_2 = F_2^{extrap.}$  in equation (1.27). This allows to interpret the  $\sigma_r$  data as a measurement of  $F_L$  at lowest  $x$ . A recent result [11] for the structure function measurements by H1 is shown in fig. 1.5 for  $F_2(x, Q^2)$  and in fig. 1.6 for  $F_L(x, Q^2)$ .

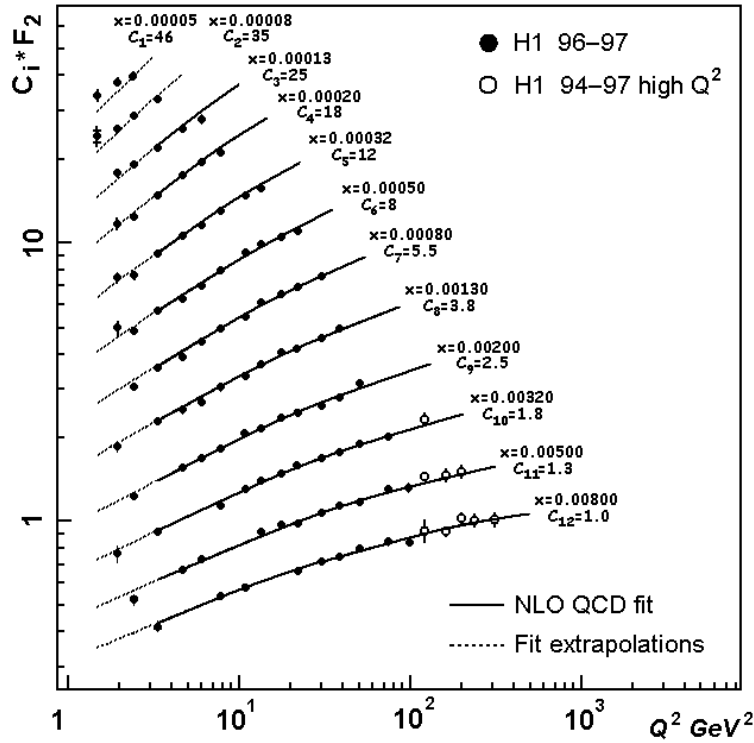


Figure 1.5: Low- $x$  measurements of  $F_2(x, Q^2)$  in a wide range of  $Q^2$ .  $F_2$  is large and rises steeply with  $Q^2$  at low  $x$ , i.e. in this region the parton ( $q$  and  $g$ ) densities are large. The behaviour of  $F_2$  can be described by perturbative QCD.

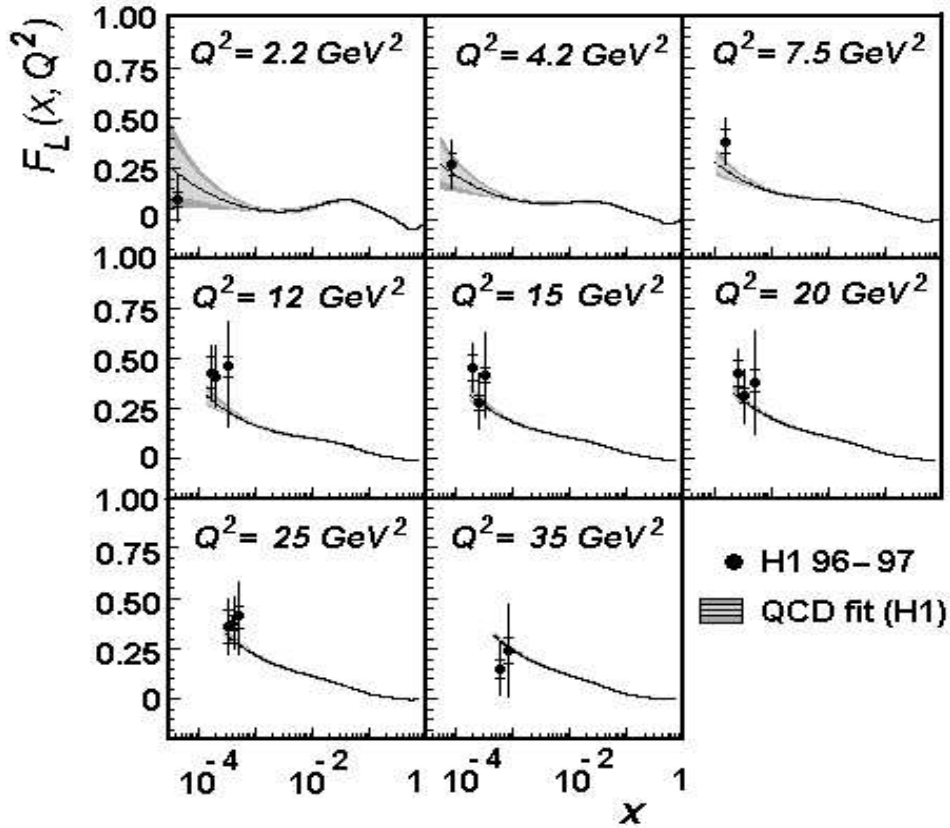


Figure 1.6: The longitudinal structure function  $F_L(x, Q^2)$  as measured by the H1 experiment at low  $x$ . The curves represent a prediction of  $F_L$  from perturbative QCD calculations based on the H1 data on the other structure function,  $F_2$ .

### 1.2.3 Background Suppression

According to the formula (1.12) the DIS cross section has a  $1/Q^4$  dependence. Therefore most leptons scatter at low angles from their incident direction. Often they are lost in the beam pipe – the leakage of particles along the beam axes is unavoidable. There are several processes concurrent to DIS which can mimic the electron in a sample of DIS events.

A large background component arises from  $\gamma\gamma$  decays of the lightest meson,  $\pi^0$ , produced during the hadronization of the nucleon final state. With some probability these  $\gamma$ -quanta are detected directly in calorimeters but often they convert into  $e^+e^-$  pairs in the detector material. Some part of electromagnetic signals produced by  $\pi^0 \rightarrow \gamma\gamma$  decays can be filtered out controlling the opening angle between two photons which is a function of the initial meson momentum.

The electron and the positron can emit bremsstrahlung photons resulting in new cascades. Knowledge of the longitudinal and transverse profiles of electron-photon showers allows their suppression since hadrons produce broader energy clusters. Monte Carlo event simulations are used in developing the data selection cuts. Most of the  $\pi^0$  contamination, however, is not resolved with the calorimeter. Requirement of a track close to the vertex region which is associated to a calorimeter cluster becomes very effective in reducing the neutral background component.

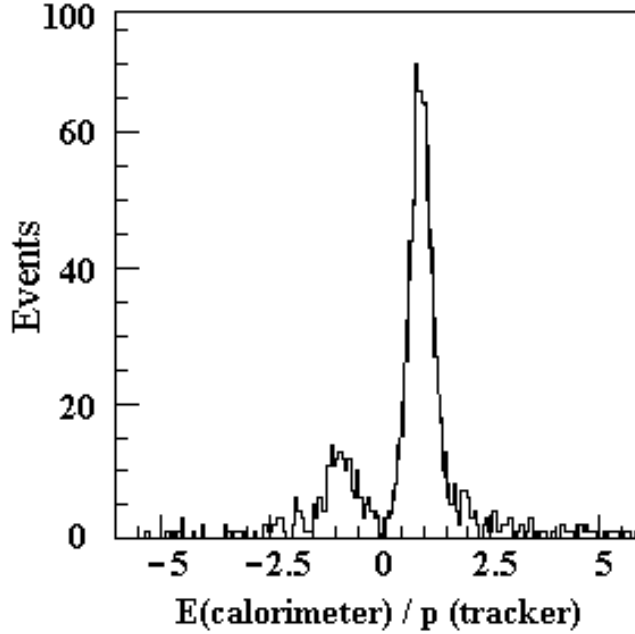


Figure 1.7: Comparison of the particle energy in the backward calorimeter of H1 with the track momentum measurement using the Backward Silicon Tracker [12]. The sign of the result corresponds to positively or negatively charged particles.

The track requirement reduces part of the neutral background. A further background source is due to the fact that sometimes it is difficult to distinguish between the scattered lepton and the hadron because their signals are too similar. False tracks are mostly related to the charged hadronic particles. An efficient method of eliminating the remaining background is based on the determination of the particle charge. All those tracks which are opposite electrically to the expected leptons, can be removed, fig. 1.7. The same fraction of unipolar events can be subtracted statistically assuming the charge symmetry of the background.

Another source of false DIS signatures is a beam-induced background.

High multiplicity tracks are produced in the interactions of accelerated particles with residual gas molecules. Off-beam orbit protons may scatter off the beam-line elements and hit the detector. Opposed to low  $x$  DIS, such events have often a very high particle multiplicity that can be measured and exploited online for the background rejection.

A rather high power of the synchrotron radiation is emitted by electrons (positrons) due to their transverse acceleration in the bending sections and focusing magnets of the HERA machine. The non- $e^\pm P$  background is run-dependent, therefore some number of so-called "pilot" HERA bunches are left unpaired (i.e. the corresponding bunch in the other beam is empty) for its studies. A ratio between the number of colliding  $n_{colliding}$  and pilot  $n_{pilot}$  bunches gives an approximation:

$$N_{total}^{bg} = \frac{n_{colliding}}{n_{p-pilot}} N_{p-pilot}^{bg} + \frac{n_{colliding}}{n_{e-pilot}} N_{e-pilot}^{bg} + \frac{n_{colliding}}{n_{empty}} N_{empty}^{bg} \quad (1.28)$$

Thus the integral of the DIS events can be corrected. It requires keeping the information about every bunch crossing for the further data processing:

- Timing cuts to reject events coming from upstream interactions of the proton and/or lepton;
- Track validation and event vertex reconstruction within a defined range;
- Linking data from tracking detectors and calorimeters;
- Controlling the particle multiplicity for every event.

All these tasks can be implemented into the hardware.

# Chapter 2

## The H1 Detector

### 2.1 The H1 Experiment at HERA-II

The integrated luminosity delivered by HERA-I for the H1 and ZEUS experiments in the period from 1994 to 2000 was approximately  $140 \text{ pb}^{-1}$  including both, the positron and the electron beams, fig. 2.1. The luminosity upgrade program of HERA [13] should provide  $1 \text{ fb}^{-1}$  over about 5 years with an instantaneous peak luminosity of  $5 \cdot 10^{31} \text{ cm}^{-2}\text{s}^{-1}$ . With larger data sets the proton structure function  $F_2$  can be measured to higher precision allowing extraction of the quark and gluon densities with an experimental precision of 1% [14].

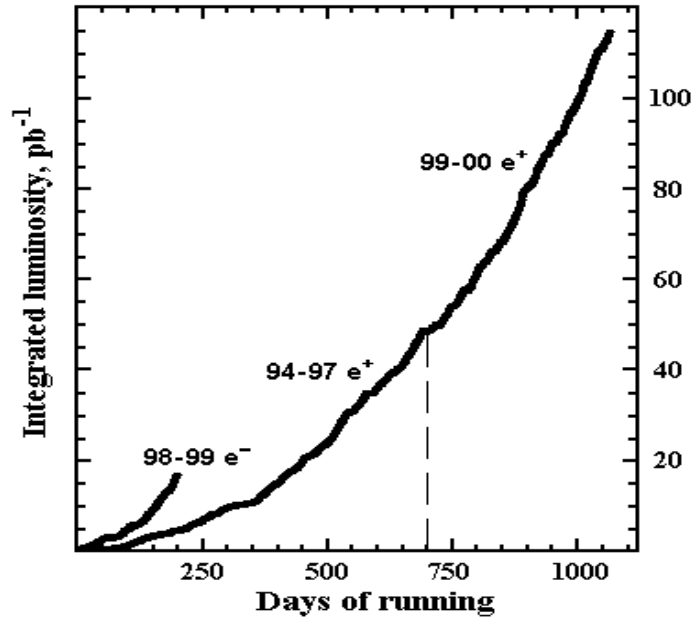


Figure 2.1: The cumulative luminosity for the H1 and ZEUS detectors in the first running period of HERA.



A major upgrade of the HERA machine in 2001 resulted in the modification of the interaction regions (IR) inside the H1 and ZEUS detectors. Two superconducting magnets, *GG* and *GO*, were installed next to the interaction point (IP), fig. 2.2, to focus the leptonic beam stronger to achieve a spot size of  $120 \times 30 \mu\text{m}^2$ . The electrons (positrons) deflected near the IP emit up to 13 kW of the synchrotron radiation (SR). This power can not be absorbed inside the detector, therefore geometry apertures of the beam tube are arranged such that the SR fan passes the detector with very small losses.

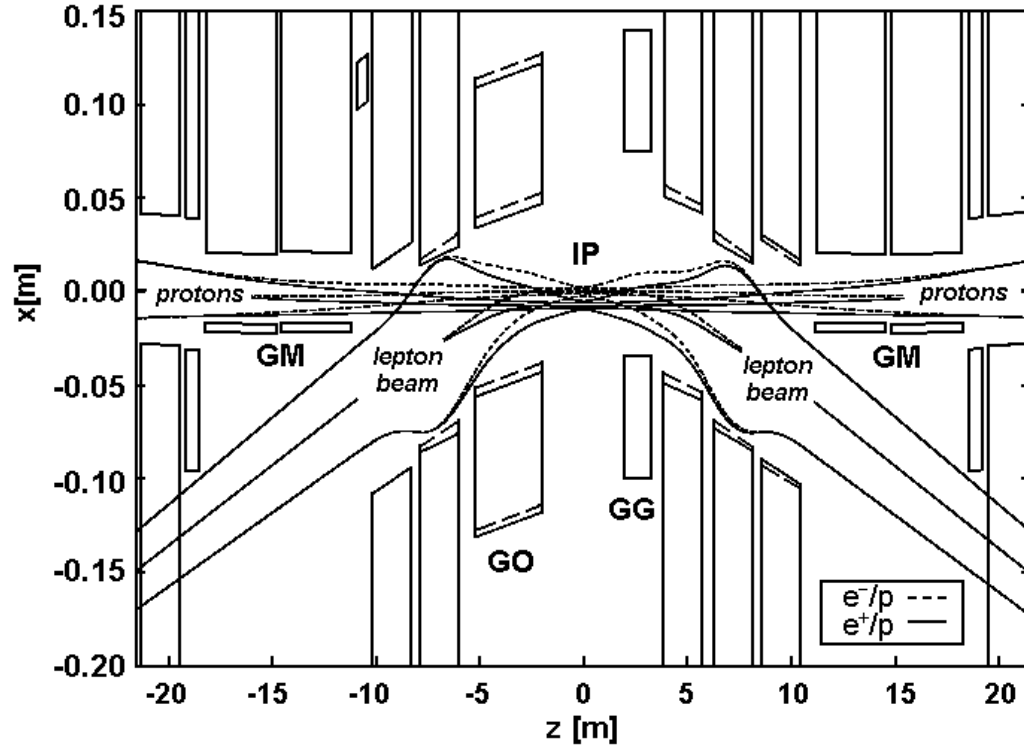


Figure 2.2: Layout of the interaction region of the H1 in the HERA coordinate system. Solid and dashed lines show the  $e^+$  and  $e^-$  beam envelopes and their corresponding magnet positions.

The final focusing magnets *GM* for the proton beam were shifted towards the IP from 26 meters in the original design [15] to 11 meters distance. Because of much higher momenta of protons the final state particles are spread mostly close to the proton beam direction. To register them accurately the H1 facility has an asymmetric layout with more equipment placed in their direction. By convention this part of the H1 detector is called the "forward" region. The opposite, "backward" region and the central part, fig. 2.3, are instrumented to detect both the hadrons and scattered leptons.

The cross section measurement for the low  $Q^2$  events relies mainly on the

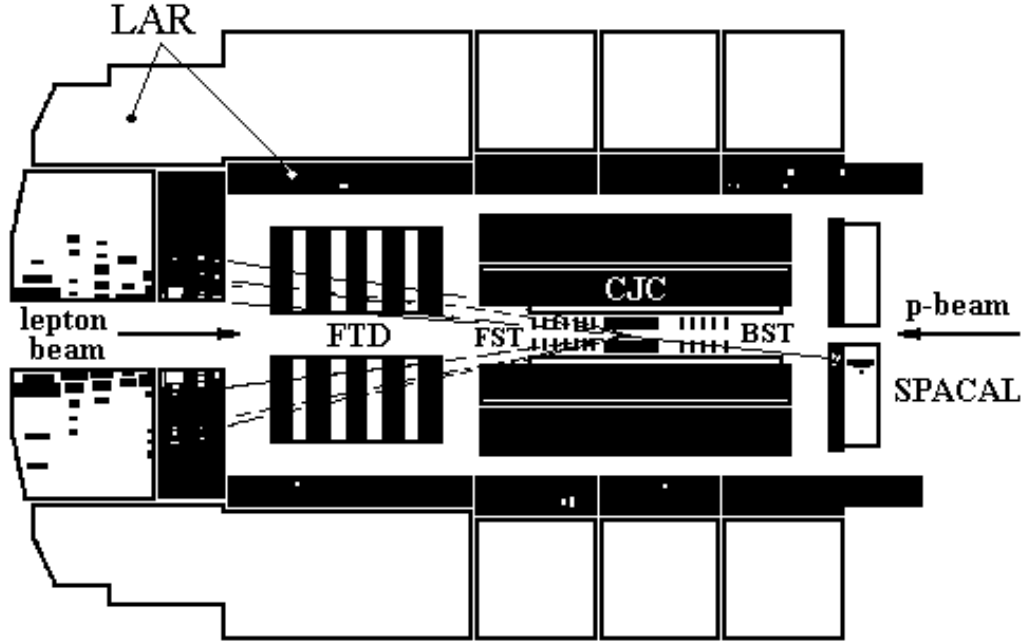


Figure 2.3: The major components of the H1 detector used for the DIS measurements at HERA-II: LAr (Liquid Argon calorimeter), SPACAL (lead/scintillating-fibre calorimeter), FTD (forward tracking device), CJC (central jet chamber), BST (backward silicon tracker).

Liquid Argon calorimeter [16], the backward calorimeter SPACAL [17] and central and backward tracking systems [18], [19]. The H1 detector combines nearly hermetic calorimetry with tracking in a solenoidal magnetic field of 1.15 Tesla.

### 2.1.1 Calorimetry System

The scattered electron or positron can be registered in the SPACAL or in the LAr calorimeters with relative energy resolution:  $\sigma_E/E \simeq 7\%/\sqrt{E/GeV} \oplus 1\%$  and  $10\%/\sqrt{E/GeV} \oplus 1\%$  respectively. The SPACAL has a high transverse granularity and provides a determination of the spatial coordinates of electromagnetic clusters with  $\sigma_{x,y} \simeq (4.4/\sqrt{E/GeV} \oplus 1)$  mm precision.

The hadronic final state energy is measured in the LAr calorimeter with about  $50\%/\sqrt{E/GeV} \oplus 2\%$  accuracy. The calorimeter has a non-compensating design (the detector response is not equivalent for different components of hadronic showers), therefore some special corrections are used to re-weight signals for the proper jet energy reconstruction [20]. Weighting functions are

obtained from the Monte Carlo jet simulation and from calibration measurements [21]. For hadrons in the backward region of H1 the SPACAL provides approximately  $\sigma_E/E \simeq (56 \pm 3)\%$  energy resolution.

The SPACAL physical trigger [22] on leptons is based on the analog energy sum compared to three energy thresholds adjustable in the range between  $\sim 100$  MeV and  $\sim 20$  GeV. The fast timing response of the SPACAL scintillation counters and the relatively good timing resolution,  $\sigma_t = (0.38 \pm 0.03)$  ns, of the photomultiplier tubes (PMT) allow the time-of-flight (ToF) measurements to veto beam induced background already at the first trigger level [23].

Trigger signals for leptons and hadrons in the LAr calorimeter are derived from the digitized energy sums in the detector cells. Programmable look-up tables are used to build up various final trigger elements for needs of different physics topologies. An upgrade program for the existing LAr trigger [24] is underway with the aim to trigger on localized energy depositions in the calorimeter - "jets".

The measurement of inelastic events needs an inclusive trigger on scattered charged leptons. For accurate analyses of DIS the trigger has to have minimum bias conditions, because the result relies merely on the lepton candidate and is free of uncertainties connected with the hadronic final state. At low  $Q^2 \leq 150$  GeV<sup>2</sup> this means triggering with adjustable SPACAL energy thresholds. As discussed above, the high sensitivity to small energies requires efficient background suppression techniques using topological and tracking information. Dedicated track triggers are worked out and used for photoproduction events

### 2.1.2 Tracking System

The tasks of the H1 tracking detectors are to trigger on charged particles, to reconstruct their tracks and vertices and to measure the particle's momenta. The trajectories of charged particles moving in a homogeneous toroidal magnetic field are helices which can be described using a set of five variables. Every sub-detector uses its own techniques to determine these parameters. Tracks which have a substantial transverse  $p_t$  momentum are registered in the central trackers: COP, CIP (the outer and the inner proportional chambers) and also CJC1, CJC2, COZ (drift chambers) all of which are arranged concentrically around the beam pipe.

Tracks with a high  $p_z$  component can be detected in the forward and backward chambers (FTD and BDC) whose planes are oriented perpendicular to the beam axis. These forward and backward tracking detectors were upgraded during the HERA shutdown in 2000-2001. A special role is given to the newly designed forward silicon tracker (FST) and the upgraded cen-

tral and backward silicon detectors, the CST and the BST, for precise track measurements as they are devices closest to the interaction region.

### Forward and Central Trackers

Triggering over the large solid angle is based on multi-wire proportional chambers which provide fast signals with their timing resolutions better than the bunch crossing interval. The COP and the CIP detectors provide a sub-trigger for events with vertices inside the nominal interaction region. These are cylindrical multi-layer detectors with a laminar - "pad" structure for each slice (the COP has a coarse granularity) covering in  $\theta$  the range from  $10^\circ$  to  $170^\circ$  (the best estimation for the CIP is given). Their purposes are:

- to provide a calorimeter independent track trigger;
- to define rays of charged particles from the interaction region and link these rays with the calorimeter trigger;
- to suppress multitrack events from beam-gas or beam-wall interactions outside the  $e^\pm P$  interaction region by a fast z-vertex reconstruction method.

Their reconstruction algorithm relies on calculations of the intercept with the beam axis for all possible track patterns. The number of candidates is histogrammed in several bins along the interaction region. The trigger is activated when the bin content exceeds certain threshold. A 16-fold division of the vertex range provides the minimum bin width of about 5 cm [25].

The forward proportional chambers were linked logically to the vertex trigger for the determination of forward rays coming from the interaction region. During the forward drift detector (FTD) upgrade [26] the removal of its multiwire proportional chambers for triggering is partially compensated by scintillating counters.

The high  $Q^2$  scattered lepton and/or charged leptons from the hadronic decays traverse already half a radiation length of material before entering the FTD. This leads to reconstruction efficiency losses. The accuracy of the momentum measurement [27] for particles degrades due to their multiple coulomb scattering. Thus a new forward silicon tracker (FST) was built and positioned in front of the FTD at low angles, see fig. 2.3. The identification of the scattered lepton in the forward region of the H1 is thus eased and became possible imposing the calorimeter cluster-track link prior to the dead material.

The FST consists of 6 wheels of silicon micro-strip detectors. The distance between strips amounts to  $25\ \mu\text{m}$ . The analog readout of every third strip

allows measurements of space points with  $\sigma_r = 7.2 \mu\text{m}$  precision for track residuals – deviations of measured track coordinates from their best-fit curve. The transverse momentum resolution of the FST  $\sigma_{p_t}/p_t^2$  was estimated of the order of  $4\% \text{ GeV}^{-1}$ . This is worse than of FTD, because the silicon tracker has smaller level arm in the  $x$ - $y$  ( $r$ - $\phi$ ) plane for helix measurements. The combined FST-FTD momentum resolution reaches, nevertheless, about  $2\% \text{ GeV}^{-1}$  [28].

The central outer drift chamber COZ performs measurements of the  $z$ -coordinate of the track much more precise,  $\sigma_z = 300 \mu\text{m}$ , than achieved by charge division of the CJC signals (2 cm). Usage of the central silicon tracker offers a  $12 \mu\text{m}$  accuracy in  $r$ - $\phi$  coordinates and  $22 \mu\text{m}$  in  $z$ -coordinate definition. This, together with the forward and the backward silicon trackers, provides a good efficiency for detecting hadrons with decay length of a few hundred micrometers, fig. 2.4.

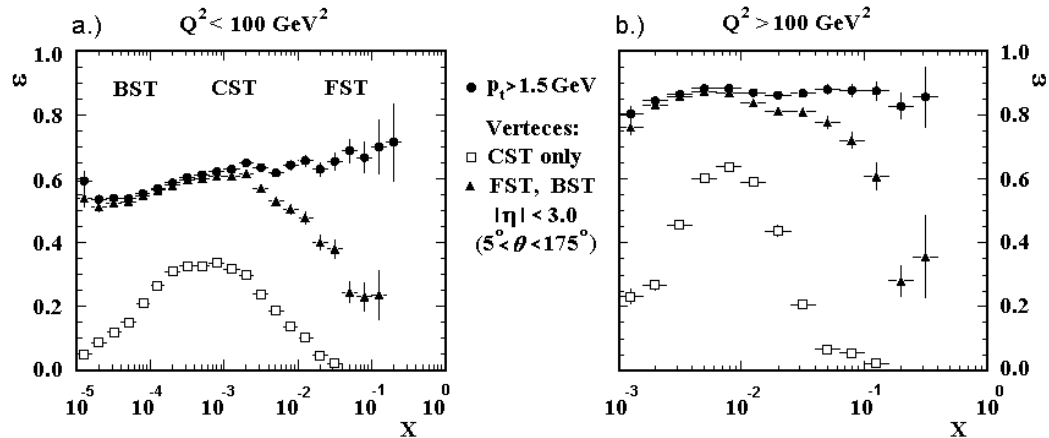


Figure 2.4: Acceptance of micro-strip detectors for heavy quark DIS events.  $F_2^c, F_2^b$  measurements become possible with (2..10)% systematic error in the extended  $x$  and  $Q^2$  range.

A few layers of the central drift chambers establish a so-called  $r$ - $\phi$  trigger [29] for tracks in the central region which have a distance to the nominal beam line smaller than 2 cm. Signals from CJC1 and CJC2 anode wires are discriminated by a threshold comparator. The combination of digitized pulses is matched to the predefined track patterns according to the track curvature in the magnetic field. The finite number of masks makes possible only separation of tracks with low or high transverse momentum. Then the number of validated tracks is counted to generate a level-one subtrigger.

A new fast track trigger (FTT) based on the CJC1 and CJC2 detectors is being implemented to provide a highly selective recognition of jets [30]

with their  $p_t$  down to 100 MeV. The analog readout of these chambers allows precise track measurements in the  $xy$ -plane with  $\sigma_{x,y} = 170 \mu\text{m}$  coordinate and  $\sigma_{p_t}/p_t^2 = 0.7\%$   $\text{GeV}^{-1}$  momentum resolutions.

### Backward Trackers

The backward region of the H1 tracking system is represented by two sub-detectors: the BDC and the BST which were strongly influenced by the HERA luminosity upgrade. Insertion of the new focusing magnet GG required shortening the silicon tracker by reducing its number of planes from 8 to 6. The increase of the inner diameter of the backward chamber as well as the SPACAL calorimeter required to build BPC which replaced the drift chamber used before. Moreover, the angular acceptance became a non-uniform function of the azimuthal direction  $\phi$  due to the excentric position of beams during the positron operation.

The Backward Silicon Tracker of the H1 experiment has been used in conjunction with the SPACAL calorimeter for detailed investigations of the deep inelastic scattering [31], [32], [33] and of charm production [34] at small Bjorken  $x \leq 10^{-3}$ . In its 1999/2000 configuration the BST was equipped with 3 types of silicon sensors: silicon pad detectors to trigger on particle tracks and silicon  $r$  and  $\phi$  strip detectors for the precise coordinate measurements of hit points in the  $r$ - $\phi$  plane [35], fig. 2.5.

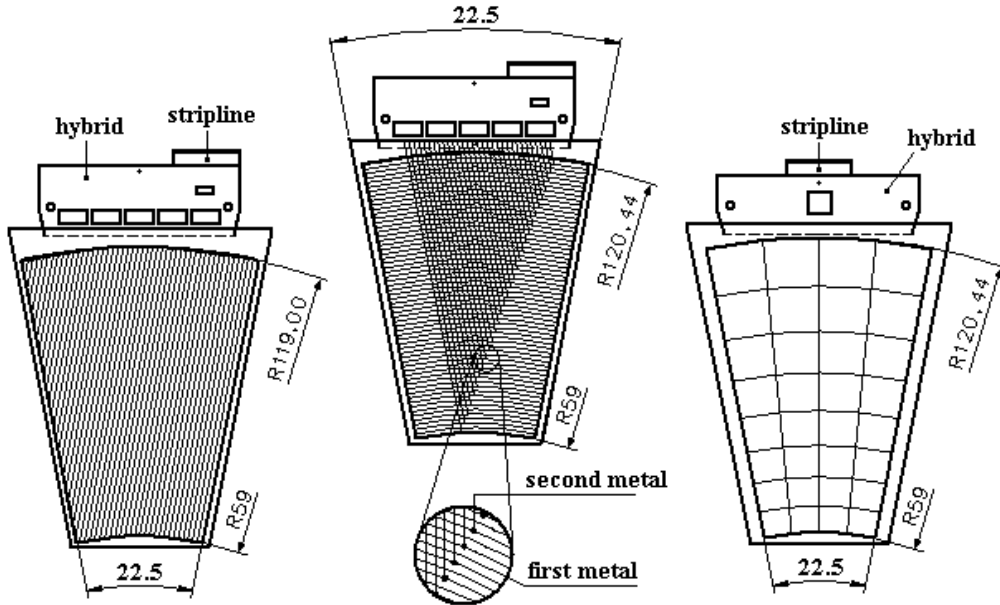


Figure 2.5: Silicon detectors with radial and concentric strips to measure  $\phi$  and  $\theta$  scattering angles and wedge-shaped pads for triggering.

The main trigger on backward scattered electrons, down to a few GeV of energy, is provided by the SPACAL calorimeter [36]. A large background to DIS events in this energy region stems from photoproduction processes. Its neutral component can be rejected with a track requirement in front of the SPACAL. Interactions between the proton beam and rest gas molecules are another source of background which may not be fully recognized by the SPACAL and its time-of-flight measurements. The background can be efficiently reduced by validating tracks from the vertex region and checking the hit multiplicity, which is particularly high for  $p$ -beam background and low for inelastic  $e^\pm P$  scattering events. For these purposes the BST-strip detector was completed with a "pad" system to detect charged particles and to compare their signatures online with prescribed track patterns, so-called trigger masks. The fast timing response (withing one HERA bunch crossing, equal to 96 ns.) of the pad detector makes it suitable for the first level trigger of H1.

### 2.1.3 Luminosity and ToF Systems

The luminosity is determined from the bremsstrahlung process  $e^\pm P \rightarrow e^\pm \gamma P$  where the incident electron suffers radiation energy losses in the electric field of the proton. This process has a dominant contribution in the total  $e^\pm P$  interaction cross-section and provides, therefore, the minimum random error for measurements. It is moreover precisely calculable in QED. The  $\gamma$ -quanta are registered by photon detector (PD) and the leptons scattered at very large angle can be detected by "electron taggers" (ET).

The photon detector contains a tungsten calorimeter with implanted quartz fibres to emit and to guide the Cherenkov radiation. The light collected has a PMT readout and the energy resolution is  $\sigma_E/E \approx 24\%/\sqrt{E/\text{GeV}} \oplus 1\%$ . The calorimeter is protected against the synchrotron radiation ( $E_\gamma \leq 150$  MeV) by a beryllium absorber at the PD entrance. A water-filled Cherenkov counter between the radiation shield and the calorimeter reduces further the synchrotron background and provides measurements for those  $\gamma$ -quanta which have produced showers in the absorber body.

Discrimination of energy signals  $E_\gamma > E_{thres}^{PD}$  provides a trigger element for the H1 data acquisition system. The instantaneous luminosity is determined from the PD trigger rate normalized to the cross section of the Bethe-Heitler process. The background and pile-up corrections are computed using the electron pilot bunch data and the relevant trigger mix: PD trigger, pilot bunch trigger, random trigger etc. The integrated luminosity is calculated offline relying on the PD trigger information [37]. The photon detector is also used to trigger on radiative DIS events.

The electron arm is equipped by two calorimeters: ET6 and ET40 which are placed at -6 m and -40 m from the IP, respectively. The ET6 tagger is similar to the SPACAL calorimeter but made of tungsten with radiation-hard scintillating fibres for the entry point of the lepton and its energy measurements:  $\sigma_E/E \geq 7\%/\sqrt{E/GeV} \oplus 1\%$ . The ET40 detector is a matrix of  $\text{PbWO}_4$  crystals with PMT readout. A local high-performance DAQ based on electron taggers is being prepared for the online photon detector calibration:  $E_\gamma = E_{e^\pm} - E'_{e^\pm}$ . Both, the ET6 and the ET40 produce L1 trigger elements for the H1 central trigger to register very low  $Q^2$  events.

Every new luminosity run is characterized by different levels of the beam induced background components. A simple and efficient technique to separate  $e^\pm P$  interactions from background particles is to measure their ToF-parameters as they have different paths to enter detectors. A number of scintillating counters located in the forward and backward regions of the H1 detector and a large scintillating wall behind the SPACAL provide timing markers for the H1 central trigger system. These signals define trigger elements applied to most sub-detectors as a veto condition for background events.

## 2.2 Data Taking Triggers

### 2.2.1 Central Trigger

The efficient use of high luminosity relies on the central trigger system (CT) which is programmed for searches of event candidates among the described above sub-detectors. To minimize the decision time this system has a multi-layer architecture with a fast global reset. The first level trigger "L1" consolidates all individual sub-systems:

1.  $z$ -vertex trigger from the CIP chambers;
2.  $r$ - $\phi$  vertex trigger from the CJC detector;
3. BST vertex trigger and/or background veto;
4. Liquid Argon hadronic and electromagnetic triggers;
5. SPACAL hadronic and electromagnetic triggers;
6. Muon trigger (not covered in this work);
7. ToF and Veto Wall anti-trigger and some others.

Their signals, so-called trigger elements (TE), have different delay times and duty cycles depending on response functions and operating conditions



of each sub-detector. Some H1 components, like the LAr calorimeter or drift chambers, require longer times to prepare their trigger acknowledges. The moment, when the sub-system trigger can be processed by the CT, is called the  $t_0$  bunch crossing<sup>1</sup>. The slowest detector, thus, determines a global  $t_0$  and any other TEs are delayed to be put in coincidence with this unique time.

There are 226 trigger elements defined for the first level trigger<sup>2</sup>. Their logical combinations, so-called subtriggers, are simplified signatures of physical events. The research policy of H1 defines priorities between subtriggers and establishes prescale factors for their rates, fig. 2.6. In addition, some artificial sources like the random generator or cosmic rays passing through the H1 detector can enforce an L1 decision. One or more successful subtriggers after the majority scheme announce the L1 accept after which the CT launches the readout phase of the central data acquisition system (CDAQ) and the intermediate trigger levels L2 and L3, otherwise the sampling phase is running further without having any dead time.

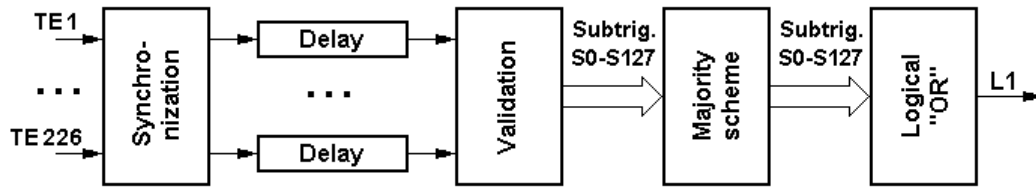


Figure 2.6: Data flow through the first trigger level of H1.

During the H1 sampling phase, information from the front-end is written into a pipeline memory synchronously to the HERA clock frequency. The H1 history for up to 32 successive bunch crossings is stored in the pipeline and available for the CDAQ<sup>3</sup>. The L1 decision to keep an event disables the pipeline updating, otherwise the relevant information would be overwritten.

The trigger levels L2 and L3 being developed as a fast track trigger, make full use of the high granularity  $t_0$  data stored in the pipeline. They validate the L1 decision through detailed searches for topology clusters, pattern matches, etc. in suitable sub-detectors. If the L2 or L3 filters reject an event, the data readout is cancelled and the sampling phase starts again. The L2 and L3 systems run in parallel with the CDAQ (bandwidth  $\approx 50$  Hz), fig. 2.7, and introduce, therefore, no additional dead time until they process faster.

<sup>1</sup>One HERA bunch crossing (96 ns) is taken as a minimum timing unit of H1.

<sup>2</sup>This is not a final number and it may change as the H1 detector will evolve.

<sup>3</sup>This makes the offline timing studies possible, but the main purpose of the pipeline is to buffer the sub-system data and, therefore, to minimize the CDAQ access time.

Their effective performance is defined as an input rate multiplied by the latency time, equal to  $20 \mu\text{s}$  and  $100 \mu\text{s}$  respectively. This requires the L1 accept rate to be kept at about 1 kHz level and it is realized via setting appropriate prescaling factors for subtriggers [38]. Every sub-detector must provide, nevertheless, a reasonable frequency for its trigger elements.

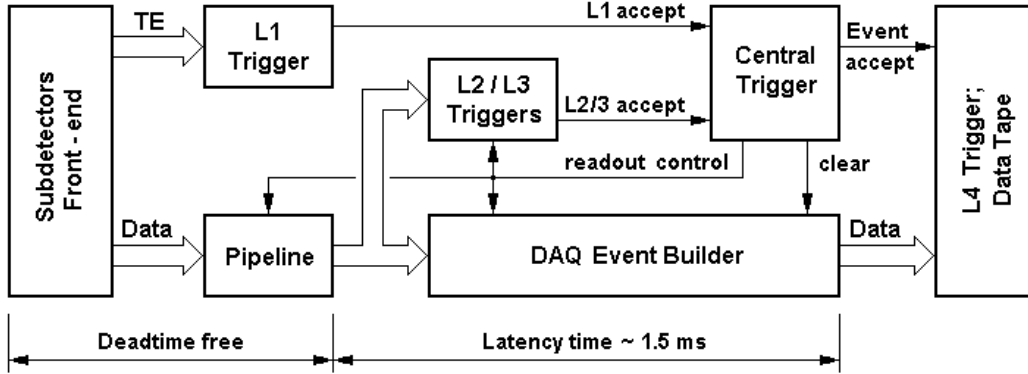


Figure 2.7: The H1 central trigger and the event builder.

The software level L4/5 contains all essentials of standard offline reconstruction programs. This system makes the final trigger decision to log the H1 event onto tape. As reconstructed data of the whole detector merge in the L4 level for the first time, this module is suited for the automatic computing of prescaling ratios for different physical subtriggers [39] as functions of beam conditions: injection, lumi tuning, stable run, end of the fill. The L4/5 information becomes useful for monitoring, calibration and efficiency studies of the new and upgraded H1 components.

### 2.2.2 Low $Q^2$ Triggers

Each physics working group prefers a set of subtriggers for optimum analysis. The inclusive DIS measurements performed by the ELAN group ("Electron Analysis") are based on scattered charged leptons for  $Q^2 \leq 150 \text{ GeV}^2$  which are reconstructed in the SPACAL and, for lower  $Q^2$ , pass the BST. The following physical subtriggers are utilized [40]:

1. The "S0" is the subtrigger used in most of the kinematic region for the  $F_2$  structure function measurements. It requires an energy cluster in the electromagnetic part of the SPACAL with about 6 GeV threshold. A veto wall decision should be negative and background signals from the ToF system in the SPACAL region (SToF) and the backward ToF system (BToF) should be absent as well as the background signal from

the Forward Interaction Timing system (FIT). A short-form of writing the subtrigger (symbols  $\&$ ,  $\|$ , and  $!$  express conjunction, disjunction and negation logical functions, respectively) is the following:

$$S0 = (\text{SPCLe\_IET} > 2) \& \text{v:3} \& \text{f:1}, \quad (2.1)$$

where  $\text{v:3}$  and  $\text{f:1}$  are the shortcuts for the veto conditions:

$$\text{v : 3} = ! \text{BToF\_BG} \& ! \text{SToF\_BG} \& ! \text{Veto\_BG};$$

$$\text{f : 1} = ! \text{FIT\_BG} \& \text{FIT\_IA}.$$

2. The access to the high  $y$  range for the  $F_L$  measurements, that follows from the formula (1.27), requires lower thresholds in the SPACAL according to equation (1.16). The event frequency increases at low thresholds. The subtrigger "S9" implementation includes, therefore, a low multiplicity track confirmation from the CJC (DCRPh trigger) and the CIP (zVertex trigger). This allows to use a minimum energy in the SPACAL ( $\geq 2$  GeV).

Additional veto conditions are applied to the hadronic part of the SPACAL because at high  $y$  the hadronic final state is scattered backward as well. Therefore the hadronic energies (AToF) are compared with 0.6 GeV and their sums (ToF) with 12 GeV thresholds to produce a negative trigger decision.

$$S9 = (\text{SPCLe\_IET} > 1) \& \text{v:5} \& \text{f:1} \& \text{t:0} \& \text{z:0} \& \text{d:0}, \quad (2.2)$$

$$\text{v : 5} = \text{v:3} \& ! \text{SPCLh\_AToF\_E\_1} \& ! \text{SPCLh\_ToF\_E\_2},$$

$$\text{t : 0} = \text{DCRPh\_T0};$$

$$\text{z : 0} = \text{zVtx\_mul} < 7;$$

$$\text{d : 0} = ! \text{DCRPh\_many}.$$

Central trackers have a rather different angular acceptance than the SPACAL. This leads to a somewhat biased DIS data sample from the "S9" trigger which was the only way to access the low  $E'_e$  region with the new BST-Pad detector, however. It is yet natural to have a basic SPACAL + BST trigger in the backward region without further track requirement. This would extend the kinematic region of the "S0" towards lower  $Q^2$  values keeping the trigger rate on an acceptable level. At the "Ringberg 2002" H1 trigger workshop it was proposed by the ELAN group to introduce corresponding new subtriggers "S01" and "S09". As can be seen in fig. 2.8, the advantage is mainly due to reduce the background at low  $E'_e$  and thus also the overall trigger

rate. In this figure only the general definition of the subtriggers is given. The number of trigger elements and their thresholds could be different for some special, so-called "minimum bias" conditions. Prescaling factors can be applied for those subtriggers depending on the beam conditions, but for the rate estimates transparent runs (without prescaling) are taken or other monitor triggers used.

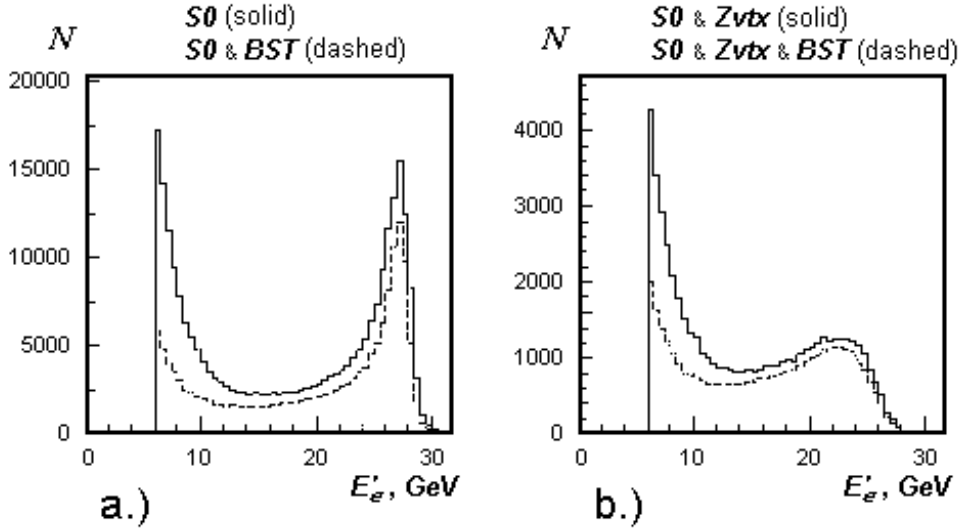


Figure 2.8: Estimates for the background rate reduction for the new subtriggers "S01" a.) and "S09" b.) at low energies with the track requirement in front of the SPACAL in the BST angular acceptance.

### 2.2.3 BST Triggering Concept

The main idea of the BST trigger is: a.) to select charged tracks (in the  $r - z$  plane) pointing to the interaction vertex and b.) to veto on upstream going tracks. The track validation algorithm also includes a cut on the hit multiplicity in the pad detector to further suppress the background caused by the proton beam.

The trajectory of a charged particle in the solenoidal magnetic field can be reconstructed if it produces 3 or more space points (hits) in the detector. The actual BST design contains 4 active pad layers. Their geometry and positioning is defined by the following constraints: the CIP and the beampipe determine the outer and the inner diameters of the detector respectively. The BST length is limited at both sides by the central silicon tracker and the GG magnet, respectively.

From a simulation of DIS events in this region an angular distribution of hadrons and the scattered electron (positron) crossing one of the detector planes was found [41]. The azimuthal segmentation of the BST should allow to separate their signals, because silicon sensors themselves don't distinguish leptons from charged hadrons as they are all minimum ionizing particles. For a symmetric design with a conventionally chosen 16-fold division in  $\phi$ , only 1% of events have hadrons traversing the same  $\phi$ -sector as the scattered lepton.

It is worth noting that the BST-Pad design profits from the quiet environment: in the backward direction dominantly the electron is the only particle or, for a process like  $J/\Psi \rightarrow e^+e^-$  one or two electrons are to be observed in the BST. This is in contradiction to high  $Q^2$  events in the forward region or to  $p$ -beam induced background events.

Charged tracks with the momentum of a few GeV/c can be approximated in the BST angular acceptance as straight lines defined by two points, but the third point is still necessary for a robust track decision, because the probability to fulfill randomly the criterion of two hits is high enough. The estimates of the track stiffness versus different particle momenta is given in fig. 2.9 for the 16-fold azimuthal segmentation of the BST.

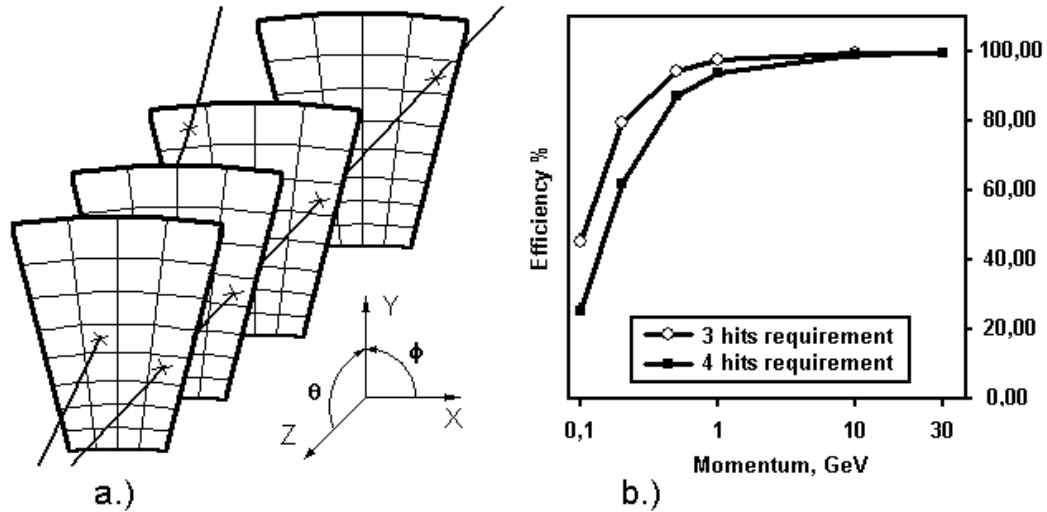


Figure 2.9: Fraction of tracks staying in one sector within 3(4) BST disks.

The confinement of tracks with  $p \geq 1$  GeV/c to one sector considerably simplifies the principle of the trigger and, hence, its hardware realisation. Only those tracks, which are sufficiently stiff, may be selected. Still, a link between neighbouring sectors (the " $\phi$ -bus") is foreseen on the hardware level to trace particles with lower momenta.

Formation of straight trigger roads crossing the detector planes and pointing to the vertex requires a certain radial subdivision of every silicon wafer.  $Z$ -positions of the pad and strip layers closely follow each other and for both a ratio  $Z_{n+1}/Z_n$  is kept constant. This provides for similar triangles the same ratio  $r_{k+1}/r_k$  independent of the crossing angle and leads to a sequence (2.3) and (2.4):

$$Z_{n+1} = Z_n \sqrt[N]{\frac{r_{max}}{r_{min}}}, \quad r_k = \left( \frac{Z_{n+1}}{Z_n} \right)^k r_{min} \quad (2.3), (2.4)$$

For  $N = 4$  planes a set of  $k = 8$  rings was chosen to keep the number of possible signal combinations for tracks acceptable (fig. 2.10). An event has triggered if at least one predefined track pattern (mask) is met. Usually the mask means an exact superposition of signals from all four detector layers. Although the efficiency of every individual plane is high, the efficiency of the trigger degrades when the signal correlation between several planes is required. A number of permutations with a lower number of participating layers can be written for every mask to retain the total efficiency.

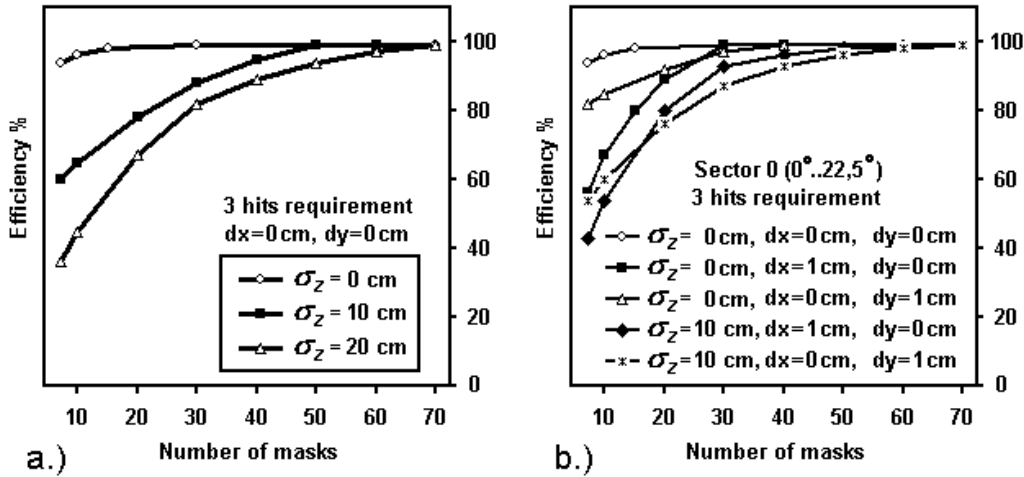


Figure 2.10: Geometral corrections to the BST trigger efficiency:

- a.) the mask number dependence on the vertex smearing;
- b.) the mask number dependence on the beam offset.

A large smearing of the vertex position around the nominal interaction point with  $\sigma_z = 12$  cm due to about 1.4 ns proton bunch duration leads to a further pattern number increase. The maximum allowed number of masks  $N$  determines a  $z$ -vertex cutoff and hence, the trigger efficiency, fig. 2.10 a). During positron operation of HERA-II the specified offset of the beamline

( $x = 8$  mm) breaks the  $\phi$ -symmetry of the BST and introduces more trigger masks individually for every sector, fig. 2.10 b). A total of 70 masks is enough to ensure high trigger efficiency. The trigger is realized, therefore, as a compromise between the residual inefficiency accepted and the risk of a random pattern match from background or from electronic noise.

### BST for the 1st-level trigger

The BST-Pad provides L1 trigger elements for tracks. An additional flag is set for the multiple tracks with the "back-to-back" topology which can be accepted for some physical cases. A "veto" TE is used to control background conditions: it indicates the high detector occupancy or the upstream direction of at least one track. These signals are generated and transmitted during the H1 sampling phase once per every HERA clock period that corresponds to the dead timeless triggering concept. The BST-Pad trigger elements are coded into 8 bits of the CT input word. Their definition is adjustable and the current implementation is given in table 2.1.

Table 2.1: The BST-Pad trigger word for the L1

Element	Description
<b>TE192</b>	Track with projection onto the inner SPACAL region
<b>TE193</b>	Track with projection onto the outer SPACAL region
<b>TE194</b>	Two tracks with back-to-back condition in
<b>TE195</b>	High pad multiplicity (more than 6 hits per track)
<b>TE196</b>	Calibration pulse (timing marker for the pipeline)
<b>TE197</b>	Not defined yet
<b>TE198</b>	Not defined yet
<b>TE199</b>	Radiation monitor (has no physical meaning for the CT)

The arbitrarily defined "inner" and "outer" regions of the SPACAL differ in their trigger rates because of the  $e^\pm P$  cross-section dependence on the lepton scattering angle. Therefore the BST-Pad may provide two trigger signals which correspond to the track projection onto one of those regions. It allows to separate  $Q^2$ -dependent prescaling factors for combined BST + SPACAL subtriggers which then form the unique DIS physical subtrigger.

### BST for the 2nd-level trigger

The "L1" decision of the BST-Pad can be validated at the L2 trigger level. It is particularly important for multiple tracks to resolve the leptonic and the

hadronic signals. This could be done by the L2 topological trigger (L2TT) which may calculate for every track its projection onto the focal plane of the SPACAL and check for signals in this region in the electromagnetic calorimeter part. Therefore the topological data (angles  $\theta$  and  $\phi$ ) for all track candidates in the BST-Pad are made available for the L2TT trigger subsystem. The pad detector provides this information via the L2 data bus. The definition of the data bits is given in table 2.2.

The  $\phi$  angle of each track is naturally defined by the BST sector number. In the given  $\phi$ -sector every triggered mask matches to a certain mean value of the polar angle  $\theta$ , or to some angular range in  $\theta$  if several masks have been triggered. These values have been found by simulation of tracks and coded into the BST-Pad trigger algorithm, see AppendixB for details.

Table 2.2: The BST-Pad trigger word for one  $\phi$ -sector sent to the L2TT

Data Bit	Description
<b>D0</b>	Radiation monitor (has no physical meaning for the L2TT);
<b>D1</b>	Encoded number $D$ which corresponds to the polar angle $\theta$
<b>...</b>	of the track when <b>Bit_7</b> = '1' or to the multiplicity of trig-
<b>D5</b>	gered pads $N(0...31)$ in any other cases;
<b>D6</b>	Veto signal (high detector occupancy or non-eP tracks);
<b>D7</b>	Flag for the track candidate(s) in the given $\phi$ -sector.

For more detailed combinatorics between different subdetectors a neural network techniques (L2NN) is utilized that requires information about all triggered pads - the so-called "raw" data from the BST-Pad. During the H1 sampling phase the topological and the raw data are stored in a pipeline. The information about every new bunch crossing is written into the first memory cell while the whole history is shifted by one time slice.

The depth of the pipeline for the topological data is adjusted in a way that the last memory cell contains T0-relevant data before sampling has been stopped. After the "L1 keep" announcement the content of this last cell is transmitted through the L2 bus to the second-level topological trigger synchronously to the HERA clock frequency that takes the first 7 periods as shown in fig. 2.11.

The raw data pipeline has a pointer to the "T0" cell, the content of which is transmitted during "L1 keep" via dedicated cables to the L2NN that takes only 4 HERA clock periods, fig. 2.12. The radiation monitor - an auxiliary function of the pad detector which shares one data line with the trigger algorithm (see chapter6 for details), - is halted for that time.



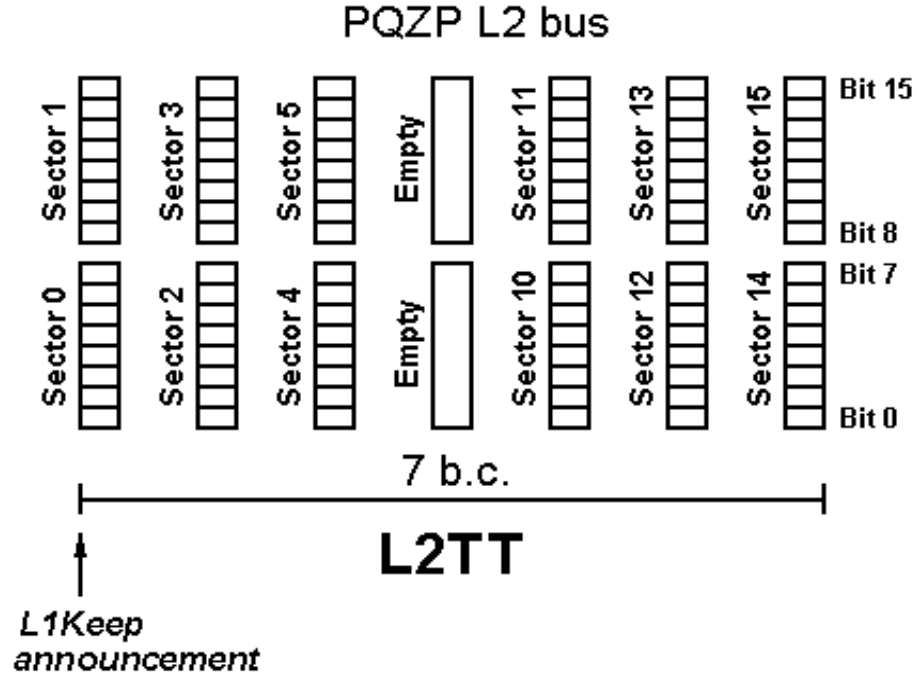


Figure 2.11: The topology data package of the BST-Pad detector. Its transmission takes  $\approx 4\%$  of the L2 trigger decision time.

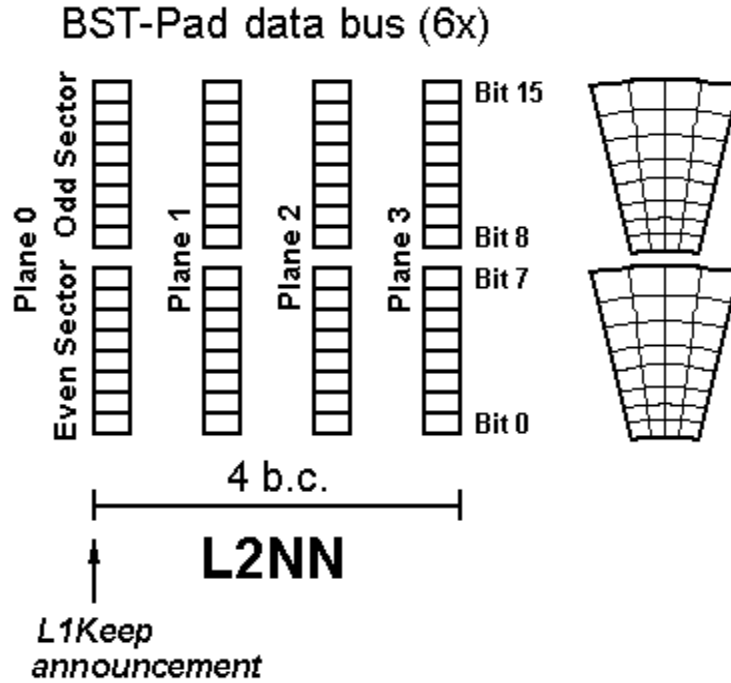


Figure 2.12: The raw data package of the BST-Pad detector. Every bit corresponds to 4 ORed pads of the same detector's ring as can be judged from the plot.

### **Silicon readout branch**

The full content of the topological pipeline and the status word of the BST slow control system are read out by the VMETaxi system via a VME interface in the so-called "sub-system trigger crate" (STC) which belongs to the "silicon readout branch" (number 12) of the central data acquisition system [42]. The readout cycle lasts 1.3 ms on average because it includes also the raw data processing from silicon strip detectors.

## **2.3 Conclusion**

The layout of the H1 facility was upgraded by new focusing magnets close to the interaction region. This led to a revised luminosity system and modification or rebuilding of the FTD, BPC, SPACAL and BST detectors. The latter contains now the L1 trigger with dedicated new readout electronics. This uses an algorithm for the track recognition based on the signal matching to a certain set of masks controlling the hit multiplicity and generating the veto on background events. The BST trigger decision still needs verification by adjacent detectors like the SPACAL and the ToF system, but its stand alone operation with more sophisticated algorithms should be possible. It must though be ensured that local failures are prevented from disturbing higher levels of the trigger system and thereby affect data collected from other parts of the H1 detector.

# Chapter 3

## The BST Trigger System

### 3.1 Overview

After the HERA upgrade in 2001 the redesigned "Pad" system started to operate. It incorporates 48 detector modules. The attached 6 electronic boards provide full detector control and perform the main data reduction algorithm. The data from each board are transmitted to the H1 central trigger system via a VME interface. The VME repeater cards route and synchronize the data flow. Store cards accumulate topological data into pipeline to be read out later upon the demand of higher level triggers. The master card provides a level-one trigger decision. In appendix A one can find the full circuit diagram of the slow control environment and of the readout system which complies with the "dead timeless" triggering concept of H1.

### 3.2 Detector Layout

The radial, azimuthal and longitudinal subdivisions of the BST-Pad detector are chosen to realize a vertex-pointing track geometry as described in a previous chapter. The apparatus consists of 4 wheels placed around an elliptical beampipe at distances  $Z = -477, -520, -568$  and  $-620$  mm with respect to the nominal vertex position. On each wheel twelve wedge-shaped detector modules are mounted perpendicular to the beam axis. Their sensitive region extends radially from 59 to 120 mm. In the polar angle  $\phi$  they cover  $270^\circ$ .

Due to an excentric position of the beampipe inside the H1 detector which accounts for the synchrotron radiation fan, a gap of  $90^\circ$  appears for the BST in  $\phi$  that required silicon strip and pad sensors with non-standard shapes to be introduced at more than 4  $z$ -positions. In the pad detector a track is defined by hits in at least 3 or 4  $Z$ -planes, thus the electron scattering angle  $\theta$ , for a vertex at  $Z = 0$ , ranges from about  $168^\circ$  to  $174^\circ$ , with respect to the proton beam direction.

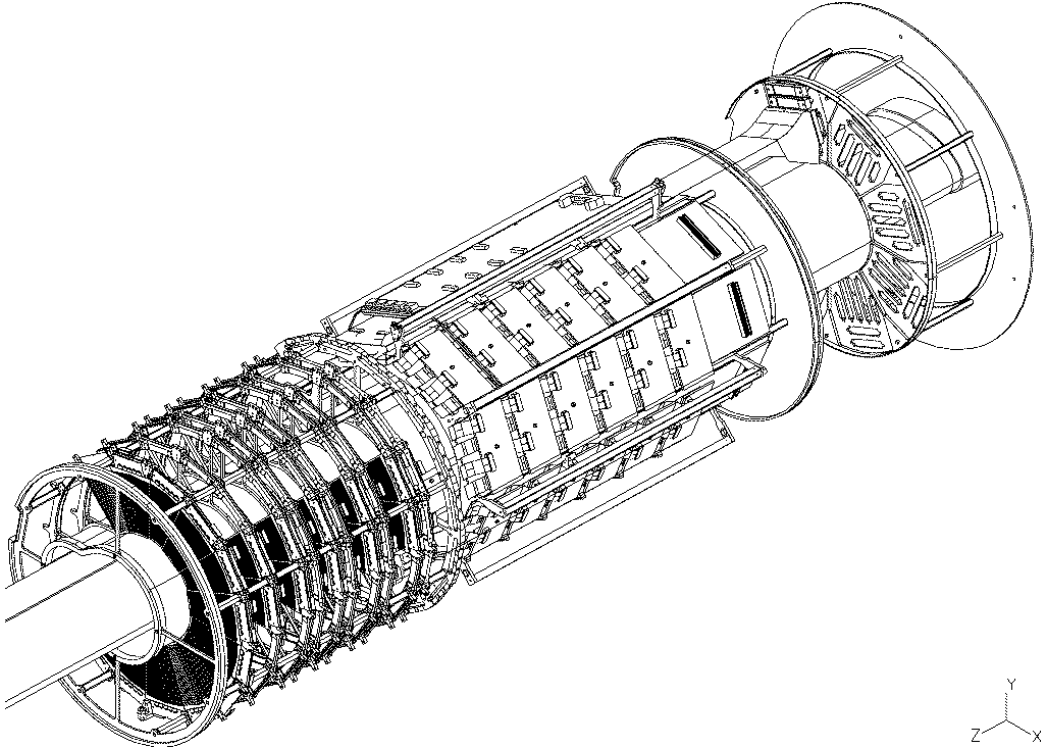


Figure 3.1: BST technical drawing (the global view) with the Silicon wheels (left), the front-end (middle) and the cable support rings (right). The 4 pad detector planes are mounted next to the strip detector planes to the repeater adjacent side. This drawing does not show the thin Cu-plated kapton electromagnetic shielding which covers the whole detector.

### 3.3 Detector Module

Every detector module [43], fig. 3.2, consists of a silicon sensor (32 pads on a common substrate) and a small printed circuit board (hybrid) with a readout chip – application-specific integrated circuit (ASIC). A special flexible stripline on kapton basis provides an electrical connection between detector hybrids and the front-end boards. Every hybrid has an aluminium substrate contacting the water cooling ring for the heat distribution. To prevent the air moisture condensing all modules should operate in the dry nitrogen atmosphere.

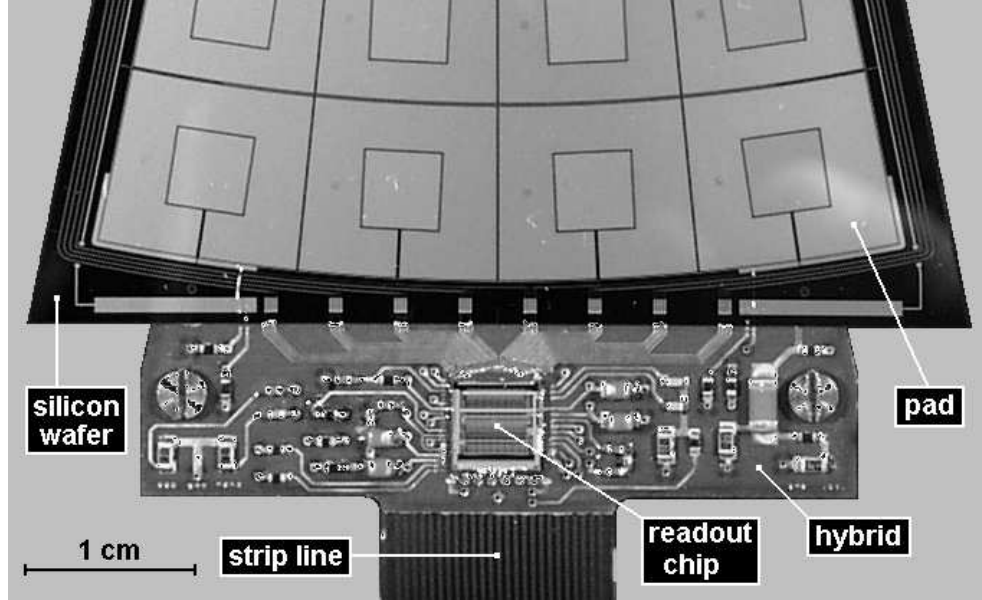


Figure 3.2: Pad detector module (only part of the wafer is shown). An additional 4-fold azimuthal subdivision of the silicon sensor reduces the detector capacitance seen by the preamplifier.

### 3.3.1 Silicon Sensor

The  $380\text{ }\mu\text{m}$  thin, single sided silicon sensors [44] were designed by DESY Zeuthen and manufactured by Micron Semiconductor Ltd. [45] in an ion-implantation polyimide passivation process. All pads are AC-coupled and use FOXFET biasing [46]. The capacitances of fully depleted pads range from 15 to 50 pF depending on the pad size ( $33.3\text{ mm}^2$  to  $115.7\text{ mm}^2$ ). A guard ring surrounds the active area of the silicon sensor to avoid distortions of the inner electric field at the crystal edges.

The signal from a minimum-ionizing particle (MIP) crossing perpendicularly a silicon wafer, amounts to 25000 electron-hole pairs on average [47]. The number of free charge carriers produced by one MIP in a thin (with respect to the particle radiation length) absorber, obeys the Landau distribution law [48]. The statistical fluctuation of this number causes a random noise component. The resulting electrical noise is a superposition of the detector's noise, the inherent noise of the readout chip and the pickup noise. Both, thermal and shot noises of the silicon sensor are comparably small due to the low input impedance of the readout electronics [49]. The ASIC's noise is determined by several design parameters and implementation technology and the pickup noise depends on the detector screening scheme and the power supply circuitry.

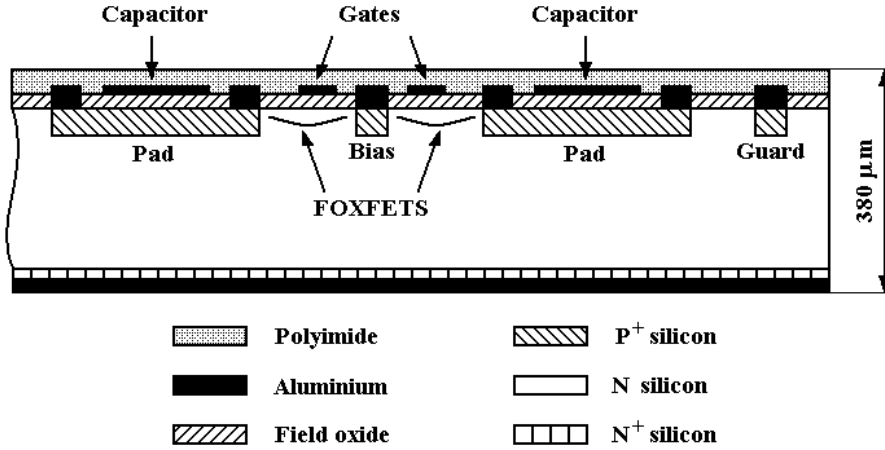


Figure 3.3: Cross-section of the silicon wafer.

### 3.3.2 Readout Chip

The BST trigger system required a front-end with good signal-to-noise characteristics. The readout chip PRO/A, designed in collaboration with IDE AS in Oslo [50], improved very much the functionality of the previous ASIC. The new chip has 32 channels with analog and digital outputs as compared to 4 in the old chip. Every channel contains a charge-sensitive preamplifier with variable gain, an active low-pass filter with 30 ns time constant, a differential amplifier, a discriminator with a passive high-pass filter at the input, a mono-flop which can be disabled for the time-over-threshold mode and an open-drain output buffer.

An important new feature of the PRO/A chip is that the differential amplifier allows the subtraction of the analog signals in two neighboring channels from each other. This removes those signal harmonics, which are common to both pads. This method was studied in a test beam and then implemented into the chip design, fig. 3.4. It replaces the software based common mode subtraction for strip detectors by electronics which was seen to be necessary for triggering.

In every channel there is an input current compensation scheme which is able to draw/sink up to 500 nanoamperes of the DC current to avoid saturation of the preamplifier when one or more pads have their decoupling capacitors shortened. This feature can be turned on and off. Several internal "bias" voltages define the ASIC's operating regime. Their superposition gives a common threshold voltage for 32 discriminators, but external thresholds can overdrive these settings in 8 groups of 4 channels each.

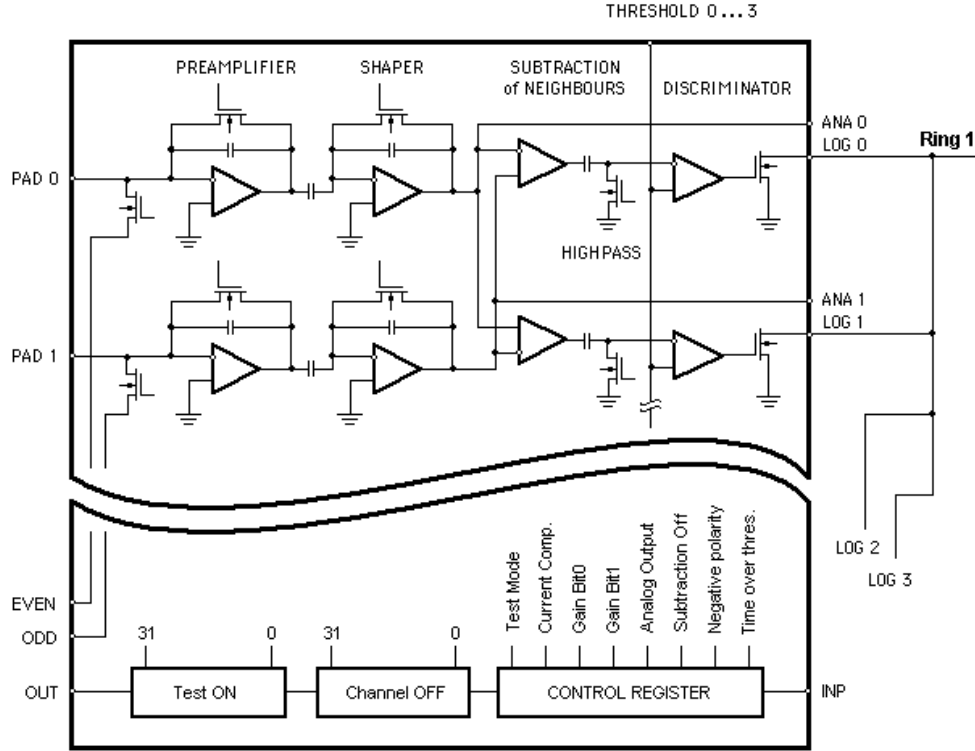


Figure 3.4: Schematic diagram of the PRO/A readout chip. Signal processing circuitry: the preamplifier, the shaper, the differential amplifier and the discriminator described above are shown. The chip has a regular structure with 32 channels steered from the control registers (below).

The chip steering is done via a 72-bit control register. The register content, the so-called "sequencer code", has a default "power on" configuration, but it can be changed any time when new system settings are necessary. There is one synchronous input and one synchronous output for the serial data and else one input for data strobes. The incoming data bit is latched during the low-to-high transition of the accompanying clock signal. The maximum download frequency is about 1 MHz. Thus it takes at least  $72.5 \mu\text{s}$  to reconfigure the chip.

The ASIC contains a calibration/test circuitry which multiplexes an external charge pulse from a special input to one of the odd and/or even channels. Each digital output can be enabled or disabled from the control register. Together with the calibration pulse circuitry this allows the simulation of some special signal patterns to study the trigger response.

Several wafers were fabricated in a  $1.2 \mu\text{m}$  N-well CMOS process by AMS [51] and then shipped to the IDE AS for quality checks.

### 3.3.3 PRO/A Chip Evaluation

An experimental setup was assembled at IDE AS and a method was developed to test the fabricated chips. Bias voltages were measured with high precision. The data obtained had a regular structure, correlated to the wafer number and the chip position on it. The maximum deviation observed was about 10% indicating technological deficiencies.

The signal-to-noise ratio (S/N) has been measured with a calibration pulse. Two reference amplitudes with a rather large offset were chosen to avoid big random errors coming from noisy environment (the special probe card which provided electrical access to the bond pads had long unshielded wires). An independent series of calibration measurements was performed for a few ASICs under low-noise laboratory conditions in DESY Zeuthen and then the whole data set was renormalized.

Table 3.1: PRO/A parameters check-list.

Parameter	Specified value	Measured value
Dynamic range	$\geq 25$ dB	$\approx 35$ dB
Sensitivity	$\geq 25$ mV/fC	<sup>1</sup> $30 \pm 1$ mV/fC
Noise performance ( $1\sigma$ )	$\leq 1200 \bar{e}$	<sup>2</sup> $1100 \pm 100 \bar{e}$
Detector capacitance	$\geq 70$ pF	up to 500 pF
Channel cross-talk	$\leq -40$ dB	$-42 \pm 2$ dB
Shaping time constant	$\leq 25$ ns	$30 \pm 1$ ns
Event frequency	$\leq 10$ MHz	$\leq 5$ MHz
DC input current	$\geq 50$ nA	up to 500 nA
Power dissipation	$\leq 5$ mW/chan.	$4.20 \pm 0.03$ mW/chan.
Ambient temperature	$(10..70)^\circ\text{C}$	<sup>3</sup> tested up to $70^\circ\text{C}$

<sup>1</sup>Adjustable in four steps; the maximum value is given.

<sup>2</sup>For the highest gain and with 40 pF capacitor at the detector's input.

<sup>3</sup>All measurements held at  $(22.0 \pm 0.5)^\circ\text{C}$ . The functionality was proven at  $70^\circ\text{C}$ .

In total 48 plus some spares ICs out of 203 tested were needed for the BST Pad detector. Thus it was possible to apply a rigorous selection cut. A threshold scan (the number of trigger counts " $N_i$ " versus the threshold voltage set " $V_i$ ",  $i=1..32$ ) was done for every channel of the readout chip with a calibration pulse fed in. The curve obtained is a convolution of the amplitude spectrum with the number of issued calibration pulses. The normal distribu-



tion is received by computing the first derivative  $(dN/dV)_i$ . Here the mean value  $M_i$  of the Gaussian peak corresponds to the most probable amplitude and the standard deviation  $\sigma_i$  is a measure for the noise. The signal-to-noise ratio  $M_i/\sigma_i$  for every channel was chosen to define the ASIC's quality<sup>1</sup>. The S/N-cut is rather strong and the number of accepted ICs decreases rapidly above a certain value. Therefore this method is good only to identify all those defective devices with a high noise and/or a small gain. A chip was rejected if at least one of its channels did not fulfill the S/N-criterion.

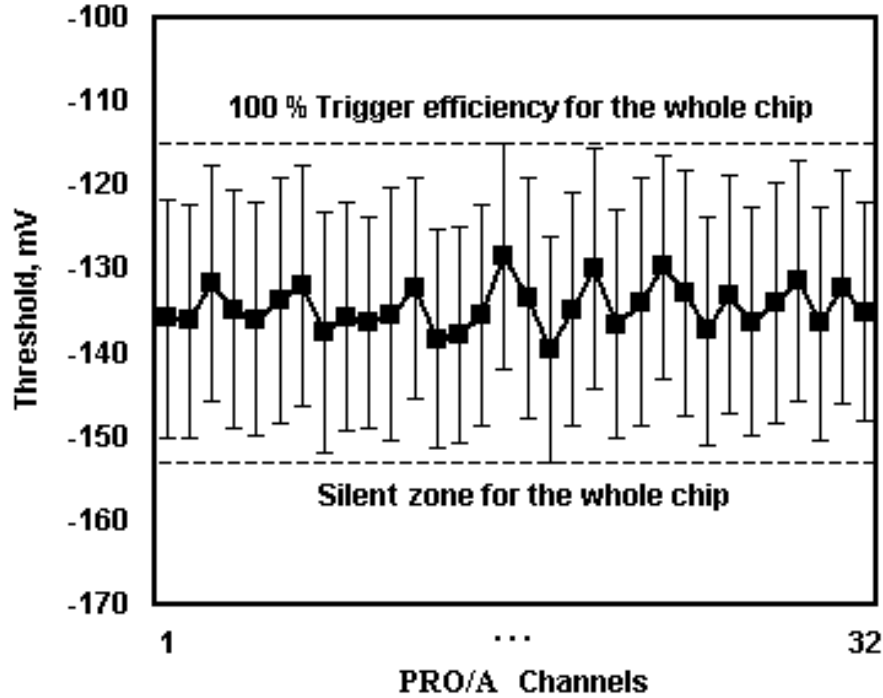


Figure 3.5: The threshold spread for 32 channels of a pad readout chip. Error bars show  $3\sigma_i$  intervals

An additional cut was applied choosing accordingly the operating threshold voltage. The value  $T_i = M_i - 3 \cdot \sigma_i$  corresponds to the maximum threshold allowed in order to preserve the high trigger efficiency, fig. 3.5. The worst channel with the smallest gain and the largest noise thus determines the common threshold for the whole chip:  $T_c = \min [T_i]$ . The higher the threshold to discriminate a given input signal (i.e. the higher gain) the more the chip is safe against noise triggering. A simple matching of  $T_c$  values is not reliable

<sup>1</sup>The pedestal value  $P_i$  must be subtracted from the mean amplitude  $M_i$  to compute properly the  $(S/N)_i$ . For the typical input signal of 4 fC the unknown pedestal introduces an about 10% systematic error.

because of unknown pedestal values which may determine the result of the comparison (the systematic uncertainties are rather high in this case).

This task can be solved differently: assuming that all ASICs have about the same S/N-ratio after the first cut, a minimal noise automatically determines the highest threshold. The noise measure was redefined as  $\Delta = \overline{M} - T_c$ , where  $\overline{M}$  is the average  $T_i$  threshold for the chip. The role of the  $\Delta$  parameter as an alternative to the standard deviation is shown in fig. 3.6. The minimal  $\Delta$  characterizes how "close" to each other all 32 channels are and ensures a high trigger efficiency for the whole detector module.

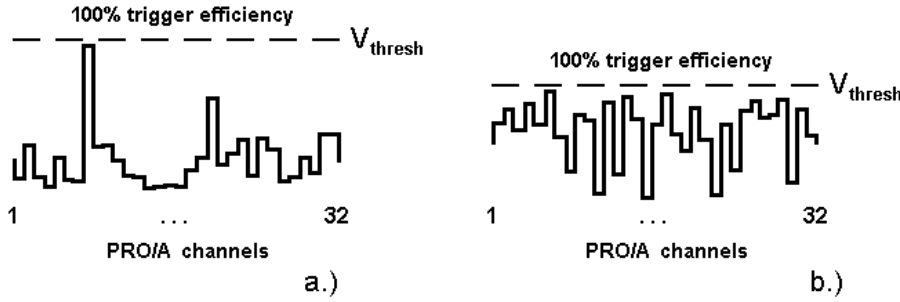


Figure 3.6: The threshold voltage  $T_i$  spread among 32 channels of the PRO/A readout chip (see text above) for which the mean  $\overline{M}$  and its standard deviation can be found. The standard deviation is smaller in case a.), but case b.) is preferable, because the common threshold will be more safe (better separated from the noise).

Two different computer systems were used for data acquisition: "Windows 98" at IDE AS in Oslo and "MacOS 8.0" at DESY Zeuthen. For both platforms, "Microsoft Excel" files provide a compatible data format. Therefore the evaluation program was written in "Visual Basic". The positive ASIC yield was nearly 83% (31% - perfect and 52% - good). About 4% did not pass the quality check and the remaining 13% had corrupted data. They could be used for test purposes.

### 3.3.4 Pad Hybrid

The PCB carries capacitive filters for the ASIC supply and RC-filters for the threshold and the depletion voltages. Initially the hybrid prototype had filtering capacitors for several bias voltages. In the final design these were omitted without degrading the chip performance. The output trigger pulse width was adjusted to 50 ns with an external resistor, drawing an additional bias current.

The calibration circuitry provides a double MIP signal for the even/odd test inputs of the readout chip. This signal is generated by the front-end and transmitted to the detector module via the stripline. On the hybrid this pulse is terminated to match the characteristic impedance of the stripline.

The hybrid circuit diagram and the board layout were designed in the "OrCad" v.9.1 development system [52]. All hybrids passed functionality tests before and after the ASIC assembly and after mounting of silicon sensors.

### 3.4 Front-end Interface

Every electronic board, fig. 3.7, provides full control over a double  $\phi$ -sector made of 8 detector modules. This includes: setting thresholds, generating, downloading, reading back and verifying of sequencer codes, issuing calibration pulses, receiving and processing of trigger signals. The need of a high-density device for these purposes led to a choice between two commercially available platforms: the "Altera" [53] and the "Xilinx" [54]. The support service availability and some technical advantages (see table 3.2) were the main reasons to select the "Altera" family.

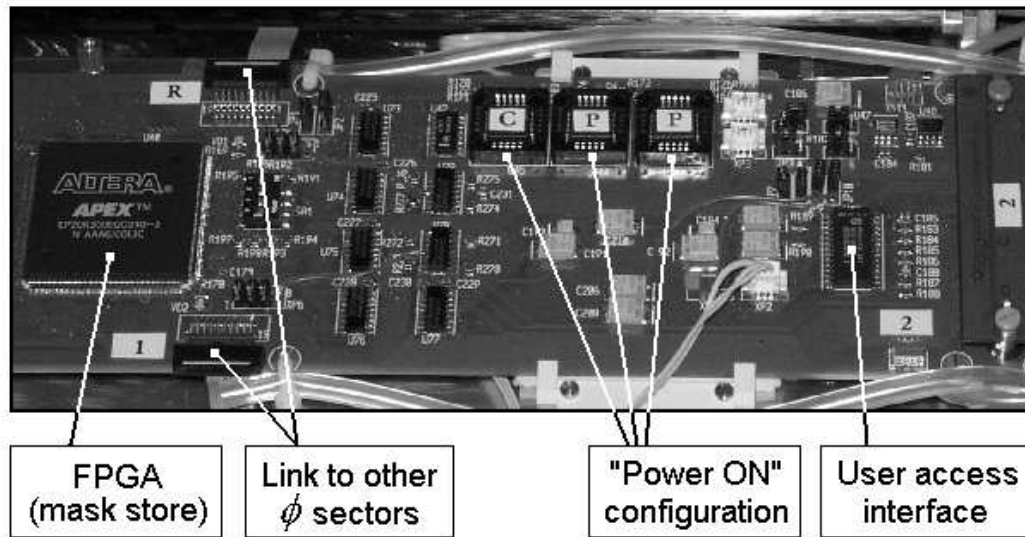


Figure 3.7: Front-end board with the "APEX" EP20K300E chip on the top side (detector modules and the second FPGA aren't shown).

Thus each card was equipped with two field-programmable gate arrays (FPGA): "ACEX" EP1K30 for the slow control and "APEX" EP20K300E for the on-line trigger data analysis. A platform-independent "Very fast Hardware Programming Language" (VHDL) [55] was chosen for the FPGA programming.

The user access to the front-end is organized via a serial line input/output interface (SLIO) to the controller area network (CAN). The CAN SLIO environment contains a front-end micro-controller P82C150 with a transceiver PCA82C250 [56], and a VME card VIPC616 [57]. Programs in the "Lab-View" framework [58] format are the top-level software of the CAN SLIO hierarchy.

Table 3.2: High-density programmable devices.

Platform	Xilinx	Altera
Compatible products	VIRTEX XCV50E..3200E	APEX EP20K60E..1500E
Logic densities	(1,7...71) K cells	(2,5...52) K elements <sup>1</sup>
Max. clock frequency, MHz	100	100
Advanced technology	—	Clock boost Clock shift Multi-clock
Design systems	Aliance <sup>2</sup> (UNIX) Foundation <sup>2</sup> (UNIX) PowerView <sup>2</sup> (UNIX)	Quartus(Windows)

<sup>1</sup>"Altera" capabilities are the same as of "Xilinx" due to highly organized architecture.

<sup>2</sup>Requires the "Xilinx Design Manager" with a new license for the final compilation.

### 3.4.1 Hardware Solutions

Below some technical aspects of the electronics design are summarized:

- Special care has been taken for the hybrid and the front-end board power supplies. Each detector module needs 3 supplies: analog and digital voltages ( $\pm 2$  V) for the readout chip and the depletion voltage for the silicon sensor. They all have independent sources and their grounds are tied together at one common point on the hybrid. This is a typical scheme used in low-noise equipment. The front-end requires 4 different voltages, but contrary to the hybrid, all have the same ground. This variety of voltages is explained by different types of semiconductor

components. The following approaches to derive all voltages from a single source are known:

- inductive DC-DC converters. They do not operate in high magnetic fields in the tracker volume of H1;
  - capacitive DC-DC convertes. They do not provide enough power;
  - linear regulators. They have a high power dissipation, but they are, nevertheless, used for every supply line individually to reject the pick-up noise from the long power cables.
- The signals transmitted from the hybrid are driven by 200  $\mu$ A current sources inside the ASIC. Ultra-fast comparators MAX964EEE [59] convert the current pulses into CMOS signal levels. The internal hysteresis loop of these comparators was not sufficient to compensate for their parasitic output-to-input feedback. An additional phase shift circuitry for incoming trigger pulses was therefore implemented.
  - The trigger data are transmitted to the H1 CDAQ via a screened 16-way cable. Differential line drivers AM26LV31 and their complementary receivers AM26LV32 [60] provide a maximum transmission rate of 40 megawords per motherboard and per second.
  - The JTAG protocol [61] was chosen to configure the FPGAs and their EPROMs. This electrical standard allows the exchange of the default and the pilot firmware during the trigger system operation.

The circuit diagram was developed using "OrCad" v.9.1. The draft which included a detailed positioning of board components and a critical routing of the high voltage and high frequency signals was prepared for the layout design and the global wiring was passed to the commercial company.

### 3.4.2 Slow Control Processor

The controller realized on the "ACEX" chip handles supply voltages for the pad modules and sequencer codes and threshold voltages for the readout chips (see appendix A.1.2). For each single task this program includes subroutines which are executed step by step in a single loop. Every subroutine has a flag (one bit in the control register) to enable or disable the procedure call. The user may set or clear these flags and, hence, enable or disable commands. After the last action the processor goes into an idle state and waits for a "wake up" signal which then launches the next loop.

Subprogram arguments, like threshold values and ASIC parameters, are stored in a random-access memory (RAM). Each time the user changes the RAM content, a handshake signal for the processor is automatically generated. Optionally, the ASICs settings which are read back could be compared to the source data and the corresponding matching flags are assigned to a status register which contains also the watchdogs for the supply voltages. One register contains an identifier code which is unique for every new system configuration. The status word and the identifier word are being readout and included in the H1 event data. The design for the slow control processor was compiled in "Quartus II" [53] software developer packages with the entry code written in the VHDL.

### 3.4.3 Data Reduction Processor

The data reduction algorithm implemented on the "APEX" chip performs the synchronization of the detector pulses, pipelining of the raw data, comparing the input trigger word to a stored pattern from the database and coding the output information.

The synchronization scheme provides a timing gate for the detector pulses with different phases which scatter in the range of 50 ns. Signals from two different bunch crossings may potentially affect the trigger decision, therefore the synchronization is based on the following:

1. A trigger signal starts with a high-low level transition (leading edge of the pulse). This definition helps also to suppress bad channels, which drive a permanent low level.
2. All signals are registered only within a time interval (gate), which does not exceed one HERA bunch crossing.

The "gate" is started by the earliest trigger pulse and closed by a signal derived from the HERA clock frequency. The delay of clock pulses provides a variable gate width. After passing the synchronization module all signals have uniform width and phase, fig. 3.8.

The whole trigger information (the raw data) is stored in the front-end pipeline which depth allows for keeping data before and after the "T0" bunch crossing. A memory write enable signal, the so-called "Pipeline Enable" ("PEN"), is driven by the H1 central trigger.

A matching scheme for tracks is based on a set of masks stored in a content addressable memory (CAM) for fast multiple searches. This is, basically, a look-up table (LUT) with a possibility to write, exchange or erase the memory content. The CAM capacity needed per one motherboard amounts

to 1024 32-bit records (masks). These records are obtained from the trigger simulation and from the offline data analysis.

The CAM module supports "don't care" values for masks. This allows for seeking for the whole mask entirely and also for smaller mask patterns. Signals from any three, two and even one plane could be used to make the trigger decision. Therefore more than one signature is programmed for every possible track to provide higher trigger efficiency.

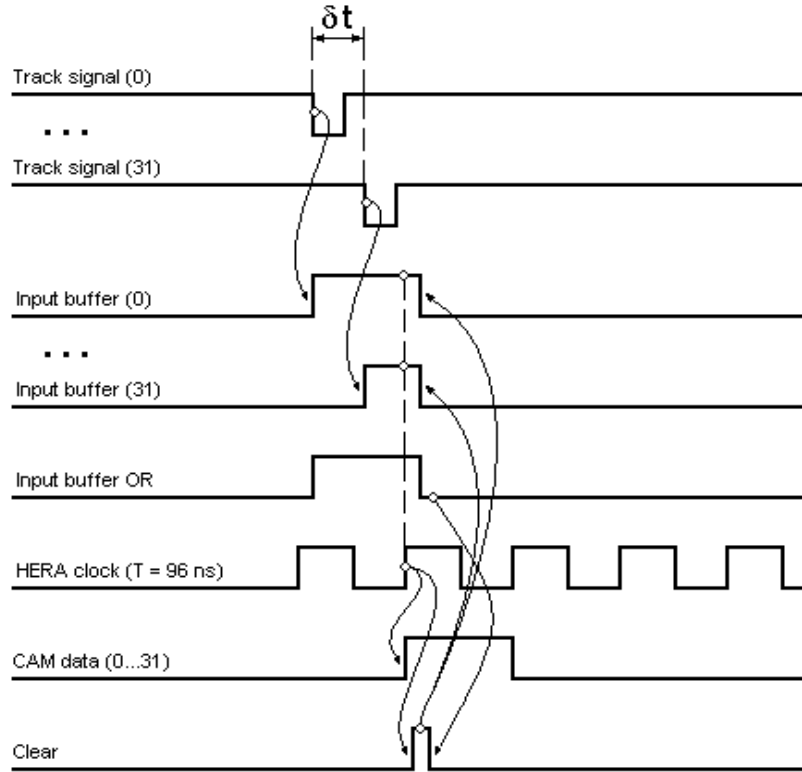


Figure 3.8: Synchronization of trigger pulses: despite their walk and timing jitter the CAM input data are "standardized".

The data output from the front-end is performed in two stages. When the first level trigger is transparent for subdetectors, the "PEN" signal is active and the data reduction processor is sending out hit multiplicities for pads or topology data, i.e. polar angles  $\theta$  of validated tracks. It allows for the master card to make a fast trigger decision. Alone or in combination with any other trigger elements, the BST L1 decision could be accepted by the H1 central trigger. Afterwards the "PEN" goes low, the readout phase starts and the front-end pipeline content (the raw data) is multiplexed to the output. Some other subroutines: the H1 radiation monitor, the hit multiplicity check and

the recognition of upstream tracks, were added to the main trigger program. The design for the data reduction processor was compiled using "Quartus II" with the entry code written in VHDL.

### 3.5 VME Interface Modules

The following VME modules are interfacing the Pad detector to the H1 CDAQ and to the H1 central trigger system [62]:

Two **repeater cards** untie high density cables coming from the detector, adapt signal levels to the H1 standard, provide the data fanout for the PQZP store cards, the L2NN receiver card and the BST-Pad master card described below, distribute and delay the HERA clock frequency and H1 control signals all over the BST-Pad and prepare the "front-end ready" (FER) acknowledge.

The "**store cards**" of the standard H1 PQZP system [63] are used to keep the BST-Pad topological data during the H1 sampling phase. On demand of the central DAQ their full content can be read out via the VME bus into the "TSCD" bank #12. With an event announcement the PQZP sampling stops and the L2NN starts latching the raw data available<sup>2</sup> which are stored thereafter into the "T2PQ" bank #513 (this L2NN receiver card is not installed yet, therefore the bank is temporarily absent). The L2TT receives the T0-relevant data from the PQZP through the port #5 and writes them via the VME bus into the "T2PQ" bank #256.

The **master card** unifies data streams from 6 front-end boards and searches for clear track signatures for the level-one trigger. It is done by selecting events with not more than  $N$  tracks ( $1 \leq N \leq 12$ ) in the whole detector. An exact number should be found from the trigger efficiency studies. A simplest solution applied for searches for the back-to-back candidates as from  $J/\Psi \rightarrow e^+e^-$  for  $N \geq 2$  is a look-up table which validates an offset in  $\phi$  between any two tracks in the transverse direction. A veto signal is generated independently of the track trigger when at least one upstream track in any sector has been registered or when the hit multiplicity is enormously high.

The master card receives the identifier and the status words of the BST-Pad from the front-end via the CAN SLIO interface. On demand of the CDAQ those data are readout into the TSCD bank #12 via the VME interface. The "read" and the "write" functions on the VME bus are programmed for the standard (A24) supervisory and non-privileged data access [64].

Circuit diagrams for the repeater cards and the master card were developed in "OrCad" v.9.1. The firmware design was compiled using "Quartus

---

<sup>2</sup>The complete history could be transmitted, but the actual front-end program does it only for the T0-relevant data.



II” with the entry code written in the VHDL.

### 3.6 Power Supply System

Originally, a ”Hewlett Packard” 6500 series power system (no technical information is provided by the supplier) was planned to supply the BST-Pad. It has a modular structure and every module provides a floating and adjustable DC voltage. The principle of operation of each module is based on a high frequency (100 kHz) oscillator and a step-down transformer. Due to a possibly large parasitic capacitance between primary and secondary windings, this transformer shows a high common mode voltage (several volts) induced in the output circuit. When two or more of such supply modules have a common potential (for instance ground), the superposition of the individual common mode voltages becomes critical, because the 100 kHz switches are not synchronized. The pad detector did not operate properly with this type of power supply.

Another modular standard, ”Gossen MSP64” [65], uses 50 Hz step-down transformers and the common mode effect is much less due to the low operating frequency. The disadvantage of this device is a digital voltage control which interferes with all internal circuits including the output power rails. Therefore a new power supply system was developed based on the following technical requirements:

1. Every front-end board has an individual supply module;
2. All voltages in this module arise from a common transformer;
3. Transformers operate at low frequency (50 Hz);
4. Analog voltage control is used (no clocked circuits etc.).

With special attention and care the filtering of the primary AC voltage and of the output DC voltage was realized. The noise performance of the trigger system was the criterion to optimize the power supply design. A threshold scan (see chapter 3.3.3) was performed for different versions of the detector power supply: the designed module, accumulator batteries and ”Rohde-Schwarz NGT20” voltage source [66], fig.3.9. At small threshold values the designed power supply looks similar to the ”NGT20”. Both are better than batteries because the latter supply has always a high inner resistance. Over a wide threshold range the BST-Pad power system becomes more ”clean” than the ”NGT20” due to a careful board layout.

One additional module was designed for the depletion voltage supply. This source provides a "high voltage" (0...70) V in six galvanically isolated channels. The circuit diagram and the layout for the whole supply system was developed in "OrCad" v.9.1.

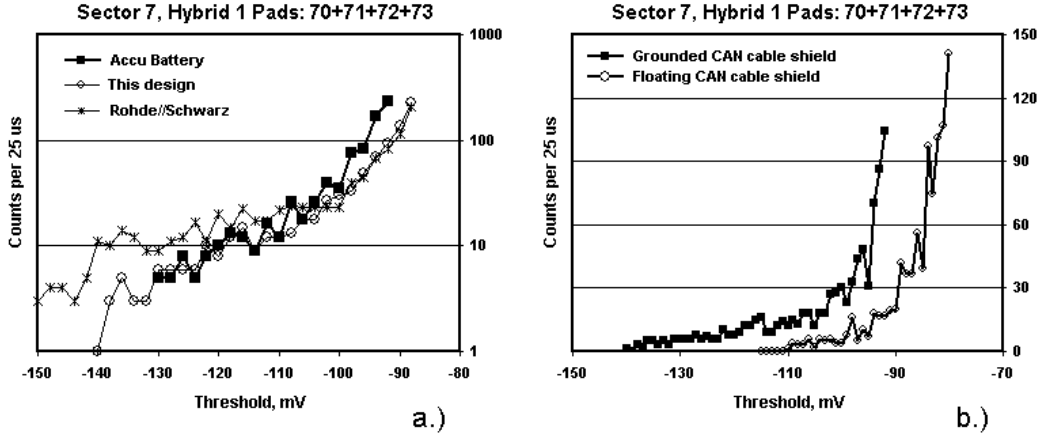


Figure 3.9: a.) Threshold scan with different supply sources and  
b.) influence of the shielding scheme.

### 3.7 Operation Experience

First experience with electronics functioning in a high radiation field (up to 3.2 Mrad =  $3.2 \times 10^4$  Gy accumulated in 1.5 years), was not trouble-free. After radiation accidents some BST-Pad control functions were lost due to equipment refusals. Front-end access for repairing requires a time consuming H1 facility dismount. A software (!) solution was found and the problem could be fixed remotely. A few rules-of-thumb were extracted for the detector upgrade and for the future front-end design:

1. The operating regimes of circuits should rely on ceramic resistors and capacitors. Semiconductors should have sub-micron technology to minimize radiation damage effects;
2. Analog circuits should have 100% feedback, i.e voltage repeaters must be used rather than amplifiers. In any case the digital circuitry is preferable because it operates with two robust signal levels;
3. As much functionality as possible should be implemented into the program algorithm. It is always easier to recompile the design activating new FPGA resources than to repair the hardware.

The front-end of the new detector is based on commercial electronical components. Ensuring their reliable operation in the environment with radiation is a complicated task, therefore the online HERA background control and the fast response on radiation effects in the silicon become very important to keep the exposure rate below 100 Gy/year.

# Chapter 4

## Test Beam Results

Test measurements were performed for the silicon sensors at every stage of the BST detector construction. The procedure of measuring their bias current and break-through voltage and of checking their decoupling capacitors was described in [67].

A series of measurements of DC-regimes and response to high frequency input signals was performed for the readout chip and the hybrid prototype before the series production of the detector modules started. A variety of experimental approaches was tried out in order to achieve better accuracy of the amplitude analysis to gauge energy deposits in the detector. All of these methods provided equivalent results for the detector energy resolution:

- Electrical charge injection via the special ASIC's calibration input;
- Flashing a laser pulse onto a photodiode used as a silicon pad;
- Irradiating the silicon sensor by  $\gamma$ -quanta,  $\beta$ -particles and beam electrons.

The calibration pulse method was used for main reference tests of the detector modules. A special adapter card similar to the front-end board was developed. Additional analog outputs of this adapter allowed for a direct amplitude analysis. A digital oscilloscope "Tektronix" TDS-754C [68] was used in the "histogram" mode as an analysing tool, fig. 4.1. The dynamic range and the equivalent noise charge (ENC) of the readout chip, the signal-to-noise ratio for 4 fC pulses, pile-up effects for frequent signals and the long term and temperature stabilities were studied for the hybrid prototype under laboratory conditions prior to a beam test.

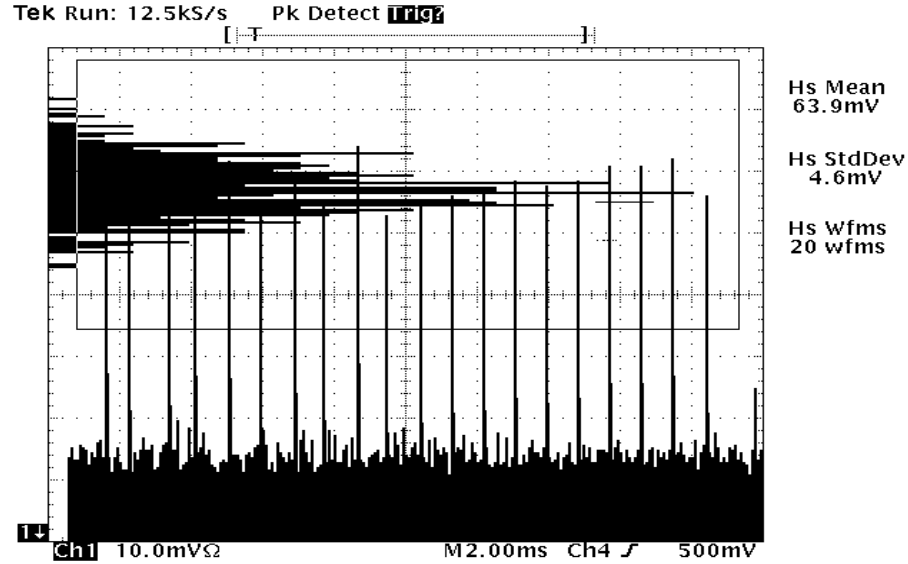


Figure 4.1: The amplitude measurement with the TDS-754C oscilloscope. Peak voltages above a certain threshold are histogrammed in a long time scale and the mean amplitude and its standard deviation are online computed. Horizontal box margins set threshold voltages and vertical ones – the acquisition time.

## 4.1 Beam Experiment

The performance of the pad hybrid prototype was measured with a 5 GeV electron beam at DESY Hamburg. The advantages of accelerated particles compared to radioactive sources and cosmic rays are:

- The beam has a well-defined direction;
- Small divergence and easy focusing;
- Large energy range close to HERA conditions;
- Precise timing and coherence;
- High particle flux is reachable.

The beam test allowed for modelling of a pad trigger system and investigating its efficiency and stability. Calibration measurements were performed for more than 50 assembled pad modules prior to their installation on the BST wheels.

### 4.1.1 Experimental Test Setup

The test detector assembly consisted of three modules in one  $\phi$ -sector ( $22.5^\circ$ ) mounted along the beam axis with 50 mm distances between them, fig. 4.2. Each module consisted of a series type pad sensor assembled onto a prototype hybrid.

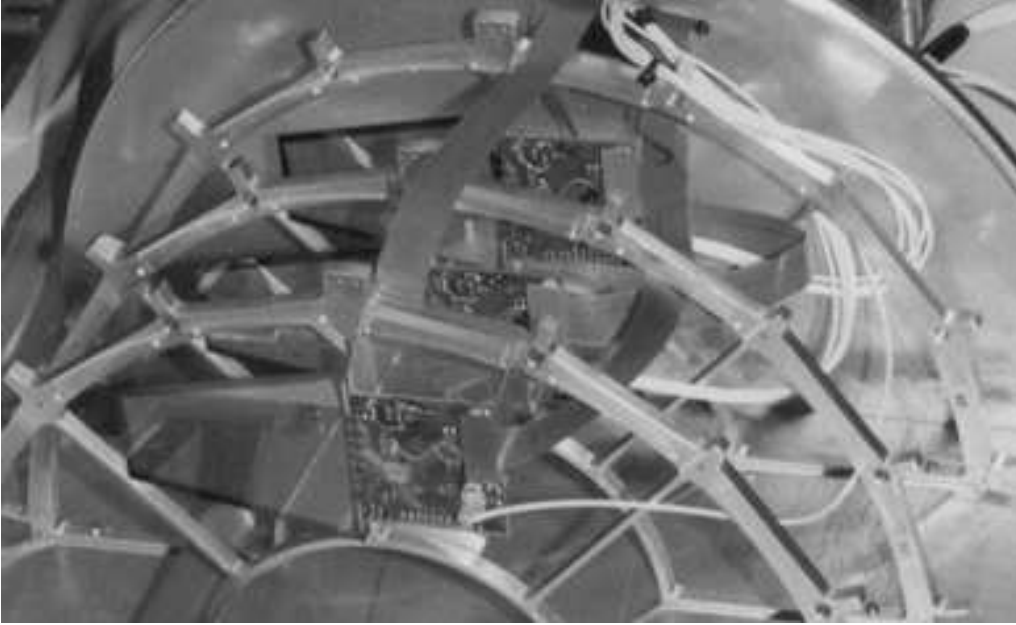


Figure 4.2: Pad detector telescope for the test beam.

Analog signals from electrons and their discriminated trigger pulses were buffered and transmitted via 40 m long cables to the data acquisition system located in the radiation safe area. Several "Rohde-Schwarz" NGT-series power supply units provided floating voltages for the silicon sensors, hybrids and the front-end electronics.

The block diagram of the data acquisition system is shown in fig. 4.3. The amplitude analyzer was based on the "LeCroy" 2249A analog-to-digit converter (ADC) [69] in the CAMAC modular standard. During trigger efficiency studies the CAMAC counter ZFK 5300<sup>1</sup> was used to sum up discriminated detector pulses. The CAMAC digit-to-amplitude converter (DAC) ZFK 5321 provided threshold settings for the detector modules. The C.A.E.N. N93B NIM-timer [70] formed gate signals for the counter and for the ADC.

---

<sup>1</sup>No technical information is provided on ZFK-series modules.

The original software in the "LabView" format was developed for the "Quadra 840AV" Macintosh PC to readout the ADC, to preprocess and visualize the data and to store the information on the hard disk. Another program was written to operate DAC thresholds and to start the counter readout after some relaxation time. The computer strobe starting the new measurement was sent to the trigger system via the C.A.E.N. V262 register. This was a multi-purpose VME module and hence used by the third program to download PRO/A sequencer codes. The trigger logic included combinatoric circuits, delay units and level converters in the NIM standard.

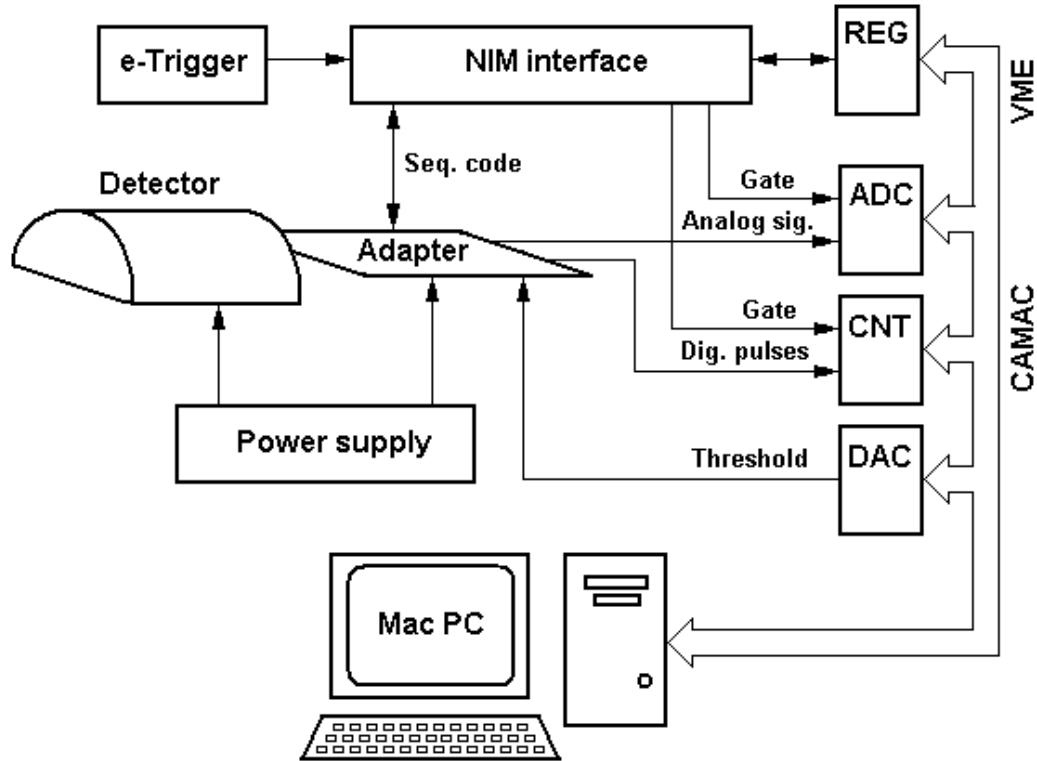


Figure 4.3: The hardware setup for the pad hybrid beam test and calibration.

#### 4.1.2 Electron Tagger

A secondary beam of electrons produced at the "DESY-2" synchrotron was used for test purposes. Here an internal  $10 \mu\text{m}$  thin carbon target is placed on a primary particle orbit, converts some fraction of accelerated electrons into electron-photon showers. With a deflection magnet and a collimating system the charged and the neutral components of these showers are separated and the secondary electron beam is shaped.

A variable magnetic field strength allows for an electron energy selection between 1 and 5 GeV. The collimator had a square  $(1 \times 1) \text{ cm}^2$  aperture. The beam axis was found precisely with two scintillation counters placed at distances  $Z1 = -5.0 \text{ m}$  and  $Z2 = -6.5 \text{ m}$  from the collimator's plane. Every counter consisted of two organic scintillators, one vertically and another horizontally oriented, with an active area of  $(2 \times 1) \text{ cm}^2$  each. The second counter had an additional  $(5 \times 5) \text{ cm}^2$  scintillation plate with a centered hole of 1.5 cm diameter, fig. 4.4, to veto electron-photon showers originating from the test setup.

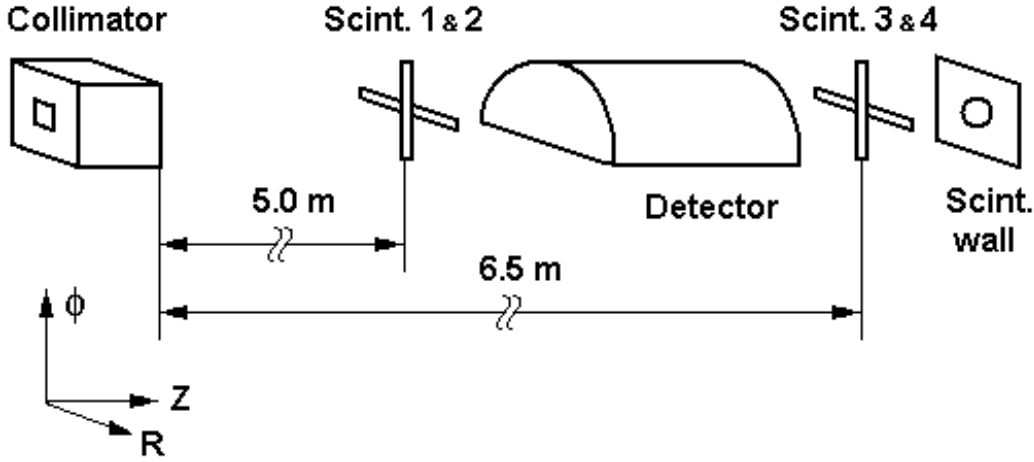


Figure 4.4: Beam line definition with 4 scintillation counters.

The track trigger was defined as a signal coincidence from all four scintillation rods and the scintillation wall could give a veto signal. The maximum trigger rate observed was about 100 Hz, but mostly it stayed at a few Hz level. A disadvantage of this trigger signal was its 200 ns delay with respect to all pad pulses which, therefore, had to be delayed as well.

#### 4.1.3 Detector Alignment

The pad detector test setup was mounted on a moveable platform between scintillation counters. A beam profile was scanned using the eight rings of pads of the detector modules themselves. This enabled their alignment in the laboratory system. The number of discriminated pulses from the beam electrons was counted for every single pad as a function of the ring number, fig. 4.5, and the azimuthal angle  $\phi$  disabling other channels. All counts were normalized to the same number of beam trigger pulses. Initially all thresholds were set to -120 mV to provide a noise frequency below 0.1 Hz.



The readout chip on the first hybrid had a common threshold shift which degraded the detector performance and led to smaller statistics. Afterwards this offset was determined and corrected by means of a threshold scan.

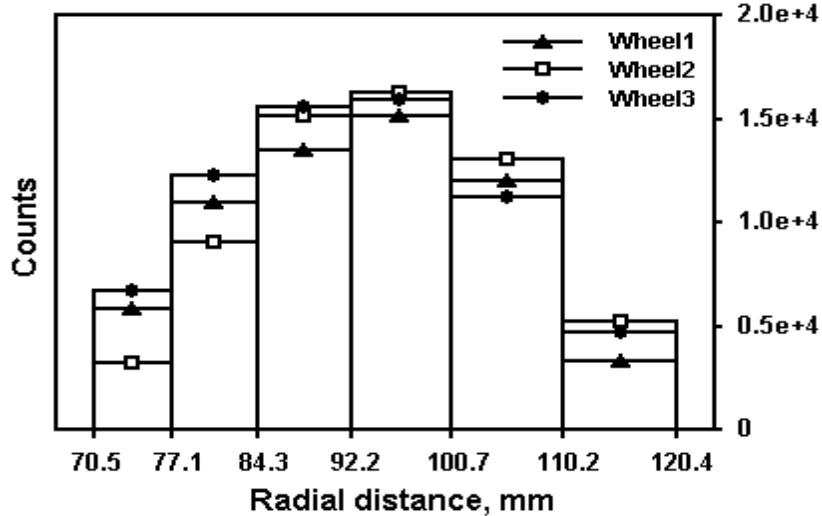


Figure 4.5: Beam profile in the horizontal plane as measured with three consecutive pad detectors in the DESY test beam.

The non-uniform pad size introduces a bias to the beam position  $\bar{X}_{simple}$  calculated as a simple average over all events histogrammed in fig. 4.5, therefore the weighted mean techniques [71] was utilized. The spatial distribution of the beam particles (beam profile) is approximated by a Gaussian, therefore the event weights  $w_{event} = 1/\sigma_{event}^2$  provide the smallest variance of the mean estimate, where  $\sigma_{event}^2 = \sigma_{instr}^2 + \sigma_{beam}^2$ . For every detector ring of the width  $D_{ring}$  its instrumental uncertainty is found as  $\sigma_{instr} = D_{ring}/\sqrt{12}$  because of the uniform response function of each pad.

The beam uncertainty  $\sigma_{beam}$  common to all events is derived iteratively from the quadratic errors  $(\bar{X} - X_i)^2$  starting with  $\bar{X} = \bar{X}_{simple}$ , where  $X_i$  is a center of the i-th ring. The numerical tests of this method showed precise results already for the first pass.

The beam intensity had a maximum at  $X = 94.83 \pm 0.05$  mm for the first module,  $94.04 \pm 0.04$  mm for the second and  $92.13 \pm 0.04$  mm for the third. These results indicate an about 1 mm misalignment of at least two sensors with respect to each other and an about  $1^\circ$  tilt of the whole detector in the horizontal plane. The maximum displacement observed between the first and the last sensors, however, was equal to 2.7 mm and thus still less than the size of even the smallest pads.

## 4.2 Measurement Programme

### 4.2.1 Analog Amplitude Measurements

The aim of this study was an amplitude analysis of genuine MIP signals in the silicon sensor. For relativistic electrons their amplitude distribution was obtained with a single detector module in self-triggering mode. In practice this means that the trigger pulse launching the ADC is derived from the same signal to be measured. The choice of a low discriminator threshold was very important for the minimum bias trigger to find the true peak position in the analog spectrum, fig. 4.6.

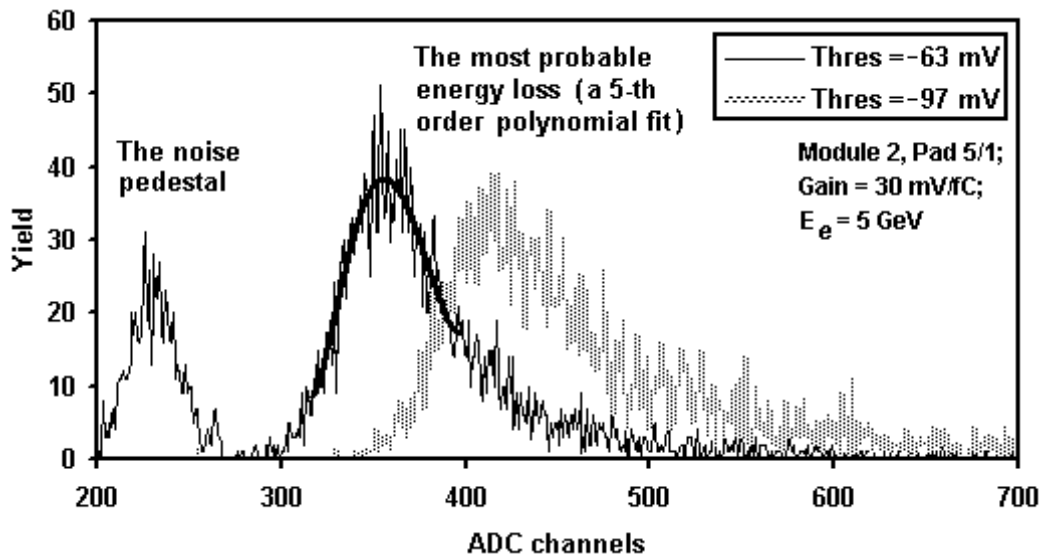


Figure 4.6: Analog signals from 5 GeV electrons crossing perpendicularly a pad detector. The first spectrum (solid line) has a real peak which corresponds to the most probable amplitude. It is separated well from the noise pedestal. The second distribution (dotted line) is just a high-energy tail of the first one with some amplitudes below the threshold due to the discriminator uncertainty.

In contrast to the calibration pulses, the spectrum of energy losses of relativistic electrons is not a Gaussian distribution. According to the Landau Theory it has a long tail to the high energy side due to some probability of a large energy transfer in a single collision of the beam electron with one of the silicon atoms. The mean energy loss on this curve thus no longer corresponds to the peak which is now called the "most probable energy loss". This latter

quantity, determined with a polynomial data fit, was used to parametrize the distribution [72].

The MIP signal for pad detectors was estimated as the most probable amplitude minus the ADC pedestal. This pedestal voltage measured with a random trigger and with no beam obeys a Gaussian distribution law. The ENC is defined, therefore, as one standard deviation of this distribution. The S/N-ratio is calculated as one MIP signal over the ENC. Proper settings of the detector depletion voltage ensure the maximum signal swing while the choice of the FOXFET gate voltage is essential for the ENC [73].

Signals available at analog outputs of the readout chip can be externally shaped and filtered prior to the trigger discriminator in order to see how optimal the amplifier part of the ASIC design is. The main advantage of a direct amplitude measurement, nevertheless, is a small systematic error as compared to the indirect finding from the threshold scan. This latter requires accumulating of a large number of discriminated pulses. The probability to count additional noise pulses increases at low threshold values, which is not the case for the analog method where the threshold is fixed, and provides equivalent conditions for the low-noise studies which are summarised in fig. 4.7.

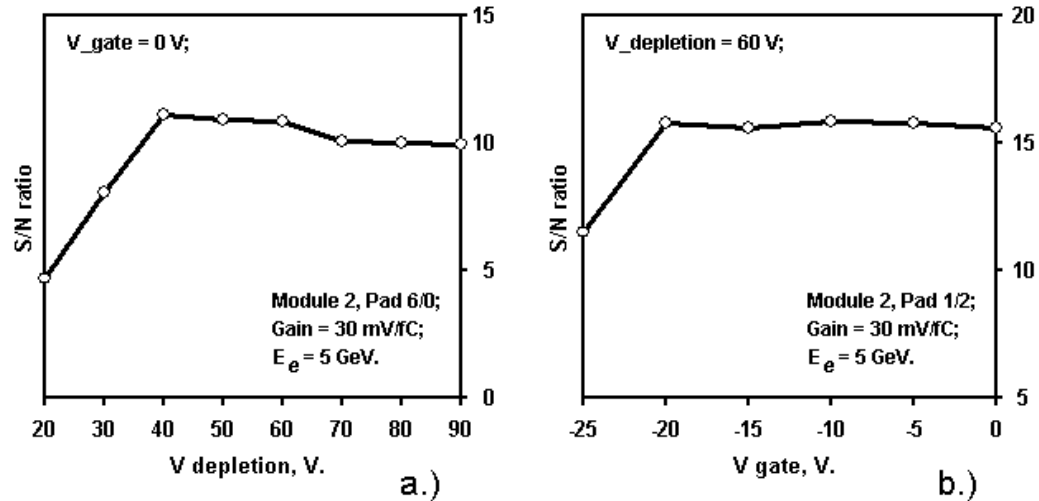


Figure 4.7: S/N vs. depletion a.) and FOXFET gate b.) voltages

Extended amplitude measurements supported the hybrid design optimization. The prototype included a number of stabilizing capacitors for the bias voltages to ensure stable operation of the readout chip. Removing those one by one from the hybrid prototype in the test beam measurements no degradation of the detector performance was observed. This led to a greatly simplified final hybrid layout.

### 4.2.2 Track Trigger Efficiency Studies

The large S/N-ratio observed for MIP signals allows a free threshold choice within some limits where still all incoming particles can be registered – the so-called "plateau" on the threshold scan curve. The number of counts on the plateau gives an estimation of the single detector efficiency which was found to be very close to 100%. The efficiency of a group of detectors, however, depends also on their alignment and on their synchronization scheme.

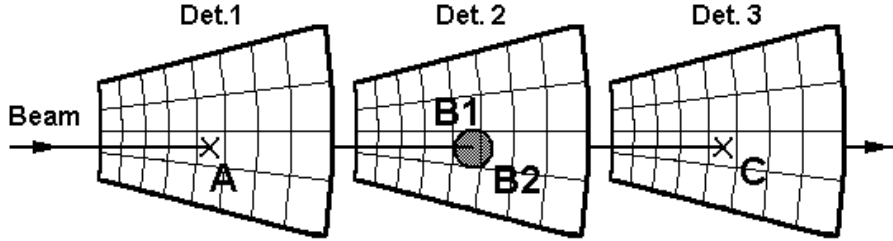


Figure 4.8: The masks, i.e. combinations of pads  $A \wedge B1 \wedge C$  and  $A \wedge B2 \wedge C$  are allowed for the chosen track topology.

As an example, the trigger efficiency was measured for tracks defined with hits in the three layers. The beam spot was focused onto single pads of the first and the third sensors and by chance, the particle could cross two pads in the middle plane, fig. 4.8. The number of tracks recognized separately by every of two masks and also by their combination was counted and normalized onto the number of trigger events. Because of the beam spread the partial efficiencies for these masks are low, but their mutual value exceeds 95%, see table 4.1. Within error limits the measurement result matches an expected efficiency with two complementary masks.

Table 4.1: Relative number of tracks in the silicon telescope measured using the setup shown in fig. 4.8 for different threshold settings of the middle detector. The symbol " $P_{N1+N2}$ " denotes the sum of two probabilities  $N1$  and  $N2$ .

Threshold, units (mV)	N1 (%): $A \wedge B1 \wedge C$	N2 (%): $A \wedge B2 \wedge C$	$P_{N1+N2}$ (%):	N3: (%) $A \wedge (B1 \vee B2) \wedge C$
40 (-71)	$61.3 \pm 1.5$	$32.7 \pm 1.5$	$94.0 \pm 3.0$	$95.8 \pm 0.6$
50 (-97)	$60.3 \pm 1.5$	$26.2 \pm 1.4$	$86.5 \pm 2.9$	$94.6 \pm 0.7$
60 (-123)	$61.8 \pm 1.5$	$29.7 \pm 1.4$	$91.5 \pm 2.9$	$91.0 \pm 0.9$

The count of tracks  $N$  obeys the binomial distribution law with the mean value  $\mu_N = pT$  and variance  $\sigma_N^2 = T \cdot p(1 - p)$  where  $p \equiv \varepsilon$  stands for the detector efficiency and  $T = 1000$  is the number of beam triggers. The sample proportion  $N/T$  is therefore an unbiased estimator of  $\varepsilon$ . The variance of  $N/T$  is equal to  $\sigma_N^2/T^2 = p(1 - p)/T$ , hence the absolute error bars for measurements are calculated:

$$\sigma(N/T) = \sqrt{N(T - N)/T^3} = \Delta_\varepsilon \quad (4.1).$$

Table 4.2: Comparison of two types of synchronization.

Timing scheme	$N_A$ (%)	$N_B$ (%)	$N_C$ (%)	$P_{A \wedge B \wedge C}$ (%)	$N_{A \wedge B \wedge C}$ (%)
Simple coinc.	97.6	99.1	99.5	96.2	$94.1 \pm 0.7$
Latch & coinc.	$\pm 0.5$	$\pm 0.3$	$\pm 0.2$	$\pm 0.6$	$96.2 \pm 0.6$

The result for the trigger efficiency was obtained with a simple coincidence of discriminated pad signals. Additional 2% can be gained with a refined synchronization scheme invented when the phase of these pulses is standardized, table 4.2. With these fine tunings an efficiency of about 96% was obtained, fig 4.9.

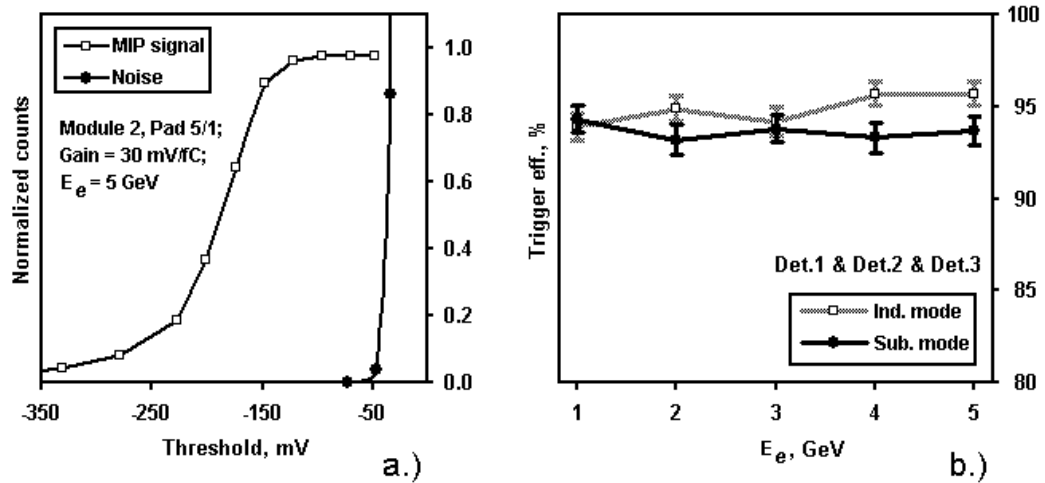


Figure 4.9: a.) Typical signal and noise curves in the threshold scan; b.) trigger efficiency vs. variable electron energy.

### 4.2.3 Detector Calibration

Calibration measurements were performed for assembled detector modules. With 5 GeV electrons a threshold scan was done for every individual pad. The plateau width determined in this section was a measure to control the detector quality, fig. 4.10-a. and to select efficient modules, fig. 4.10-b. with a plateau larger than 10 mV. This allows a reliable setting of the operational threshold voltage just above the noise. For these measurements the so-called "internal" trigger signal was defined by two outermost silicon sensors.

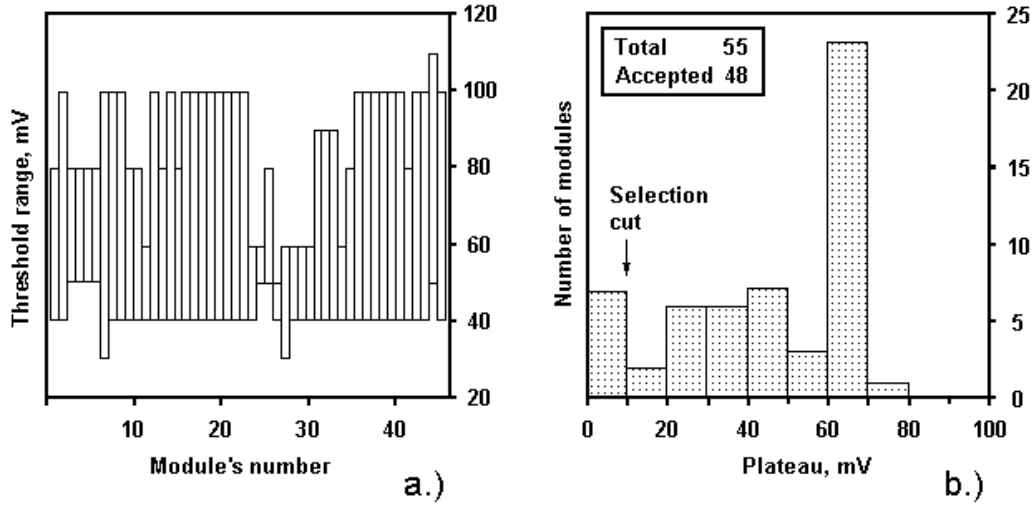


Figure 4.10: a.) Threshold ranges where the trigger efficiency stays high (the detectors with a zero plateau width aren't shown);  
b.) the detector's selection relying on the plateau width.

Out of 55 tested modules 48 could be selected. For the remaining 7 detectors there was, essentially, no plateau observed during the beam calibration. Their counting rates for MIP signals were comparable small even at low thresholds until the noise slope reached. These observations were common to all pads of those wafers. It was found that all these problematic sensors had a very high drain current  $\approx 1 \mu\text{A}$  as compared to 10...100 nA for the normal detectors.

Such an efficiency decrease can be treated as being inherent to the silicon common mode noise (CMN) with one difference compared to stochastic noise that it doesn't cause any false signals, but suppresses the trigger, instead. Additional trigger masks known from the section 2.2.3 as permutations are supposed to compensate the inefficiency of such pad detectors in case of their usage for the trigger as spares.

### 4.3 Conclusion

Preparation to the beam test made a great contribution to the front-end hardware design and the slow control software development for the BST trigger system. Parameters of pad detectors with new and recycled silicon sensors were measured. During this test 48 well functioning modules with predetermined thresholds could be selected.

The algorithm of the test beam profile scan with the pad detectors can be applied for their alignment in the H1 coordinate system with a reasonable statistics for the well-defined tracks in the BST angular acceptance. The information about those tracks can also be used to study the trigger efficiency of the BST-Pad inside the H1 facility.

# Chapter 5

## Data Analysis

After installation and solving the main experimental problems for the BST functionality regarding stable power supply or slow control as described above, the pad detector was running in H1. This operation suffered very much from the high HERA background conditions in the initial phase of HERA II which destroyed a large part of the detector. The development time and effort needed to be shared between monitoring the radiation and developing the BST-Pad became the main experimental task. There were three distinct periods of data taking with the pad detector to investigate its efficiency, timing resolution, etc.:

1. Efficiency studies for a single detector module: with identified positrons in the backward region of H1 a threshold scan was performed for two silicon sensors and their trigger efficiency was measured whose dependence on the threshold voltage was similar to the beam test results.
2. Raw data recording from the whole pad detector with a random trigger for minimum bias conditions. These data allow for the offline reconstruction of tracks and their comparison with simulation results. The detector information for several time slices is kept in the pipeline and then read out to study synchronization of pulses from different BST-Pad planes.
3. Efficiency measurement for a set of masks: the complete trigger algorithm has been started and two L1-trigger elements of the BST, the track trigger and the high multiplicity veto were investigated.

The amount of information per event in measurements from 1 to 3 increased for the BST-Pad, therefore three different configurations of the front-end with enhanced complexity of the data transmission algorithm have been applied for those experiments because of the limited readout bandwidth of the Pad system.



## 5.1 Single Plane Efficiency Studies

The trigger efficiency of each detector module is determined as a ratio between the number of tracks passing through the silicon sensor and the number of tracks validated by the pad detector itself. This ratio was measured with different threshold settings for the readout chip in order to find a safe range (plateau) of the operational voltage.

A track candidate for the scattered positron is defined by two space points, which are 3-dimensional coordinates  $(x_V, y_V, z_V)$  of the event vertex and the energy cluster position  $(x_S, y_S, z_S)$  in the SPACAL. The straight line fit can be used for the particle trajectory down to a few GeV of energy of the scattered positron. Therefore the particle coordinates,  $(x_B, y_B)$ , when crossing one of the pad  $z_B$ -planes, are found as:

$$x_B = x_V + (x_S - x_V) \cdot (z_B - z_V) / (z_S - z_V) \quad (5.1)$$

$$y_B = y_V + (y_S - y_V) \cdot (z_B - z_V) / (z_S - z_V) \quad (5.2)$$

The track candidate is accepted if these  $(x_B, y_B)$  coordinates fit into the silicon sensor active area. During luminosity operation of HERA the positrons are scattered into a large solid angle of the H1 detector. In the trigger efficiency measurement this leads to rather lower statistics for each individual pad. The threshold dependence has thus been investigated for the entire silicon sensor with all pads enabled. Their global "OR" function helps to prevent the double counting of hits.

The number of the output channels of each motherboard allows two detector modules to be read out simultaneously in every HERA bunch crossing. Two adjacent detectors in the first  $z$ -plane were chosen as they cover the largest possible angular acceptance in  $\theta$ , fig 5.1.

The "T0" data from the silicon pads were stored in the PQZP system. The minimal pipeline depth  $PD_{Pad}$  for the BST-Pad:

$$PD_{Pad} = T_{L1} - \Delta T_{Pad} \quad (5.3)$$

has to be greater than or equal to 21 time slices. The period  $T_{L1}$  of the H1 sampling phase amounts to 24 HERA clock periods ( $2.3 \mu s$ ). The sub-detector's delay  $\Delta T_{BST}$  includes a delay of the synchronization algorithm (described in the chapter 3.4.3), transition delays of the buffering logics and signal delays of the data cables. It is estimated to be 3 or 4 HERA clock periods depending on the phase shift of the synchronization frequency, see appendix A. With a chosen pipeline depth for 28 HERA bunch crossings, most of the pad signals were found in the 21-st time slice propagated backwards (to the past) from the "L1Keep" decision time of the CT. Thus the timing scheme of the pad detector has been verified.

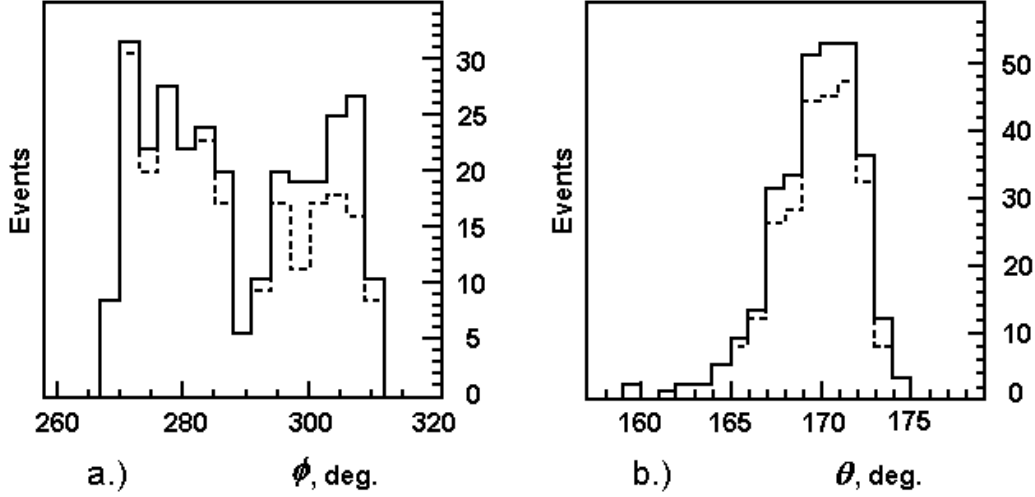


Figure 5.1: Angular acceptance in  $\phi$  a.) and  $\theta$  b.) of two detector modules Nr. 16 and Nr.17 used for the trigger efficiency measurements (detector alignment is not yet done). The solid line shows the total number of track candidates and the dashed one - events, which contain signals from pads.

### 5.1.1 Data Selection

The data for single plane efficiency studies was taken in February 2003. The integrated luminosity for this period amounts to  $110 \text{ nb}^{-1}$ . Most of the H1 sub-systems were included in the CDAQ readout. Whereas the high voltage (HV) power supply is always provided for the H1 calorimeters, it is turned on for the tracking detectors only after the background situation in HERA has been optimized. The run numbers for good operating conditions and reasonable amount of data collected are summarised in table 5.1.

### 5.1.2 Fiducial Cuts

Besides the "S0" or "S9" trigger conditions for the scattered positrons the following additional cuts on reconstructed event variables have been applied:

- The event  $z$ -vertex, fig. 5.2 a.), has to be in the range  $\pm 30 \text{ cm}$  from the nominal position that corresponds roughly to  $\pm 3\sigma$  Gauss (the effect of the vertex smearing described in 2.2.3). This allows for a background suppression of non relevant physical processes (beam-gas, beam-wall scattering etc.);
- The event vertex has to be reconstructed in central trackers (vertex type = 1) with precision  $\Delta z$  not worse than  $5 \text{ cm}$ , fig. 5.2 b.). This parameter enters the systematic error on efficiency measurements;

Table 5.1: Raw data sample for the pad detector study with variable threshold settings.

Threshold, mV	Run Nr.	L4 Events
-72	341274, 341275	33775
-78	341267, 341269, 341272, 341273	134333
-80	341478, 341480, 341481, 341487, 341488, 341494, 341495, 341497	219533
-85	340856, 340857, 340858, 340859, 340860, 340869, 340870, 340872	128097
-100	340874, 340875, 340877, 340905, 340907, 340908	124136
-110	340910, 340941	63981
-115	340878, 340879, 340881, 340882, 340885	79248
-120	340942, 340946	92362
-130	340948	23443
-140	340954, 340967	105385

- The energy deposit  $E'_e$  in the electromagnetic SPACAL has to be larger than (15...20) GeV, fig. 5.2 c.), and the radius of the SPACAL cluster  $r_{CL}$  should not exceed the calorimeter cell size (4 cm), fig. 5.2 d.), to reject signals from  $\gamma$ -quanta or hadrons originating in photoproduction or in hadronic decays.

### 5.1.3 Detector Alignment

In order to minimize the systematic error on the efficiency measurement where the number of track candidates depends on the BST-Pad acceptance, the CJC, the SPACAL and the pad detector have to be aligned with respect to each other. By convention the H1 coordinate system is defined by the central tracker, therefore the SPACAL has been aligned first with respect to the CJC and then the BST-Pad position in between was estimated.

#### SPACAL Alignment

Increased scattering angles of positrons make their track selection in the BST aperture more critical to a parallel shift of the SPACAL and the pad detector in the  $x$ - $y$  plane. The SPACAL offset can be found exploring Compton scattering [74]. This reaction has two products in the final state: the scattered positron and the bremsstrahlung photon. In the transverse direction they establish  $180^\circ$  opening angle to obey the momentum conservation law. They

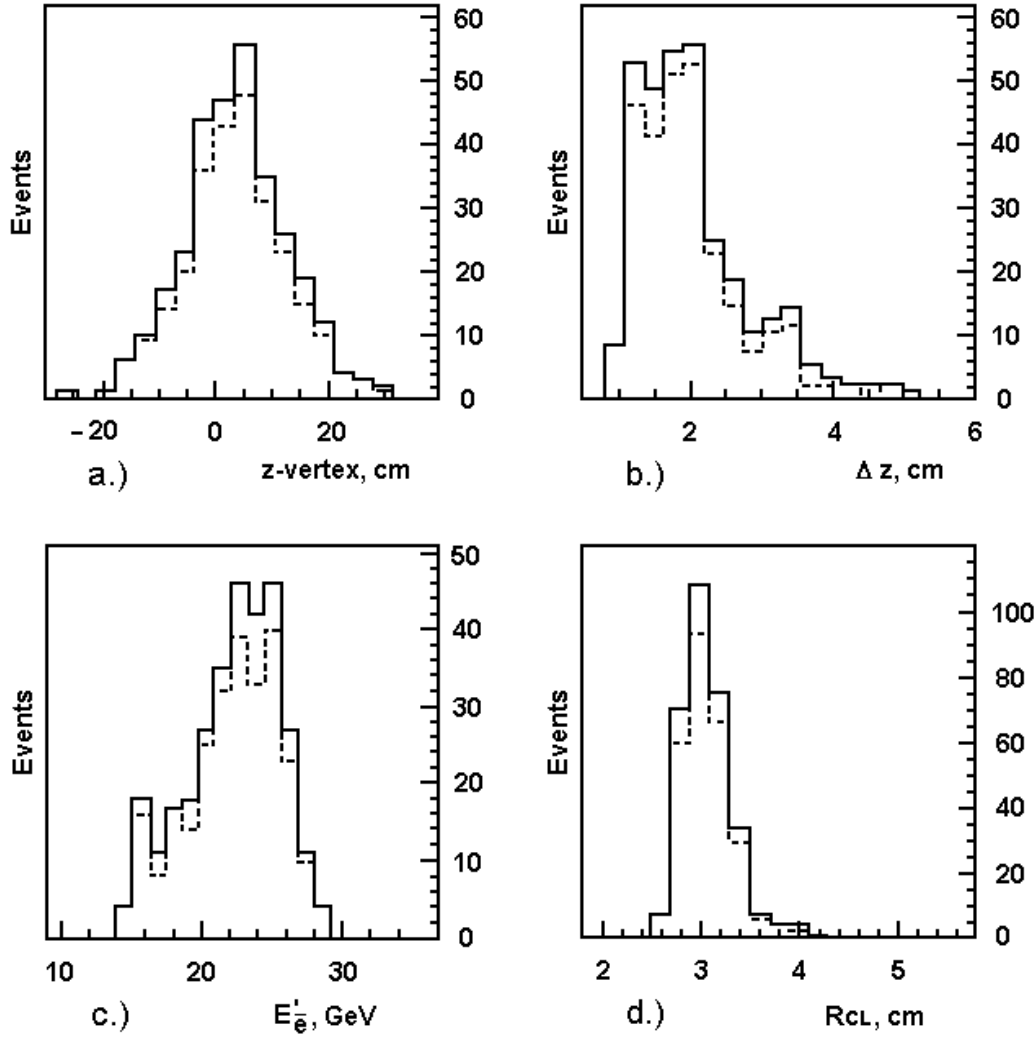


Figure 5.2: Kinematic cuts for the data selection: event vertex range a.) and accuracy of the vertex reconstruction b.), the scattered positron energy c.) and the radius of the SPACAL energy cluster d.). The solid line shows all selected track candidates and the dashed one - only those of tracks which are validated in the pad detector.

can both be registered in the SPACAL and their coordinates have the same bias which can be extracted from a series of measurements. In the data analysis two electromagnetic clusters in the backward calorimeter are required. Their energy sum has to exceed the positron beam energy 27 GeV, but the lower threshold is applied for selection because both baricenters have a measurement uncertainty of a few GeV. These clusters are connected by a line in the SPACAL plane and a number of lines from many events determines the

beam spot position. In fig. 5.3, left part, these lines are shown by dots whose densities along  $X$  and  $Y$  axes are histogrammed on the right side. The shapes of distributions depend on the beam profile in the interaction region and for both the Gaussian fits have been used. Taking into account the beam tilt and the beam shift the geometrical center  $X_0 = (0.1 \pm 0.2) \text{ cm}$  and  $(Y_0 = 0.03 \pm 0.10) \text{ cm}$  of this spot is found from 36 Compton events. To sufficient approximation for the pad data analysis the SPACAL offset has been omitted.

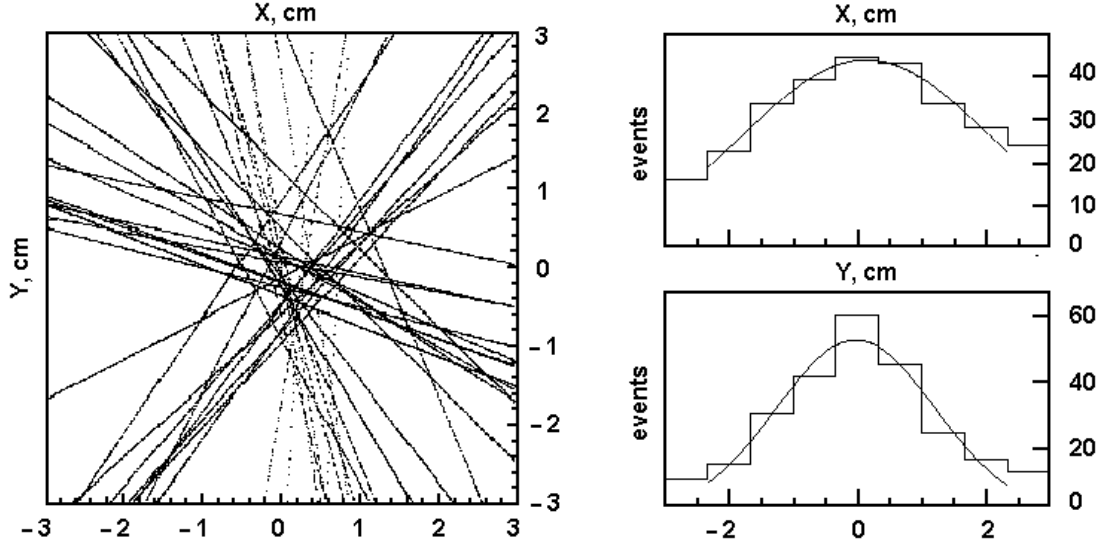


Figure 5.3: Distribution of Compton events in the SPACAL  $x$ - $y$  plane.

### BST-Pad Alignment with Respect to the CJC

The center position  $X_{P0}$ ,  $Y_{P0}$  of each silicon wheel can be estimated with respect to the beam line utilizing the least squares method. For an event containing the vertex as measured by central trackers, the energetic cluster in the SPACAL and the trigger signal from pads, the hit coordinates  $x_i$  and  $y_i$  in the pad detector's plane have been tabulated by formulae (5.1) and (5.2) to fit a function  $R = \sqrt{(x_i - x_{P0})^2 + (y_i - y_{P0})^2}$  which is an expected pad radius. It is recommended [75] to use  $R^2$  for the optimal circular fit, therefore the mean squared error function acquires the form:

$$S(X_{P0}, Y_{P0}) = \sum_i^{\text{events}} \left[ (x_i - X_{P0})^2 + (y_i - Y_{P0})^2 - r_i^2 \right]^2 \quad (5.4)$$

where  $r_i$  is the center of the triggered ring. It's minimization with respect to parameters  $X_{P0}$  and  $Y_{P0}$  leads to a system of equations:

$$\frac{\delta S(X_{P0}, Y_{P0})}{\delta X_{P0}} = 0; \quad \frac{\delta S(X_{P0}, Y_{P0})}{\delta Y_{P0}} = 0; \quad (5.5), (5.6)$$

which contain the third power of  $X_{P0}$ ,  $Y_{P0}$ . Linearization is done by Taylor series representation of  $R^2(X_{P0}, Y_{P0})$  at point  $(X_0, Y_0) = (0, 0)$  of the reference coordinate system, where  $X_{P0} = X_0 + \Delta X$  and  $Y_{P0} = Y_0 + \Delta Y$ :

$$R^2(X_{P0}, Y_{P0}) \approx R^2(X_0, Y_0) + \Delta X \left. \frac{\delta R^2}{\delta \Delta X} \right|_{(X_0, Y_0)} + \Delta Y \left. \frac{\delta R^2}{\delta \Delta Y} \right|_{(X_0, Y_0)} \quad (5.7)$$

$$R^2(\Delta X, \Delta Y) = x_i^2 + y_i^2 - 2x_i\Delta X - 2y_i\Delta Y \quad (5.8)$$

$$S(\Delta X, \Delta Y) = \sum_i^{events} \left[ (x_i^2 + y_i^2 - r_i^2) - 2x_i\Delta X - 2y_i\Delta Y \right]^2 \quad (5.9)$$

$$\frac{\delta S}{\delta \Delta X} = 2 \sum_i^{events} \left[ (x_i^2 + y_i^2 - r_i^2) - 2x_i\Delta X - 2y_i\Delta Y \right] (-x_i) \quad (5.10)$$

$$\frac{\delta S}{\delta \Delta Y} = 2 \sum_i^{events} \left[ (x_i^2 + y_i^2 - r_i^2) - 2x_i\Delta X - 2y_i\Delta Y \right] (-y_i) \quad (5.11)$$

The resulting equations:

$$2A\Delta X + 2B\Delta Y - C = 0, \quad 2B\Delta X + 2D\Delta Y - E = 0 \quad (5.12)$$

$$\text{where } A = \sum_i^{events} x_i^2, \quad B = \sum_i^{events} x_i y_i, \quad D = \sum_i^{events} y_i^2, \quad (5.13), (5.14), (5.15)$$

$$C = \sum_i^{events} x_i(x_i^2 + y_i^2 - r_i^2), \quad E = \sum_i^{events} y_i(x_i^2 + y_i^2 - r_i^2), \quad (5.16), (5.17)$$

$$\Delta X = \frac{CD - BE}{2(AD - BB)}, \quad \Delta Y = \frac{E - 2B\Delta X}{2D} \quad (5.18), (5.19)$$

The solution for  $\Delta X = -6.2 \pm 0.6$  mm and  $\Delta Y = -15.5 \pm 1.6$  mm was found, where the error estimation is taken from the reference article for  $45^\circ$  arc and 10 cm measured radius with a sufficient number of data points. The method has been proven on simulated events in same BST Pad geometry. An alternative alignment for the pad detectors could be done with the BST Strip system [76] that requires knowledge about positioning of silicon strip and pad sensors with respect to each other in the 3D space.

### 5.1.4 Efficiency Measurement

Results of the threshold scan and efficiency calculations are given in fig. 5.4. Fig. 5.4-a. represents the trigger efficiency of the first BST-Pad plane as a function of the threshold voltages common to all detectors. In this figure every point is an average value over the whole range of  $\theta$  and  $\phi$  available in the experiment. The plateau region for those pad modules extends down to  $-130$  mV in good agreement with the beam calibration results.

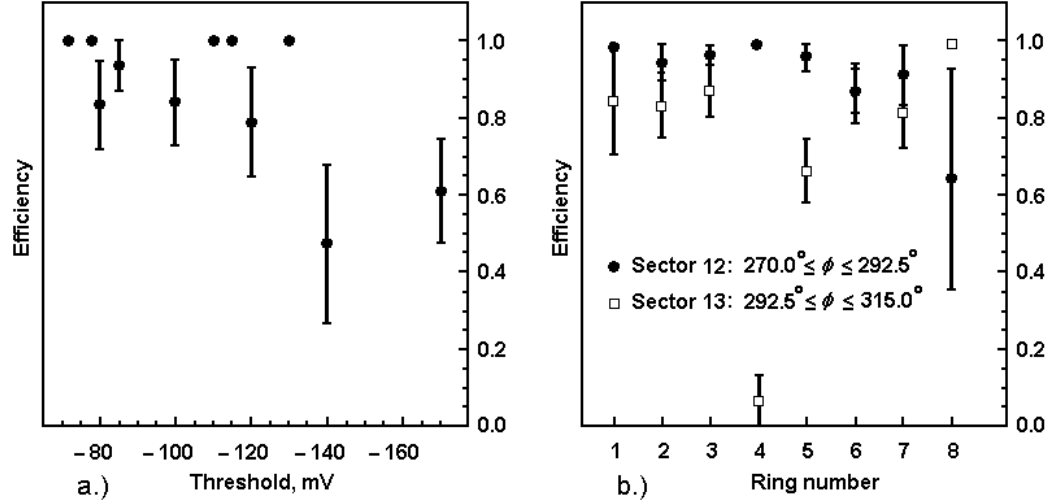


Figure 5.4: Trigger efficiency of pad detectors with one hit requirement a.), ring dependent efficiencies for individual detector modules b.).

Differential efficiencies for each detector module are shown in fig. 5.4-b. For considering the radial subdivision of the silicon sensor the data for different thresholds from the plateau region was unified because of the lack of event statistics for individual rings. This helps to reveal problematic channels, for example the 4-th ring of the module 17 (sector 13). Excluding them from the analysis, the single plane efficiency  $\varepsilon_S$  over the whole area of two detectors is found to be  $\varepsilon_S = (90 \pm 2) \%$ . As the beam calibration shows, most of the detectors have similar performance, therefore in configuration with 4 planes the total trigger efficiency with 3 hits requirement can be estimated as:

$$\varepsilon_T = \varepsilon_S^4 + 4 \cdot \varepsilon_S^3(1 - \varepsilon_S) = (95 \pm 2)\% \quad (5.20)$$

Only statistical errors for the binomial distribution are considered. The geometrical uncertainties: the error on the vertex reconstruction (it results in  $|\Delta_{x,y}| \leq 5$  mm), the alignment imprecision ( $|\Delta_{x,y}| \leq 2$  mm) and the coordinate resolution of the SPACAL ( $|\Delta_{x,y}| \leq 2$  mm) give rise to the systematic

error of the efficiency measurement. These factors are uncorrelated, therefore their sum in quadrature estimates their common effect that leads to a silicon sensor aperture smearing and causes the increase or decrease of the number of accepted tracks. In practice this was included in safety margins and two scenarios, the "good" (to accept) and the "bad" (to reject) have been considered for every track candidate from which no systematic shift was observed for the trigger efficiency.

Beam background and electronics noise are further sources of systematic errors. Their cumulative effect increases the probability of random hits especially at low threshold voltages. In order to minimize their influence on the efficiency result, all tracks are validated in the pad detector in a narrow corridor (within one pad size) around  $(x_B, y_B)$  space point. Because of the 8-fold ring subdivision of each silicon sensor, this removes 7/8 of all pad signals which are not related to real tracks. Residual counts were measured with the same statistics for positrons identified out of BST-Pad acceptance. The fraction of those events is about 0.3 % which can be omitted.



## 5.2 Raw Data Analysis

For the Pad efficiency measurements a reliable track definition required the SPACAL energy above 20 GeV. This excludes the low energies of scattered electrons which are important for the  $F_L$  measurements. The new solution is based on the stand-alone track reconstruction in two or three layers of the BST-Pad, therefore the raw data from several detector planes has been analyzed.

### 5.2.1 Data Readout

The H1 CDAQ requires the BST trigger as a master to launch the data readout in the so-called "dedicated" run. In the absence of the "store card", see chapter 3.5, the only possibility for the pad system was to run in the slave mode, to deliver the raw data during the H1 sampling phase and to keep the information in the PQZP.

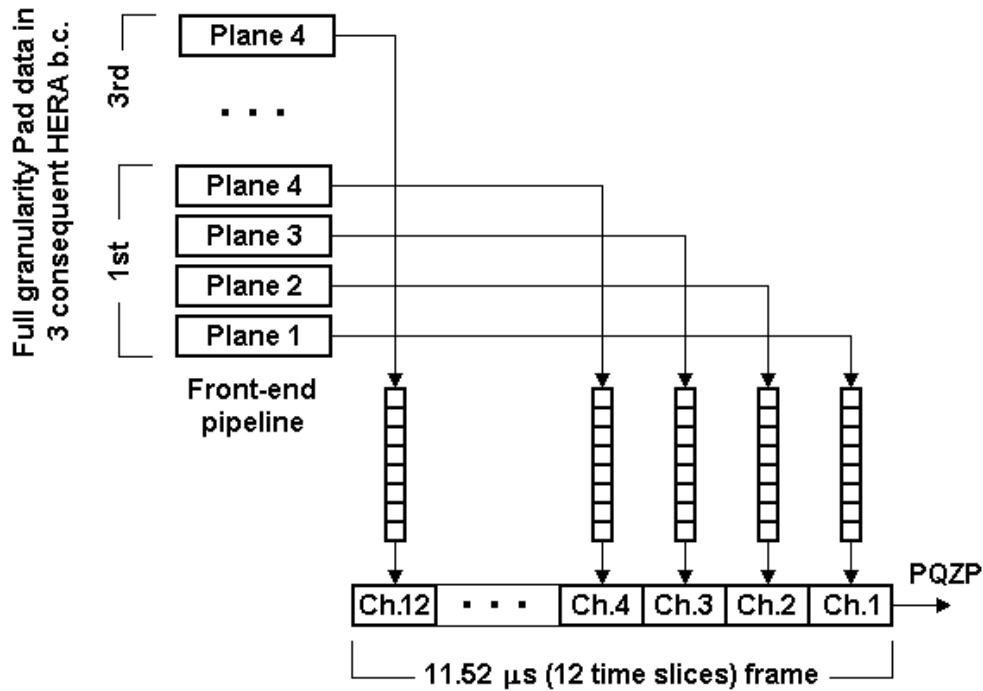


Figure 5.5: BST-Pad data frame in the time-division multiplexing scheme.

The so-called "time-division multiplexing" algorithm is utilised for the raw data transmission. The front-end latches into registers the full granularity pad data for several consequent bunch crossings. The whole set of data is split

onto several clusters allocated to different time slices and then every cluster takes a turn to use the output port, fig. 5.5. Two synchronous counters were implemented, one for the transmitter and another for the receiver, to identify clusters in the data stream. The period of these counters ("frame") depends, besides the readout bandwidth, on the amount of data to be sent out. Thus it determines the system deadtime. The frame position in the PQZP memory is random with respect to the H1 trigger, therefore the memory depth in terms of time slices was chosen longer than the frame length. To prevent broken messages (it happens when the "L1 Keep" signal occurs and makes the PQZP system inactive), every frame is sent out twice increasing further the deadtime. When a broken readout occurs the tail of the previous message is used in the offline analysis to recover the data.

### 5.2.2 Data Treatment

The raw data was taken for all four planes of the same two  $\phi$ -sectors ( $270.0^\circ..292.5^\circ$  and  $292.5^\circ..315.0^\circ$ ) during the luminosity running period of HERA from 10.11.02 till 26.11.02., but only one luminosity fill on 10.11.02 has been considered in the current analysis with the run numbers: **330396-330398, 330414, 330416, 330418, 330419, 330533, 330536, 330537, 330539, 330540** resulting in about 300.000 L4-built events.

The complete BST-Pad information for the latched bunch crossings was reconstructed relying on the counter values. The choice of those colliding bunches independent of the H1 trigger (random) allowed to scan the history through the whole pipeline and to study the distribution of the trigger pulses in time. Again, the pad signals (now already from all 8 detector modules) are met mostly in a single interval which is number 21 propagated backwards from the "L1 Keep" moment with negligible counts in the neighbouring time slices.

The functionality of the pad detectors was checked plotting the occurrence of signals for individual rings of the silicon sensors. Fig. 5.6. shows that detector 3 had to be turned off and that the first ring of the first detector was inefficient.

Rings at smaller radii contain more hits because they are situated close to the beam. The frequency rise is observed for the outermost rings because their larger area starts to play a role. So far there were no "hot" pads discovered. It is proposed to implement such a histogram already at the L4 trigger level for the online control of the BST trigger system.

The number of BST-Pad layers triggered simultaneously, and the hit multiplicity per one sector per bunch crossing are plotted in fig. 5.7 a.) and b.) respectively. Signals in 3 or 4 planes with a reasonably low hit multiplicity

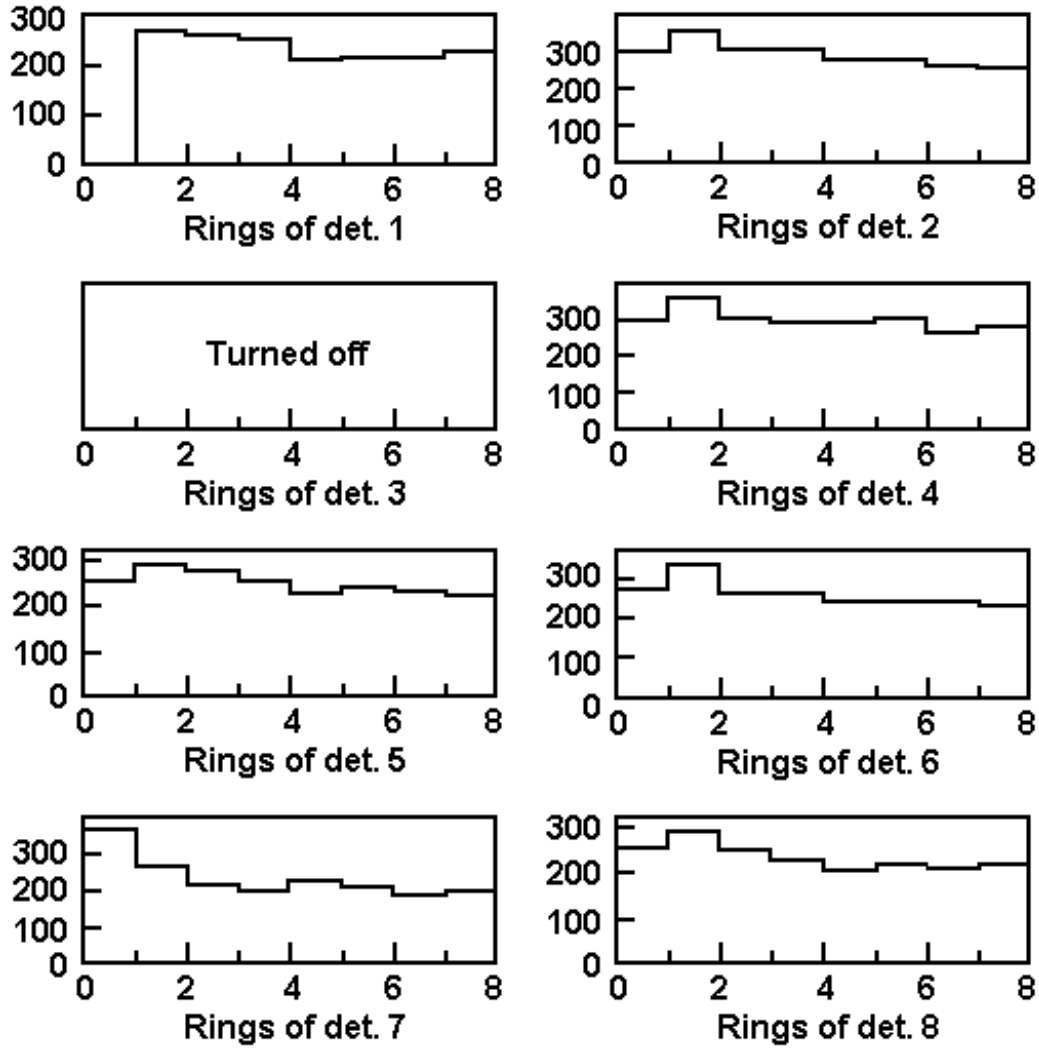


Figure 5.6: Radial distribution of hits in the pad detectors.

per event give the most clear track signatures which are kept in the data file.

For studies of a single plane efficiency the T0-relevant data have been selected. In every sector the track is defined by any two triggered rings in two different  $z$ -positions. Since the ring apertures are rather large and can not be treated as space points to determine the equation for the straight line, a random "ray generator" is being used to find all possible track projections onto the 3-rd and the 4-th planes. Only pointing to the interaction vertex rays have been considered and the so-called "internal" efficiencies for all planes are calculated. With a common to all detector modules threshold of -140 mV an average efficiency of 70% was measured which agrees with results in 5.1.4.

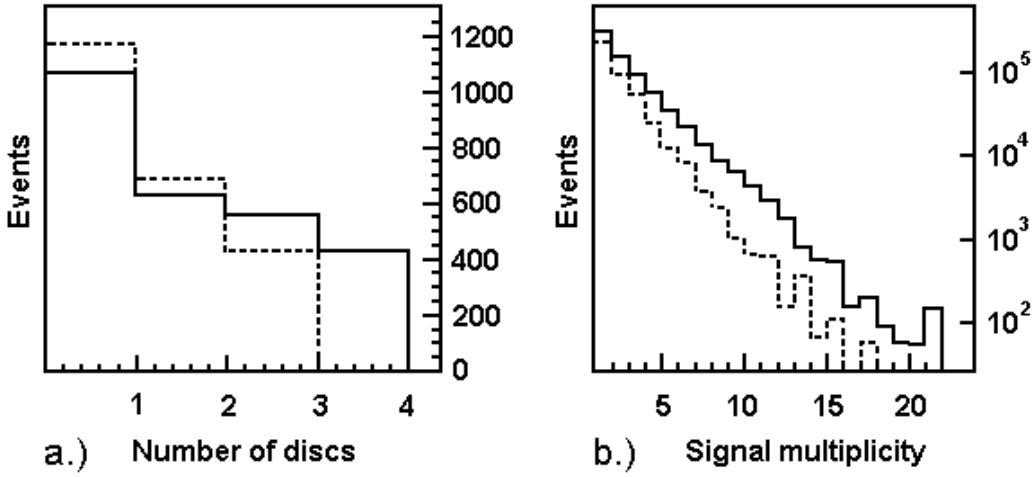


Figure 5.7: The number of Pad-disks triggered simultaneously a.) and hit multiplicities in one  $\phi$ -sector b.) per one HERA bunch crossing. Solid and dashed lines represent sectors 13 and 12 respectively.

The data discrepancy occurs in the process of matching of the tracks to the SPACAL energy clusters. The analysis code has to be more advanced in future and the efficiency has to be studied in more details.

### 5.3 DIS Trigger and Background Suppression

The raw data taking offers a possibility to study the background in H1 seen by the pad detector. The random selection of the bunch crossing to be read out provides an unbiased background estimation. The multiplicity of pads (rings) triggered in one  $\phi$ -sector is shown in fig. 5.8-a. in correlation with the  $z$ -vertex position for each event. One can see, that the multiplicity amounts to 4 or 5 hits for events with the central vertex ( $\pm 30$  cm from the nominal IP), but it is particularly high for events with  $(-200 \leq z \leq -80)$  cm which is a region of two HERA collimators C5a and C5b. The multiplicity cut removes up to 15% of those background events with a threshold of 6 hits per track. This was tested using the luminosity data from the pilot BST-Pad runs for which the full version of the trigger algorithm was loaded into the front-end. Fig. 5.8-b. shows that this background filter provides about 10% suppression power and does not affect any central vertex events.

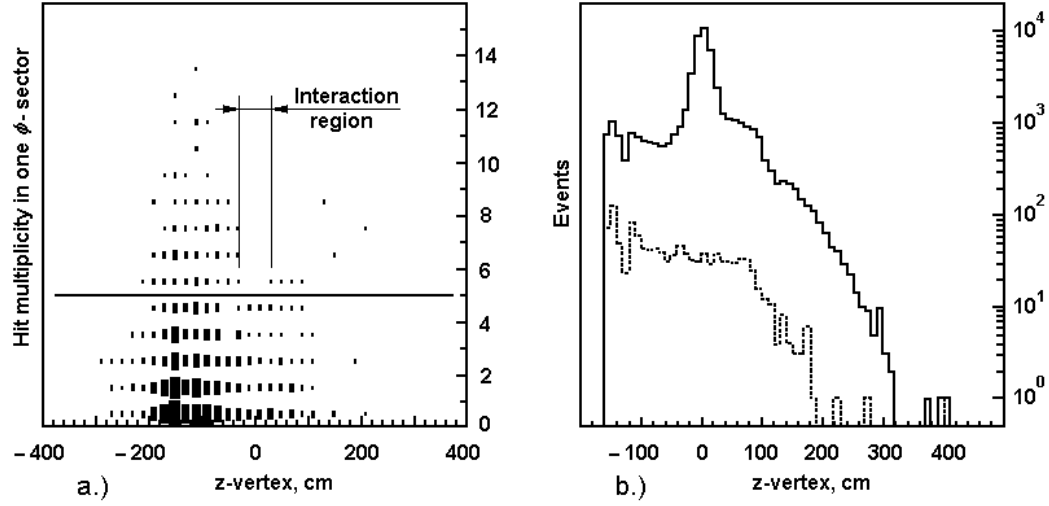


Figure 5.8: Multiplicity of hits in the pad detector versus interaction vertex position as measured in the central trackers a.). Distribution of events along the interaction region (solid line) and the fraction of events rejected by the BST-Pad veto signal (dashed line) b.).

The vertex distribution as measured by central trackers with the prototype low- $Q^2$  DIS trigger *S8* including the Pad detector is shown in fig. 5.9-a. The large level-arm of the BST + SPACAL tandem provides a high selectivity for the vertex tracks.

The L1 subtrigger is based on the lowest SPACAL energy threshold and the track reconstructed with pads:

$$S8 = (TE_{192} \parallel TE_{193}) \& (SPCL_{eJET} > 0) \& v:5 \ f:1 \quad (5.21)$$

The shortcuts  $f : 1$  and  $v : 5$  to the TOF veto signals are given in 2.2.2. The trigger mask set contained combinations for the low-momenta charged particles that made possible the correct energy measurements with the SPACAL, fig. 5.9-b. The run was transparent for the second level trigger therefore an offline L2-filtering was required to match the BST track and the cluster geometry. The energy spectrum obtained with the Pad trigger approaches the one for the DIS - this is the main result of the present work.

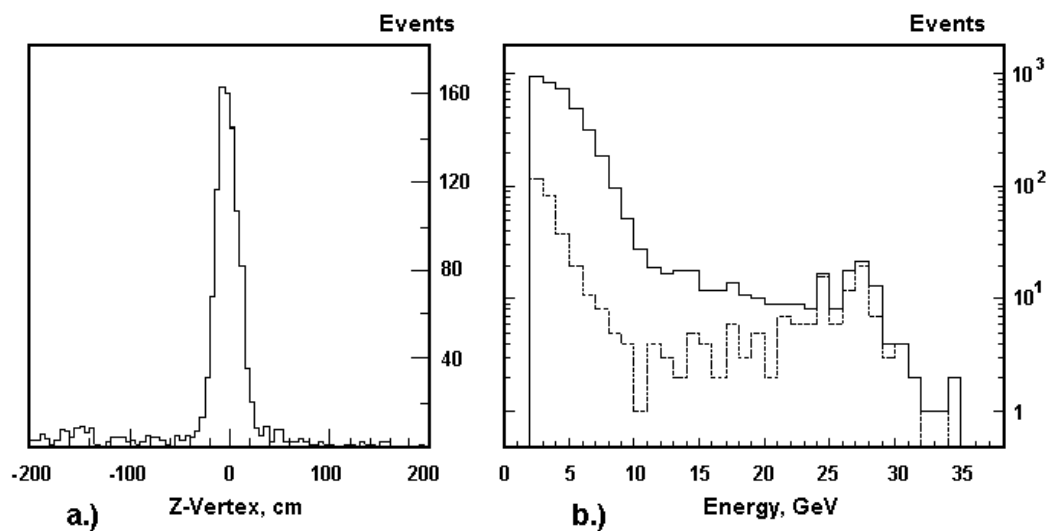


Figure 5.9: Event vertex a.) and the SPACAL energy b.) measured by the H1 apparatus with the pilot S8 trigger. The solid line on the second plot shows all events acquired with the L1 subtrigger and the dashed one - the data passing the offline L2 filtering.

# Chapter 6

## The H1 Radiation Monitor

While the BST pad detector was designed and foreseen to operate as a track trigger, it became clear during 2002 that it can serve as a very much desired tool to monitor backgrounds from HERA which were extremely high and no reliable data taking was possible prior to the spring shutdown in 2003. This chapter describes therefore the further development of the BST-Pad as the main H1 radiation monitor.

### 6.1 Radiation Sources in the Experiment

There are two main sources of the high beam-induced radiation inside the H1 detector: a.) the synchrotron radiation and b.) proton beam initiated collisions with the rest gas molecules in the beam pipe or with the beam optics elements themselves. During the operation of HERA after the luminosity upgrade the majority of the synchrotron radiation entering the H1 detector is backscattered off absorbers which are situated in the right region of H1 from the interaction point at -11 and -18 m [77]. In addition to synchrotron radiation background, off-momentum leptons which have lost some fraction of their energy due to beam gas interactions upstream ( $+z$ ) of the detector are bent by the dipole magnet into the beam pipe, leading to another source of  $\bar{e}$  related background.

The most significant background component observed in the H1 detector arises from proton beam-gas interactions. A simple model which describes the sensitivity of the background rates, measured in the CJC and the BST pad detector, to the HERA beam currents and to the quality of the vacuum at various points along the beam line has been developed [78]. During luminosity running, the rate is seen to depend on both beam currents,  $I_{\bar{e}}$  and  $I_P$ , and four contributions can be distinguished:

1. A small pedestal rate  $R_0$ , determined in off-beam periods which is constant in time and independent of the beam conditions;

2. A contribution from synchrotron radiation,  $\alpha_{SR}I_{\bar{e}}$ , proportional to the positron current;
3. A contribution from positron beam-gas interactions,  $\alpha_{\bar{e}}I_{\bar{e}}\langle P_L \rangle$ , proportional to the positron beam current and the average pressure to the left of the IP;
4. A contribution from proton beam-gas interactions,  $\alpha_P I_P \langle P_R \rangle$ , proportional to the proton beam current and the average pressure to the right of the IP.

The synchrotron radiation power and higher order mode excitations lead to heating effects in the beampipe and the average pressure in HERA is supposed to depend linearly on the positron beam current. Assuming that  $\langle P_L \rangle = P_0^L + \gamma_L I_{\bar{e}}$  and  $\langle P_R \rangle = P_0^R + \gamma_R I_{\bar{e}}$ , with  $P_0$  representing the base pressure, the total background rate  $R_{BG}$  can be parametrized as follows:

$$R_{BG} = R_0 + \tilde{\alpha}I_{\bar{e}} + \alpha_{\bar{e}}\gamma_L I_{\bar{e}}^2 + \alpha_P I_P (P_0^R + \gamma_R I_{\bar{e}}) \quad (6.1)$$

where  $\tilde{\alpha} = \alpha_{SR} + \alpha_{\bar{e}}P_0^L$  combines the contribution from synchrotron radiation and from positron beam-gas at the base pressure. It is possible to derive values of  $\tilde{\alpha}$  and  $\alpha_{\bar{e}}\gamma_L$  from the positron only fills, while the coefficients  $\alpha_P P_0^R$  and  $\alpha_P \gamma_R$  could be determined during luminosity operation. The distinction of these terms allows then to identify the relative importance of the different background mechanisms.

## 6.2 Radiation Effects in the BST

### 6.2.1 Silicon Sensors

Radiation damage of the semiconductor structure occurs through two basic mechanisms:

1. Bulk damage due to displacement of atoms from their lattice sites. This leads to changes in doping concentration with a corresponding resistivity decrease, necessity of higher depletion voltage and increased leakage current. Displacement damage depends on the particle type and energy.
2. Surface damage due to charge build-up in the silicon oxide passivation layer and the creation of defects at the  $\text{SiO}_2$  - Si interface. Both are induced by ionizing particles and lead to surface leakage currents increase and a signal-to-noise level degrading. This effect depends strongly on the sensor fabrication technology.



Measurements held in H1 for the silicon detectors of the PLUG calorimeter which were exposed to high radiation doses showed that the damage to the bulk of the silicon can be excluded [79]. Large surface damages observed were inconsistent with those doses seen by the dosimeter, therefore the main component of the background causing radiation effects can be attributed to photons with energies below 30 keV to which the dosimeter was insensitive. Low energy photons (up to 50 keV) should be entirely stopped in a few millimeter thick Beryllium beampipe [80] of the HERA-II design.

## 6.2.2 Readout Electronics

Radiation effects on electronics can be divided into 3 different categories according to their effects on the semiconductor components:

1. Single event effects are related to individual interactions in the silicon. Highly ionizing particles can directly deposit enough charge locally in the silicon to disturb the function of electronic circuits:
  - Single event upset (SEU): The deposited charge is sufficient to flip the value of an analog or logical signals, memory bit, etc.
  - Single event latch-up (SEL) results in a short circuit between the power supply and the ground. It can be triggered by a locally deposited charge into the CMOS technology bulk. The permanent damage that can't be recovered after the power reset is classified as a single event burnout (SEB).
2. Hadrons may displace atoms in the silicon lattice of active devices (displacement damage) and thereby affect their function. Bipolar and especially optical devices: LEDs and opto-couplers are very sensitive to this effect.
3. Total ionizing dose (TID) causes the threshold voltage of MOS transistors to change because of trapped charges in the silicon dioxide gate insulator. Modern sub-micron technologies tend to be more resistant to total dose effects, because these trapped charges can potentially "escape" by tunneling effects. High performance analog devices (e.g. amplifiers, ADC, DAC) may potentially be affected at quite low doses of a few hundred Rad.

Redundancy design is needed for SEU corrections because this is a statistical process which depends mainly on the dose rate. Most experts agree that TID related problems are rarely seen for digital circuits below a few kRad. Displacement damages can be estimated or approved with some safety factors:

Simulation uncertainty:	Factor 2
Radiation qualification uncertainty:	Factor 2
Component to component variation:	Factor 2

The minimum total safety factor of 8 can be reduced if the radiation qualification is justified with a precise monitoring of the radiation levels.

### 6.3 Radiation Monitoring with Pads

In view of the large background problems at HERA-II, the BST-Pad system was configured to measure the radiation background inside the H1 facility. The BST-Pad is the trigger detector closest to the interaction point, which suffers also the high radiation damage from upstream showers. The detector has good sensitivity to the particle background and reduced sensitivity to the synchrotron radiation. The exposure rate is proportional to the hit multiplicity  $N$  per detector area  $S$  per one HERA bunch crossing  $T$  and expressed as dose  $D$  over time  $t$ :

$$R = \frac{D [Gy]}{t [s]}, \quad D = \frac{E [J]}{m [kg]}, \quad m = \rho V \quad (6.2), (6.3), (6.4)$$

The dose is determined by the energy deposition in the volume  $V$  of density  $\rho$ . Relativistic muons, pions and protons suffer a collision energy loss when passing through matter. In a thin silicon layer their stopping power amounts to (18..25) keV per 100  $\mu\text{m}$  and doesn't depend on their initial energies as they are minimum ionizing particles.

For relativistic electrons and positrons the radiation (bremsstrahlung) contributes substantially to the stopping power when their energies are much above the critical value of a few MeV. It leads to electron-photons showers, but in a thin crystal this chain doesn't develop because of a very small interaction probability for  $\gamma$ -quanta. Thus electrons may be also treated as MIPs. Some fraction of the energy destructing the crystal, so-called "kerma", is carried by ionizing charged particles liberated by neutral ones [81].

$$E = N \cdot \varepsilon \cdot \rho x, \quad \varepsilon = \frac{\delta E}{\rho \delta x} \approx 2 \text{ MeV cm}^2/\text{g} \quad (6.5)$$

Substituting (6.3), (6.4) and (6.5) into (6.2)

$$R = \frac{1}{S} \cdot \frac{N}{T} \cdot \varepsilon, \quad f [Hz] = \frac{N [hits]}{T [s]} = \frac{S R}{\varepsilon} \quad (6.6), (6.7)$$

The silicon sensors have an area of  $S \approx 20 \text{ cm}^2$ . The dose rate of 100 Gy per year mentioned in 3.7 would correspond then to an equivalent frequency

$f \sim 400$  kHz which is calculated online as a number of pads triggered within one second. In every  $\phi$ -sector a number of hits is accumulated and transmitted to the master card as short packages of pulses – the principle of the pulse number modulation (PNM). On the master card these pulses are counted for one second, the maximum count rate among 12 sectors is found and during the next second the integrated result is sent to the H1 CDAQ for the data logging and visualization while the new result is being prepared. Finally, the dose rate is represented as a number of pulses which are derived from the HERA clock frequency – the principle of the frequency modulation (FM). The H1 central trigger is measuring this modulated frequency which value is shown online in the H1 and HERA control rooms. It can be also seen on any remote computer under the Java applet:

<http://h1lumiserver.desy.de:8080/main/h1mon.html>

In fig. 6.1 the correlations between the BST-Pad count rate and the beam currents are demonstrated as they look like on the display. In Fig. 6.2 the BST-Pad frequency is compared to the background rate measurements by scintillation counters close to the beam pipe.

In contrary to the PNM algorithm, the frequency modulation provides an equidistant position for signals and a quasi-constant load for the CDAQ counter and, hence, a smooth curve on the display. The core part of the VHDL code for the radiation monitor with some necessary comments to the algorithm is given in appendix C.

The idea to deliver the maximum frequency may cause a so-called "hot spot" effect when a couple of detectors give enormous high rate. This, nevertheless, is still better than the average value because the synchrotron background has a strong  $\phi$ -dependence, and the intensity of the scattered radiation varies with "1/distance" law. Thus a high radiation load must be indicated for every detector module to avoid its fast ageing. Another advantage of a small normal area for the radiation monitor is a weak count rate dependence on the number of detectors in use. It allows to perform different tests for the trigger algorithm without affecting the monitoring rate.

A threshold choice for the radiation monitor provides a negligible  $R_0$  term in formula (6.1). An attempt to put a real MIP threshold led up to a five-fold total rate increase depending on background conditions. It means that 100 Gy/year limit would correspond then to 80 kHz count rate measured with the chosen noise-free settings. Running at the level of 80 kHz one should keep in mind that the real rate is higher and no more room for safety is left. The need of lower thresholds for the trigger operation requires the dynamic pedestal subtraction for the count rate which was realised for up to 25 kHz noise frequency.

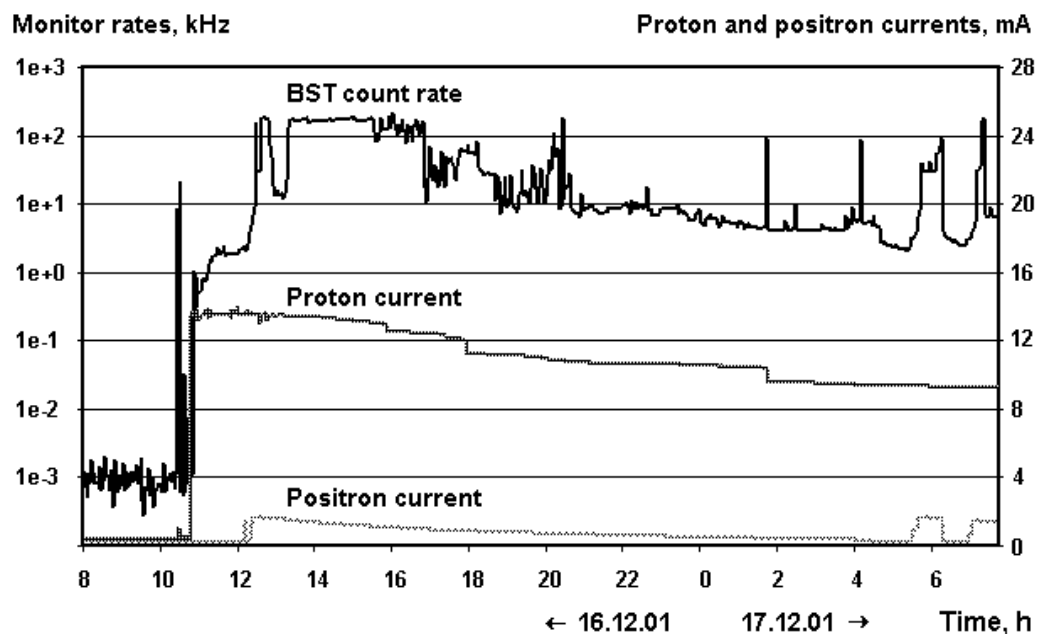


Figure 6.1: Radiation monitor frequency as a function of beam currents.

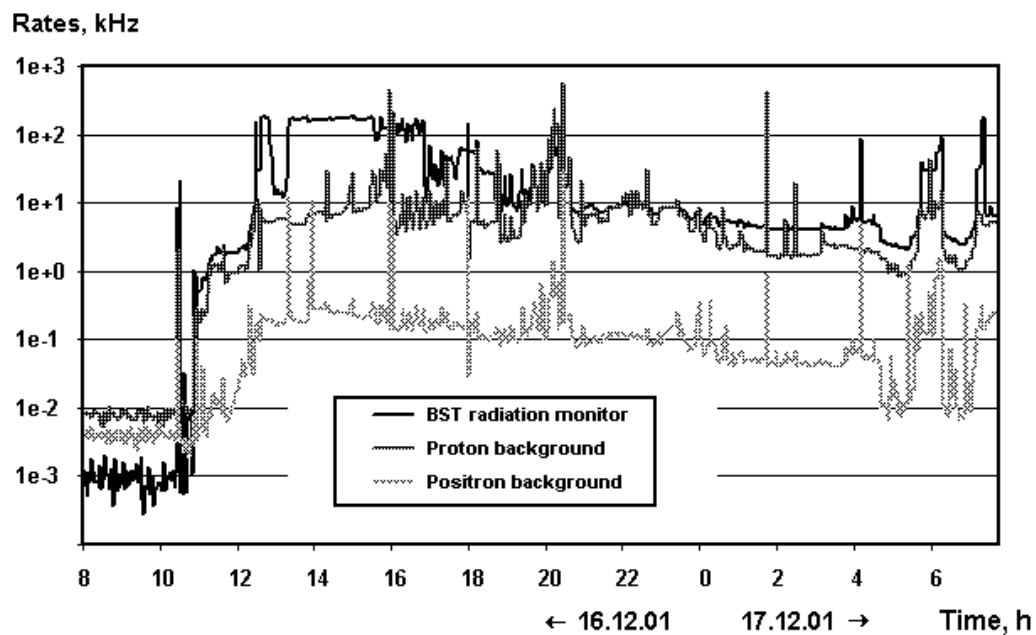


Figure 6.2: Correlations between the radiation monitor frequency and the lepton and the proton background rates as measured with the scintillation counters close to the beam pipe.

## 6.4 Further Applications for the BST-Pad

A number of further useful tasks were solved with the pad detectors during HERA machine studies and during luminosity running:

**HERA vacuum studies in the H1 region:** The radiation monitor is being used for indirect measurements of the rest-gas pressure in the vicinity of the H1 detector, fig. 6.3-a. The rate increase may indicate the vacuum worsening on the formula (6.1).

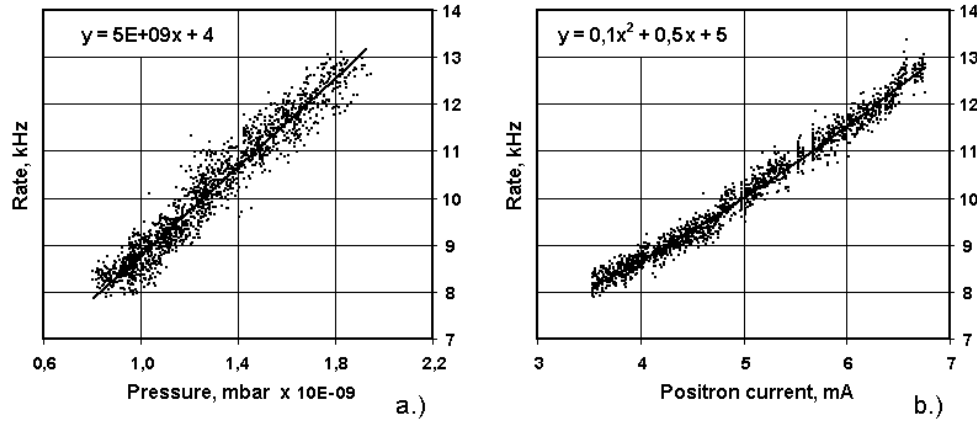


Figure 6.3: Linear a.) and quadratic b.) terms of the radiation monitor rate.

**Control of background conditions:** A clear correlation between the CJC current due to random background hits and the count rate from the silicon pad detectors was observed, fig. 6.4. Trips of the CJC high voltage power supply occur very often when the radiation monitor rate exceeds 50 kHz.

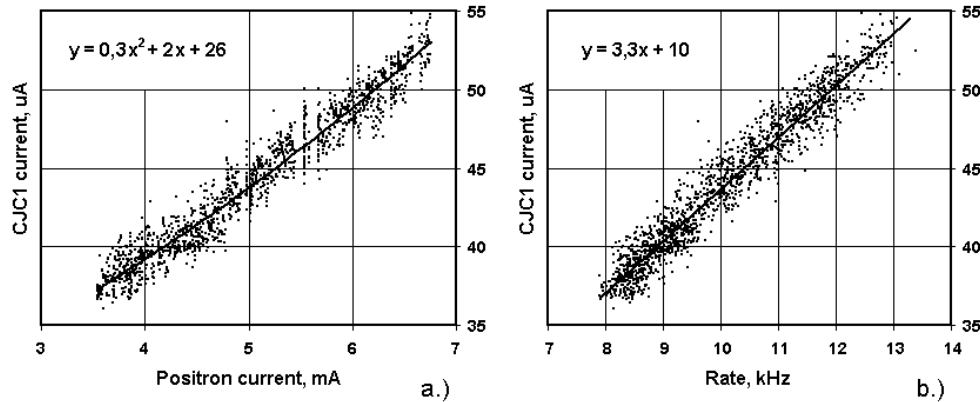


Figure 6.4: A similar to the radiation monitor behaviour of the CJC current.

During injection this rate is usually high, but after the luminosity announcement it get used to optimize background conditions for H1 (collimators positioning, beam focusing, etc.) by help of the BST-Pad before the central and the forward chambers are turned on. In some cases, when the situation is not getting better, the H1 shift crew may insist on a beam dump and a new fill.

**Cumulative dose:** Vital parameters of all HERA experiments are stored in a so-called "HERA archive" data base. It includes also the history of the H1 radiation monitor rate. Thus it is possible to calculate the total dose absorbed by the silicon, fig. 6.5. This result might potentially be affected by a "hot-spot" – non-uniform radiation field conditions [82].

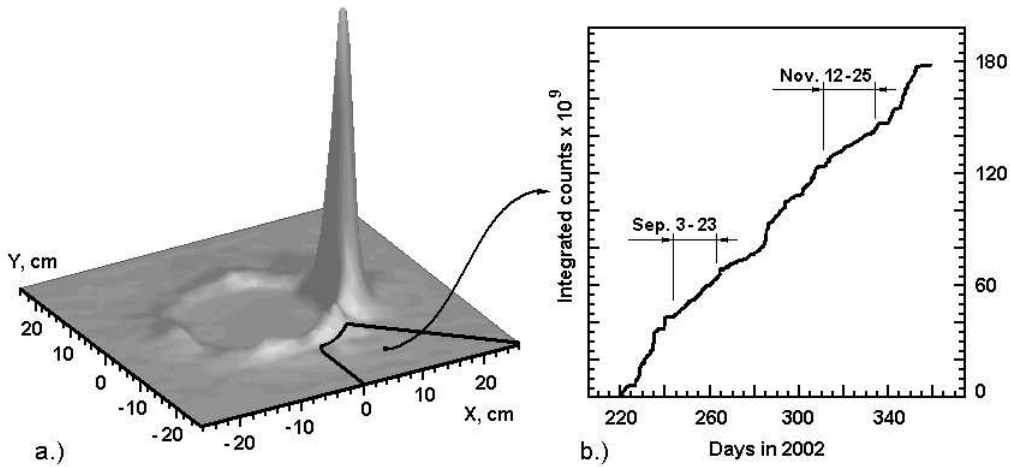


Figure 6.5: a.) The particle occupancy of the electromagnetic SPACAL during the HERA luminosity run. The marked region in the SPACAL XY-plane corresponds to the radiation monitor coverage area. b.) A monthly dose of about 100 rad<sup>1</sup> was observed for this sector of the silicon pad detector in autumn 2002, calculated from the two periods indicated.

**Beam dump watchdog:** There was a proposal made to use the radiation monitor in correlation with the veto wall or some other sensitive sub-detectors for the automatic beam shut-down. The system which would trigger the decision to dump the beam should be tolerable to spikes or to occasional rate increase within a few minutes. By now just a sound alarm is generated for the shift crew when the background is too high.

<sup>1</sup>Measured with a high ( $\approx 1.5$  MIP) threshold. The real dose may result in 500 rad/month that gives nearly 100 Gy/year which was specified.

## 6.5 Design Outlook

Electronics design must cope with radiation levels over full lifetime with sufficient safety factors. In addition to the radiation monitoring, a special technical service is necessary for different parts of the sub-detector functioning in radiation conditions:

- Analog circuitry requires a regular threshold scan with a calibration pulse to check the gain and(or) the comparator threshold change of the readout chip.
- Loss of data from a few detector channels can be accepted, but no effects on general trigger signals should occur. If it is the case, then parts of the system should be reprogrammed to borrow these trigger bits from the less important channels.
- Soft failures must be resolved by the front-end re-initializing and the reset procedure should be reasonable fast. Configuration data must be regularly updated to prevent its corruption in the memory due to single event upsets.

These works have to be done independently of the ongoing function of the pad system, but the detector multitasking makes it difficult to keep all parallel sub-processes unaffected. It makes the device maintenance slower and as experience shows, any kind of additional functionality must be realized leaving the detector for its primary physics goal untouched, if possible.

# Chapter 7

## Summary

Changes made to the H1 detector during the HERA upgrade in 2001 are briefly described in this thesis. The first level trigger of H1 includes now 5 new trigger elements from the silicon pad detector which was developed with this thesis to improve measurements of the Deep Inelastic Scattering at low  $Q^2$  and low  $x$  for studies of the proton structure functions.

The most accurate measurement of  $F_L$  and  $F_2$  in the acceptance region of the Backward Silicon Tracker of H1 has been the main motivation for the trigger device to reduce background and identify DIS where the scattered lepton only defines the interaction vertex in the H1 detector.

Because of the limited bandwidth of the H1 CDAQ the BST trigger becomes especially important to keep the rate of the DIS event candidates at a level acceptable for the H1 central trigger as it increases significantly with higher HERA-II luminosity.

The BSTT is the fastest detector of H1. It complies with the "dead time-less" triggering concept and it needs only 4 HERA clock periods to deliver the track information to the H1 central trigger system. The reprogrammable front-end makes it suitable for some other applications like the H1 radiation monitor which was an essential tool during HERA machine studies.

The detector development did cover both the electronics design and the computer engineering. That included the hybrid design, the complete measurement of parameters of the PRO/A readout chip and evaluation of the best ASICs, development of the new front-end (motherboard) including firmware for the slow detector control and for the trigger data reduction. The power supply system for the front-end was design and also several VME modules interfacing the BSTT to the H1. First operation of the BST Pad system in the high radiation environment during HERA-II startup provided valu-



able experience in detector design. For more reliability of the mixed analog and digital system, some circuitry redundancy and more careful selection of electronical components are required.

For the BST detector upgrade more effort was invested into software development. Therefore skills in the VHDL programming were mastered for microcontrollers and the local DAQ architectures.

Three beam tests were performed which revealed an important understanding of properties of the silicon detectors, for instance the common mode effect. A short detector design summary and test results were published in [43].

Luminosity data were taken with the BST pad detector in H1 and trigger efficiencies of individual detector modules have been measured. Predictions for the total efficiency of the track trigger result in  $(95 \pm 2) \%$ , but it has to be studied in more detail especially at low energies of the scattered electrons (positrons). Further data analysis, in particular studies of the beam-induced background in H1, opens a possibility to veto those non-physical events already at the first trigger level.

A comprehensive overview of the BST Pad system is given in this Ph.D. thesis. Some intermediate results were also presented on the "DPG-2000" and "DPG-2002" conferences, on the international workshop on the vertex detectors "Vertex-2001" and on the seminar in the Humboldt University zu Berlin in January 2002.

# Acknowledgments

I am deeply grateful to Dr. Max Klein who let me realize myself.

I want to thank Dr. Ulrich Gensch for the cordial invitation to DESY Zeuthen and for the official support of my stay in Germany which was, unfortunately, too short because it was too good.

I am much obliged to all my friends and dear colleagues:

Peter Kostka and Thomas Naumann for their invaluable help in my PhD; Hans Henschel, Wolfgang Lange, Joachim Meißner, Ulrich Harder, Milan Janata and all bearded men of whom I truly enjoyed working with; Sergey Gorbunov for our fruitful discussions, Mikhail Kalmykov, Maxim Lukyanov and Anatoli Astvatsatourov for our social events; my "Brothers in Arms" Tomáš Laštovička, Vladimir Arkadov, Miroslav Nožička, Alexey Petrukhin and Doris Eckstein for their every day support; Jan Kretzschmar, Dirk Hoffmann and Nick Malden just because.

**Danke Deutschland !**



Figure: the whole "treasure" of Max

# Appendix A

## Subsystems of the BST-Pad

### A.1 Slow Control Subsystem

The slow control subsystem of the BST-Pad, fig. A.1, controls the operating regimes for the silicon pad detectors. That includes:

1. Fast re-initialization of the front-end to recover from radiation effects;
2. Downloading and reading out sequencer codes for the PRO/A ASICs;
3. Setting and reading back thresholds for the pad hybrids;
4. Power supply operation and monitoring;
5. Temperature measurements.

The last two processes run regularly with a characteristic time interval of several seconds. Any other tasks are performed only once before the detector operation, therefore a default "power on" configuration has been implemented for them. The control functions are distributed between the front-end boards and an unique VME interface card, the so-called "power-and download-station" (PDS).

#### A.1.1 PDS Control Functions

The functionality of the PDS module is defined by four control registers. Writing data in one of those registers forces, therefore, the commands to be automatically executed by the PDS, see table A.1. The actual register contents and the system response can be read out via the VME interface. This VME bus is controlled by a MacVEE V370 which is connected to a Macintosh PC (current IP: 131.169.33.234).

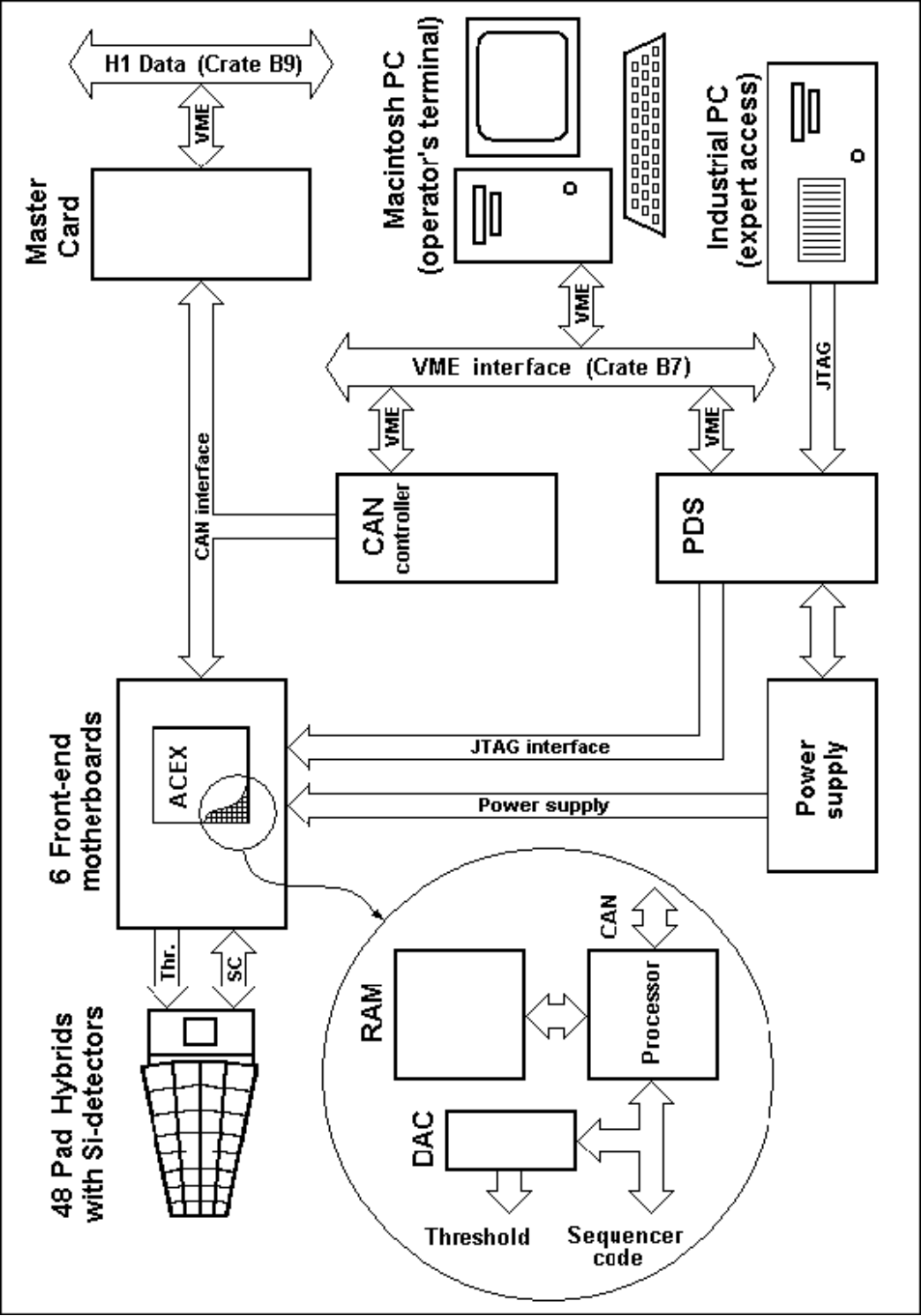


Figure A.1: Block diagram of the BST-Pad slow control system.

The full register address consists of 8 hexadecimal digits. The first digit (the most significant one) corresponds to a slot number of the interface card in the Macintosh PC. The second is defined by a VME crate number as set on the V370 controller. The remaining six positions are related to the PDS module itself. The upper two digits are preselected by hardware switches on the board. The PC, the MacVEE and PDS address area establishes the so-called "base address" of the control register. The current base address is *E266*. The last four hexadecimal digits - the "offset" values, - are given in table A.1. If the PDS board is addressed, but the offset is any other than those specified, a bus error signal will be generated.

Table A.1: PDS slow control functions

Offset	Register	Data Bits	Write	Read	Description
0000	1	15...0	Yes	Yes	Identifier word
0002	2	10...8	Yes	Yes	JTAG multiplexer
0002	2	5...0	Yes	Yes	Front-end reset
0004	3	13...8	No	Yes	Initialization status
0004	3	5...0	No	Yes	"Look at me" status
0006	4	13...8	No	Yes	Low voltage status
0006	4	5...0	Yes	Yes	High voltage control

The **identifier word** in the first control register has a free, user-defined data format to keep track of any changes to the BST-Pad detector settings (version of firmware, sequencer code, threshold values, mask sets, etc.). It is recommended, therefore, to assign same identifiers to the PDS and to the Master card because this word is appended to the H1 data. The default ("power-on") data setting is "0000" (hexadecimal, further "hex").

A **JTAG multiplexer** contained in the PDS is routing the JTAG interface from the industrial PC (current IP: 131.169.133.87) to the front-end board to be programmed. The multiplexer address is selected by three bits: "8", "9" and "10" of the second control register (table A.2) and corresponds to the board number 0...5 (control channel). For any other combination of these bits there is no valid address defined! During changing the JTAG address the other bits of the second register must be protected against overwriting. The default data setting is "000" (binary).

The **front-end reset** of channels 0...5 is performed through bits "0...5" of the second control register. A "1" setting allows the corresponding front-end board to be initialized via the JTAG or from the on-board EPROM while "0" forces the front-end reset. During reset or initialization any other bit of

the second register must be protected against overwriting. The default data setting is "11111" (binary).

The **initialization status** of channels 0...5 is indicated by bits "8...13" of the third control register. A "1" means successful initialization while "0" shows that the front-end circuitry has failed to initialize. These signals are also visualized individually for every channel by front-panel LEDs.

The **"look at me" status** of channels 0...5 is indicated by bits "0...5" of the third control register. A "1" shows that command execution has been completed by the front-end while "0" means that the process is still under way. A logic OR combination of all six LAM signals is indicated by a front-panel LED.

The **low voltage status** of channels 0...5 is indicated by bits "8...13" of the fourth control register. A "1" means that the corresponding power module delivers the supply voltages while "0" denotes that these voltages are off.

The **high voltage control** of channels 0...5 is performed through bits "0...5" of the fourth control register. A "1" setting switches the corresponding depletion voltage on while a "0" turns it off. The default data setting is "00000" (binary).

Table A.2: Channel select for the firmware programming

Bit 10	Bit 9	Bit 8	Front-end board	PDS front-side connector
0	0	0	0	XS1 (main board)
0	0	1	1	XS2 (main board)
0	1	0	2	XS5 (piggyback)
0	1	1	3	XS6 (piggyback)
1	0	0	4	XS7 (piggyback)
1	0	1	5	XS8 (piggyback)

### A.1.2 Front-end Control Functions

A large programmable logics chip (ACEX) houses numerous control functions for the front-end operation. It is configured at power-on from an on-board EEPROM and can be programmed by user through the JTAG interface. The slow control processor, fig. A.2, is based on clocked state machine symbolically called "KGB". The commands to be executed are masked by the control register (CR) bits. The chip features also a bidirectional interface to the CAN controller.

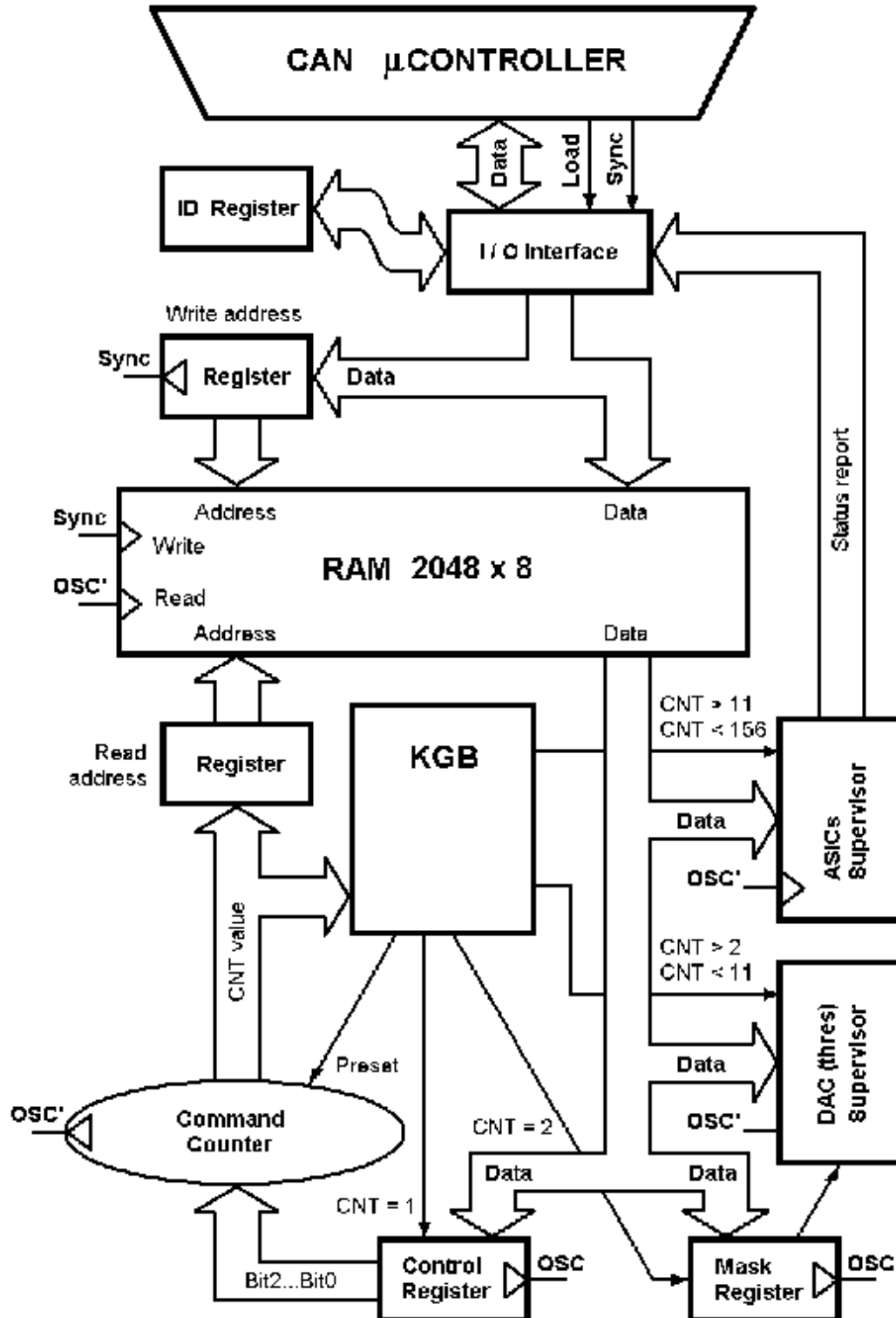


Figure A.2: Architecture of the slow control processor.

## Control Register

All CR bits and their associated commands are listed below:

A **Bit\_0** = "1" forces discriminator thresholds to be set for those hybrids which are specified in the mask register, see table A.3 for details. This bit can be assigned by the user, but it will be overwritten automatically during the "power on" or "power reset" procedures described below. The new value is copied from the corresponding bit in the *0x01* (hex) register. The "look at me" signal going high causes an asynchronous reset for the Bit\_0.

A **Bit\_1** = "1" forces downloading of ASIC sequencer codes. This bit can be assigned by the user, but it will be overwritten automatically during the "power on" or "power reset" procedures described below. The new value is copied from the corresponding bit in the *0x01* (hex) register. The "look at me" signal going high causes an asynchronous reset for the Bit\_1.

A **Bit\_2** = "1" forces reading back of ASIC sequencer codes. This bit can be assigned by the user, but it will be overwritten automatically during the "power on" or "power reset" procedures described below. The new value is copied from the corresponding bit in the *0x01* (hex) register. The "look at me" signal going high causes an asynchronous reset for the Bit\_2.

A **Bit\_3** = "1" forces the analog and digital voltages to shut off. Set by the user this bit will be automatically reset after the beginning of the shutdown procedure.

A **Bit\_4** = "1" forces the data block readout. Set by the user this bit will be automatically reset after the last byte is sent. Pulling "ACX\_APX" to "1" causes an asynchronous reset for the Bit\_4 as well.

A **Bit\_5** = "1" forces writing a block of data. Set by the user this bit will be automatically reset after capturing the last byte. Pulling "Load" or "ACX\_APX" to "1" causes an asynchronous reset for the Bit\_5 as well.

The last two bits: **Bit\_6** and **Bit\_7** select one of the status registers for the readout. For the combination: Bit\_6 = "0", Bit\_7 = "0" ("00" bin) the voltage control register is chosen. The "10" (bin) corresponds to the low byte and "01" (bin) - to the upper byte of the ID word while the "11" (bin) is related to the ASICs download control. These bits can be assigned by the user, but they will be overwritten automatically during the "power on" or "power reset" procedures described below.

**Note:** the memory cell *0x01* (hex), which is a data source for the control register, is protected against overwriting during sending a block of data to the RAM !



## Data Transmission

The CAN micro-controller ( $\mu$ controller) uses three signals: "ACX\_APX", "Load" and "Sync" to supervise the data exchange with the ACEX RAM. "ACX\_APX" is a chip select signal for the ACEX. During any control action it must always be "0". "Load" is controlling the information flow: by setting it to "0" the CAN  $\mu$ controller drives the data and the ACEX is turned in receiver mode while "1" reverses the data flow. "Sync" is used to synchronize the data transmission. Its "high-to-low" transition (further  $\downarrow$ ) latches the address present on the data bus while the "low-to-high" transition ( $\uparrow$ ) latches the data itself. Pulling "Load" or "ACX\_APX" to "1" inhibits the RAM content update.

The RAM capacity amounts to 2048 bytes<sup>1</sup>. It is possible to write the content of any single byte or to download a block of bytes. The data readout is possible in blocks only. The block length is stored at address  $0x7F$  (hex) and protected against overwriting during sending a block of data to the RAM. The maximum length amounts to 255 bytes, the default value is set to zero.

The address of the first byte to be written or read out consists of the base address and the offset stored at  $0x7B$  (hex) and  $0x7C$  (hex), respectively. Both, the base address and the offset are protected against overwriting during sending a block of data to the RAM. The base address ranges from 0 to 7 and the offset from 0 to 255, and their default values are set to zero.

**Writing a block** of data starts immediately after the CR Bit\_5 is set to "1". With the next "Sync"  $\uparrow$  the data present on the data bus will be latched into memory cells starting from the address  $Base\ Address + Offset$ . Every "Sync"  $\downarrow$  will increment the address until it reaches the value  $Base\ Address + Offset + Block\ Length$ .

The **block readout** starts after "Load" going high if the CR Bit\_4 was set to "1" before. Again, the "Sync"  $\downarrow$  increments  $n$  times the output address ( $n = Block\ Length$ ). After the block readout being complete, the register specified by CR Bit\_6 and Bit\_7 can be read out.

## Power Supply Reset

The power for pad hybrids, see chapter 3.4, is switched off for two seconds after setting "Load" if the CR Bit\_3 was set to "1" before. The idea of this procedure is to respond locally to a possible ASIC latch-up without any external power off (the front-end board can be left running). The analog bipolar voltage is turned on again after one second and the digital bipolar voltage

---

<sup>1</sup>All numbers are represented in decimal format, unless otherwise specified.

after two seconds, according to PRO/A specifications. The same switching sequence is provided for the hybrids supply during the global power-on of the front-end.

### Setting up Thresholds

The procedure starts after "Load" went high if CR Bit\_0 was set to "1" before. For each hybrid a corresponding flag in the mask register must be set to "1". This helps to change one or more thresholds while keeping all others unchanged. The threshold voltages  $-1V \leq U_{thres} \leq 0.2V$  are encoded as  $Data = int(213 \cdot (0.2 - U_{thres} [V]))$  to be stored in the memory. Each byte thus contains one individual threshold value for one hybrid.

Table A.3: Structure of the mask register *0x02* (hex)

Flags	Bit_7	Bit_6	Bit_5	Bit_4	Bit_3	Bit_2	Bit_1	Bit_0
Hybrid	_00	_01	_02	_03	_13	_12	_11	_10

The pad hybrids are indexed by their sector number in  $\phi$  (low bit). High digit corresponds to the plane number in  $-z$  direction, i.e. the "hybrid\_12" means one in the odd sector situated in the 2-nd plane.

Example: set -200 mV threshold for the hybrid\_03.

```
Set "Sync" = "1"
Set "Load" = "0"
  Set "Data" = "01" (hex) % Selecting the control register %
Set "Sync" = "0"
  Set "Data" = "01" (hex) % Assigning the control register %
Set "Sync" = "1"
  Set "Data" = "02" (hex) % Selecting the mask register %
Set "Sync" = "0"
  Set "Data" = "10" (hex) % Assigning the mask register %
Set "Sync" = "1"
  Set "Data" = "07" (hex) % Selecting the hybrid_03 %
Set "Sync" = "0"
  Set "Data" = "55" (hex) % Assigning the threshold %
Set "Sync" = "1"
Set "Load" = "1"
```

### Setting up PRO/A ASICs

The procedure starts after "Load" went high if CR Bit\_1 was set to "1" before. All hybrids are loaded in parallel with common data strobe. The ASICs data are stored in eight rows which are aligned in the RAM through addresses 12 (dec) to 83 (dec). Each row contains one sequencer code and the corresponding hybrid is selected by a bit number, see table A.4.

Table A.4: Matching between sequencer codes and RAM bits

Location	Bit_7	Bit_6	Bit_5	Bit_4	Bit_3	Bit_2	Bit_1	Bit_0
Hybrid	_13	_03	_12	_02	_11	_01	_10	_00

The PRO/A readout chip has default settings which contains only "0" in all register bits (subtraction mode is on, calibration and current compensation circuitries are off, all 32 digital outputs are enabled for trigger pulses, all analog outputs are disabled, no channels are connected to the calibration input). There is no need to change these during startup, but in a case of change some recommendations must be considered:

1. While programming one or more hybrids, the data in neighbouring bits must be protected against overwriting.
2. The following table shows how to program the preamplifier's gain by two bits in the sequencer code:

Table A.5: Gain stages of the PRO/A readout chip

Gain stage	small	medium	default	high
Gain select bit_0	1	1	0	0
Gain select bit_1	0	1	0	1

3. It is impractical to connect more than one odd and one even ASIC channels to the "Odd" and "Even" calibration inputs.

### ASICs Download Control

The procedure starts after "Load" went high if CR Bit\_2 was set to "1" before. All hybrids are read out in parallel with common data strobe. The received data is compared with the RAM content and a status report for every detector module is generated. A "1" means successful readback for the corresponding hybrid (see table A.5) while "0" shows a failure.

Example: set gain to "Small" for all hybrids,  
check that they were loaded properly.

```
Set "Sync" = "1"
Set "Load" = "0"
  Set "Data" = "01" (hex) % Selecting the control register %
  Set "Sync" = "0"
    Set "Data" = "C6" (hex) % Assigning the control register %
  Set "Sync" = "1"
    Set "Data" = "4E" (hex) % Selecting the gain stage bit_0 %
  Set "Sync" = "0"
    Set "Data" = "FF" (hex) % Assigning the gain stage bit_0 %
  Set "Sync" = "1"
    Set "Data" = "4F" (hex) % Selecting the gain stage bit_1 %
  Set "Sync" = "0"
    Set "Data" = "00" (hex) % Assigning the gain stage bit_1 %
  Set "Sync" = "1"
Set "Load" = "1"
```

### Supply Voltage Control

A voltage drop below 10% is being detected for the front-end power supplies: +5.0V for the CAN  $\mu$ controller, +3.3V for most of components, +2.5V for the ACEX core and +1.8V for the APEX core. For  $\pm 2.0$ V analog and  $\pm 2.0$ V digital supplies of the pad hybrids both, undervoltage and overvoltage within 10% levels are indicated. Voltage failures trigger corresponding bits (watchdogs) in the status register, see table A.6. A "1" denotes the normal value for the given voltage while "0" shows an alarm. The "Sync"  $\uparrow$  during "Load" = "1" will reset these watchdogs if the tripped voltages got recovered.

Table A.6: Matching between supply voltages and data bits

Position	Bit_7	Bit_6	Bit_5	Bit_4	Bit_3	Bit_2	Bit_1	Bit_0
Voltage	+5.0	+3.3	+2.5	+1.8	-2.0D	+2.0D	-2.0A	+2.0A

### Identifier Registers

Two registers  $0x7D$  and  $0x7E$  are reserved to keep the identifier word. These can be assigned individually or filled during the block transfer. The remaining memory is dedicated to the CAN  $\mu$ controller for storage of temperature values. The temperature measurement is performed by the CAN chip itself and not covered in this description.

Below is given a memory initialization file which contains all necessary data for the BST-Pad slow control system:

```

depth = 2048; % Memory size is required %
width = 8;    % Enter decimal numbers %

ADDRESS_RADIX = DEC; % Radices are optional. Enter BIN, DEC, %
DATA_RADIX = BIN;    % HEX, OCT; unless otherwise specified %
                    % radices = HEX %

content
begin
    0: 00000000; % This memory cell is not used %

    1: 11000111; % Set thresholds, download and check %
           % ASICs and read out of a check status %
    2: 11111111; % Process all DAC channels %

    3: 01000010; % Default threshold for hybrid_10: -110 mV %
    4: 01000010; % Default threshold for hybrid_11: -110 mV %
    5: 01000010; % Default threshold for hybrid_12: -110 mV %
    6: 01000010; % Default threshold for hybrid_13: -110 mV %
    7: 01000010; % Default threshold for hybrid_03: -110 mV %
    8: 01000010; % Default threshold for hybrid_02: -110 mV %
    9: 01000010; % Default threshold for hybrid_01: -110 mV %
    10: 01000010; % Default threshold for hybrid_00: -110 mV %

    11: 00000000; % This memory cell is not used %

    [12..43]: 00000000; % Test enable = "Off" for all pads %
    [44..75]: 00000000; % Trigger output = "On" for all pads %

    76: 00000000; % Calibr. mode = "Off" for all hybrids %
    77: 00000000; % Current comp. = "Off" for all hybrids %
    78: 00000000; % Gain select bit_0 = "0" for all hybrids %
    79: 11111111; % Gain select bit_1 = "1" for all hybrids %
    80: 00000000; % Analog output = "Off" for all hybrids %
    81: 00000000; % Individual mode = "Off" for all hybrids %
    82: 00000000; % Negative signal = "Off" for all hybrids %
    83: 00000000; % Time-over-thres. = "Off" for all hybrids %

    [84..2047]: 00000000; % This memory area is not used %
end;
```

## A.2 Data Reduction Subsystem

All six front-end boards and one master card (fig. A.3), perform the trigger data reduction. This section gives detailed information how to prepare those components for data processing.

### A.2.1 Setting up the Front-end

Downloading of trigger masks to the front-end is realized via the CAN interface. The "ACX\_APX" signal must be set to "1". The CAM capacity for masks amounts to 256 long words (32 bits each). The APEX chip on the front-end board contains 4 CAM modules. A combination of two bits in the control register provides a "CAM write enable" signal for one of them, see table A.7.

Table A.7: CAM multiplexer

Bit_1	Bit_0	CAM purpose
0	0	veto masks for the even sector
0	1	veto masks for the odd sector
1	0	trigger masks for the even sector
1	1	trigger masks for the odd sector

Each mask is transmitted as a block of data. Its length amounts to 4 bytes for masks with exact matching and to 8 bytes for masks with "don't care" conditions ("X"). In the latter case **Bit\_2** in the control register must be set to "1", otherwise to "0". The "Load" signal must be set to "0" for writing, the "Sync" ↓ latches the address (except for the control register) and "Sync" ↑ - the data values. A CAM readout is not possible in this design. The following sequence has to be maintained to download a mask properly:

1. Control bits **Bit\_0**, **Bit\_1** and **Bit\_2** are assigned with the first "Sync" ↓. The block transfer procedure starts if all other five bits contain zeros, otherwise the whole byte can be treated as a free address. This helps the processor to distinguish between a new mask and the identifier.
2. The first data byte corresponds to the first BST-Pad plane with respect to the interaction vertex (disk "0").
3. The second "Sync" ↓ latches the mask address (0 to 255). The masks are sorted accordingly to their ascending occurrence (decreasing radius of the track projection onto the SPACAL  $x$ - $y$  plane). This order must

be kept through all CAM addresses - it is particularly important for the L2TT trigger data.

4. The second, the third and the fourth data bytes correspond to the next detector planes respectively. The mask address is protected against overwriting until the fourth byte has been reached.
5. The CAM access and the mask exchange take place during the next block transfer and require two clock cycles. Therefore at least two additional "Sync" ↑ pulses must be sent for the last mask. This can be combined with setting up the pipeline depth at *7F* (hex) which defaults to 20 and the identifier registers *7D* (hex) and *7E* (hex).

Example: load the trigger mask "1234" over the address *66* (hex) for subsector 0 with "X"-condition in the third detector plane.

```

Set "Sync" = "1"
Set "Load" = "0"
  Set "Data" = "06" (hex) % Assigning the control register %
Set "Sync" = "0"
  Set "Data" = "01" (hex) % Mask pattern for the 1st plane %
Set "Sync" = "1"
  Set "Data" = "66" (hex) % Assigning the mask address %
Set "Sync" = "0"
  Set "Data" = "02" (hex) % Mask pattern for the 2nd plane %
Set "Sync" = "1", "0"
  Set "Data" = "04" (hex) % Mask pattern for the 3rd plane %
Set "Sync" = "1", "0"
  Set "Data" = "08" (hex) % Mask pattern for the 4th plane %
Set "Sync" = "1", "0"
  Set "Data" = "00" (hex)
Set "Sync" = "1", "0"
  Set "Data" = "00" (hex)
Set "Sync" = "1", "0"
  Set "Data" = "04" (hex) % "X"-pattern for the 3rd plane %
Set "Sync" = "1", "0"
  Set "Data" = "00" (hex)
Set "Sync" = "1", "0"
Set "Sync" = "1", "0"
Set "Sync" = "1"
Set "Load" = "1"

```

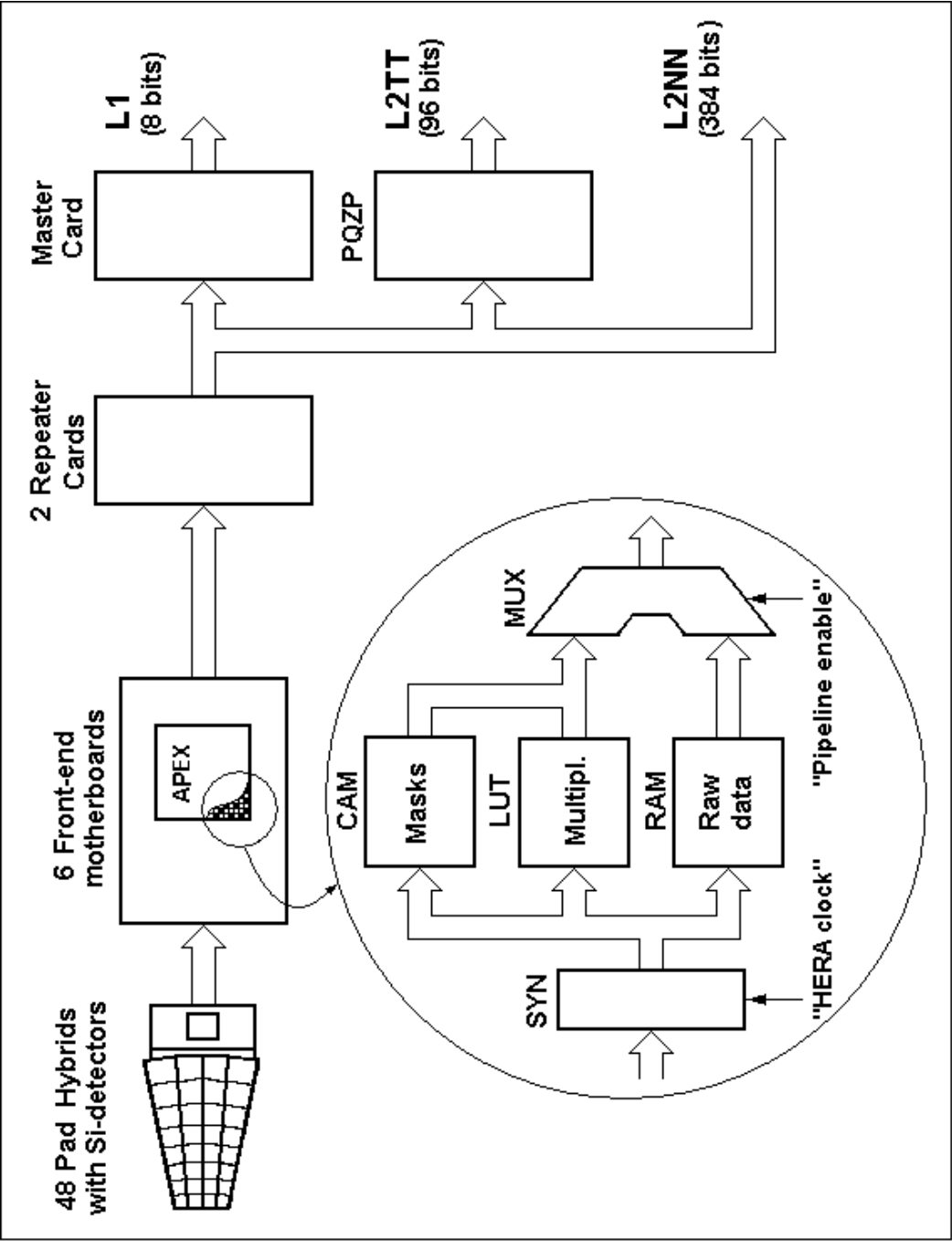


Figure A.3: Block diagram of the BST-Pad data reduction system.



## A.2.2 Setting up the Master Card

### CAN System

The VME-module VIPC616 interfaces six front-end boards equipped with CAN micro-controllers (nodes) to the BST-Pad slow control system. According to the CAN specification every node has an unique address, see table A.8. The master card carries a node too with the address "6" (hex).

Table A.8: CAN components of the front-end

Node address	"D"	"E"	"F"	"A"	"B"	"C"
Front-end board	0	1	2	3	4	5
BST sector in $\phi^\circ$	0-45	45-90	90-135	225-270	270-315	315-360

### Identifier and Status Registers

Assignment of the identifier register is done via the CAN interface by help of the "Load", "Sync" and "Csel" control signals described above (the latter is an analogon of the "ACX\_APX" switch). The lower and upper bytes of the ID word are stored on the ACEX chip (the "Csel" has to be "0") under the addresses 7D (hex) and 7E (hex).

The status word is formed by signals from the front-end boards and from the repeater cards. The "LAM" status of channels 0...5 is indicated by bits "0...5" of the status register. A "1" shows that the corresponding board is ready for data taking. Bit\_6 and Bit\_7 indicate the power supply status of the first and the second repeater cards, respectively, and Bit\_8 indicates the supply status of the master card itself. A "1" denotes good operating conditions and can be used to improve the data reliability. All other bits are set to zero.

Both, the identifier and the status words are read out via the VME bus. The current base address of the master card is 9066 (hex) where the last two digits are preselected by hardware switches on the board. Two address offsets: 0000 (hex) for the identifier and 0004 (hex) for the status registers are predefined. The master card will generate a bus error signal if the offset is any other than those specified.

### Test Mode Select

The "Pipeline enable" and the "Fast clear" signals as well as the HERA clock frequency are provided by the H1 central trigger system via a backplane connector of the master card. For test purposes these signals can also be

applied from front panel connectors, in this case the "Fast clear" pulse must have an inverse polarity. To use the master card outside the STC crate a jumper XP7 (see the circuit diagram) has to be set. This insures a stable board operation because without any signal source the backplane receivers have a tendency to oscillate.

### Clock Adjustment

The master card uses strobes of two repeaters to latch the trigger data from the front-end. The data processing is synchronized to the HERA clock frequency and has programmable delays for all signals with respect to each other. With a multi-position switch SA1 it is possible to delay the running algorithm as a whole by up to 100 ns in 10 equidistant steps (in practice: move within one HERA clock period). It is particularly important for separating the raw data from the radiation monitor pulses.

### Front Panel Indicators

A green and a red LED on the front panel visualize trigger and veto events, correspondingly. These indicators are driven by mono-flops with 100 ms period and 10% duty cycle.

## A.2.3 Setting up the Repeater Card

### Test Mode Select

The "Pipeline enable" and the "Fast clear" signals as well as the HERA clock frequency are provided by the H1 central trigger system via a backplane connector of the repeater card. For test purposes these signals can also be provided from the front panel connectors, in this case the "Fast clear" pulse must have an inverse polarity.

Table A.9: Signal sources for the front-end

XP7 shunts	Backplane	Front panel	Auto-sequence	Pushbutton
1-2			Set	Set
3-4		Set	★)	★)
5-6				Set

★) Must be set if the clock frequency is provided via the front panel connector.

Utilizing an external clock frequency the repeater card is able to emulate commands of the central trigger with a programmable period and duty cycle

for the "Pipeline enable" signal. The on-board SB1 pushbutton can be used as an advanced clock generator to which the control signals are synchronized. The last option needs also an external frequency for a special subroutine which prevents the button contact chatter. Routing of the control and clock signals to the front-end is done by setting shunts between contact groups of the XP7 connector, see table A.9. Important: a quasi-complementary signal "L1Keep" is sent to the front-end instead of the "Pipeline enable", because the latter starts usually after the "L1Keep" has been removed. That allows for "fresh" data to "ripple" through the pipeline.

Each repeater card watches "LAM" signals from the front-end boards. Those with "LAM" = "0" inhibit data strobes to the master card and to the PQZP system. This excludes any front-end boards being not configured from trigger decisions and insures for them a zero content in the TSCD bank #12. In test mode this option can be disabled individually for channels "0...2" and "3...5" by setting shunts between contact groups 11-12, 13-14 and 15-16 of the connector XP7 (see the circuit diagram).

### **Clock Adjustment**

With a multi-position switch SA2 the rising edge of the "L1Keep" signal can be delayed by up to 100 ns in 10 equidistant steps. In the same way the SA3 switch delays the falling edge of the "L1Keep" signal and the SA4 delays the data strobe accompanying the L1 trigger word. The SA1 switch provides a common variable delay for all processes with respect to the clock pulses. The global timing scheme of the data reduction algorithm is given in fig. A.4.

### **Front Panel Indicators**

A red LED on the front panel shows a "heartbeat" of the repeater card. Driven by a mono-flop (0.7 Hz and 3% duty cycle), it is flashing when both, the "Run" signal and the HERA clock frequency, are provided by the central trigger. A green LED indicates the "Pipeline enable" signal when it is active.

## **A.3 Technical documentation**

All circuit diagrams for the pad hybrid, for the front-end, for the power supply system, for the repeater card and for the master card, the firmware code sources and the text of this thesis can be found in the internet under:

<http://www.desy.de/~tsurin/Data/>

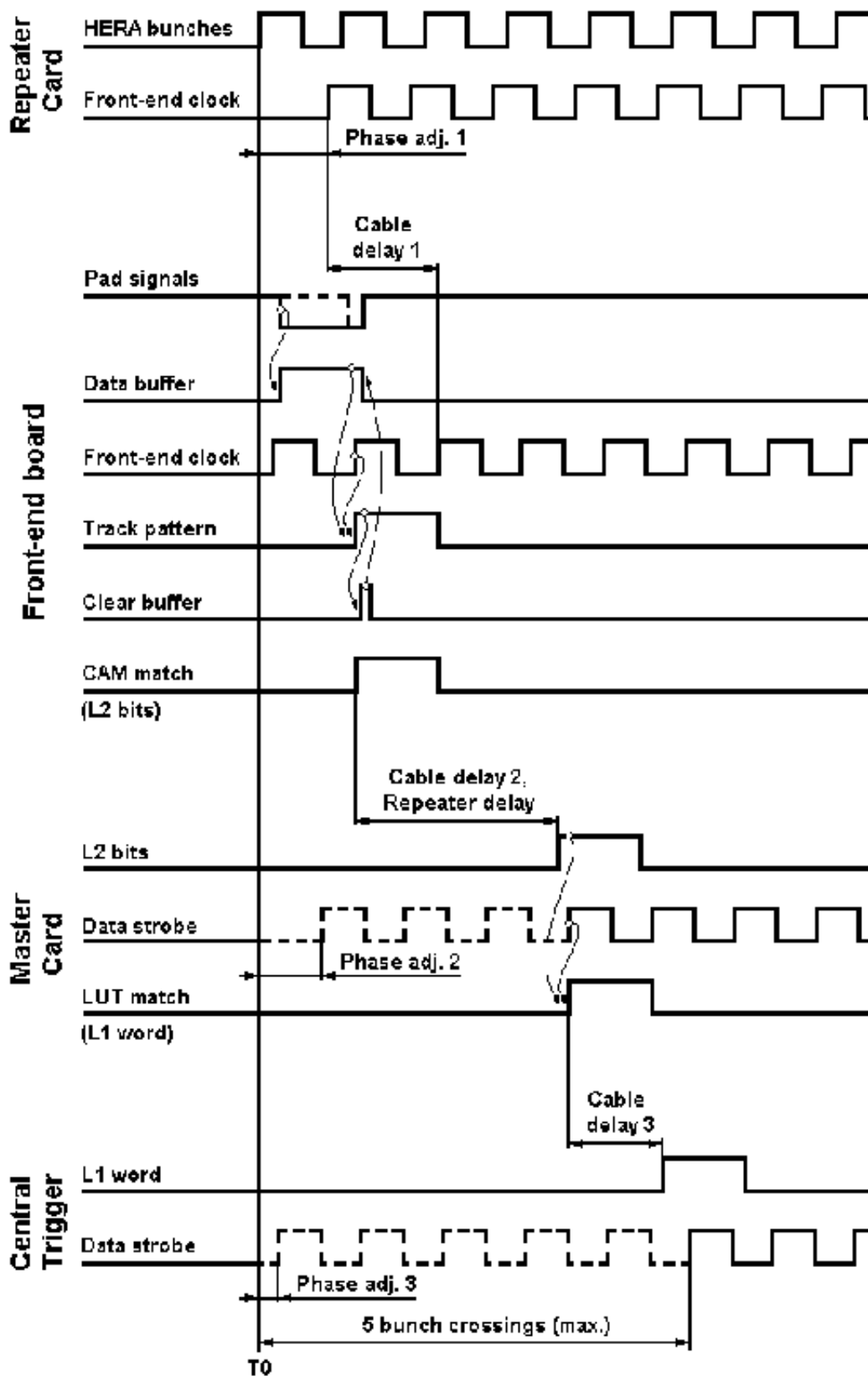


Figure A.4: Delays of the BST-Pad data at different system levels with respect to the unique  $e^{\pm}P$  interaction time  $T_0$ .

# Appendix B

## Topological Trigger Data

The principle of data delivery shown in fig 2.11 needs explanations on the data structure and, for completeness, on the data treatment. The first eight BST-Pad words transmitted contain the polar and the azimuthal angles of the track candidates. The word position in this sequence corresponds to one front-end board whose  $\phi$ -sectors - even and odd, are represented by lower and upper bytes, see table B.1.

Table B.1: Data package for the L2TT

Clock cycle	Board	Sectors	Range in $\phi^\circ$
1	0	0 (lower byte) 1 (upper byte)	0.0 - 22.5 22.5 - 45.0
2	1	2 (lower byte) 3 (upper byte)	45.0 - 67.5 67.5 - 90.0
3	2	4 (lower byte) 5 (upper byte)	90.0 - 112.5 112.5 - 135.0
4		—	
5	3	10 (lower byte) 11 (upper byte)	225.0 - 247.5 247.5 - 270.0
6	4	12 (lower byte) 13 (upper byte)	270.0 - 292.5 292.5 - 315.0
7	5	14 (lower byte) 15 (upper byte)	315.0 - 337.5 337.5 - 360.0
8		—	

The track or veto candidates in every sector are denoted by a combination of Bit\_7 and Bit\_6 in the corresponding data bytes, see table B.2. The track information is coded by Bit\_5...Bit\_1 in table B.3.

Table B.2: Truth table for coding the trigger and veto signals

Bit_7	Bit_6	Event class	Purpose	Bit_5 ... Bit_1
1	0	Vertex track	Trigger only	SPACAL radius
1	1	Vertex track.	Trigger/Veto	SPACAL radius
0	1	Background	Veto only	Hit multiplicity
0	0	—	—	Hit multiplicity

Validation of a track candidate is possible online by matching the BST-Pad signals to the triggered SPACAL cells. It is, therefore, more convenient for the topological trigger to dial with a track projection onto the SPACAL  $r-\phi$  plane rather than with a polar angle  $\theta$ . For a variety of simulated events (the particles momenta spread between 6 GeV/c and 27 GeV/c) these radial projections were calculated.

Each trigger mask has a certain acceptance in  $z$ ,  $\theta$  and  $\phi$ , and therefore allows for the projection smearing. The distributions of the SPACAL radii obtained for all masks approach a Gaussian ( $\chi^2$  / degrees of freedom  $\approx 2$ ) with a standard deviation varying from 10mm (for the mask "0112") to 52mm (for the mask "5780").

The unique mask number (CAM address) matches the mean radius of the track projection, whose uncertainty for every single event does not degrade much when up to 16 neighbouring masks are coded to give a common signal. If several masks have triggered, the algorithm calculates their total projection range in which the L2TT can search for the local energy deposits (clusters) in the SPACAL. The five bits of the BST L2TT data word become enough to cover all possible track geometries.

Each entry in table B.3 represents a group of masks. A gap of 4mm between groups "00100" and "00101", "10010" and "10011", "11001" and "11010" is still less than a size of the SPACAL electromagnetic cell equal to 4cm.

The number of masks and their permutations necessary to reach  $\approx 99\%$  trigger efficiency is about 100, therefore more than one half of the CAM area stays unconfigured and many bit combinations in table B.3 are not used, but they are reserved for the 2-hit track candidates.

Input receivers AM26LV32 of the repeater card drive high potentials (log-

ical "1") in a case of unpowered front-end or unplugged input cables. Therefore all signals from the front-end have an inverse polarity to ensure a zero content in the TSCD bank #12 for missing hardware. In the offline analysis these data are inverted again.

Table B.3: Truth table for coding the track geometry

Bit_5...Bit_1	SPACAL radius, mm	Mask addresses
Cluster localizations for single tracks		
00001	152...180	00...0F (hex)
00010	180...197	10...1F (hex)
00011	197...215	20...2F (hex)
00100	215...232	30...3F (hex)
00101	236...242	40...4F (hex)
00110	242...260	50...5F (hex)
00111	260...288	60...6F (hex)
01000	288...354	70...7F (hex)
Multiple tracks confined to narrow ranges		
10001	152...197	00...1F (hex)
10010	197...232	20...3F (hex)
10011	236...260	40...5F (hex)
10100	260...354	60...7F (hex)
Multiple tracks confined to broad ranges		
11001	152...232	00...3F (hex)
11010	236...354	40...7F (hex)
Multiple tracks in the whole acceptance		
11101	152...354	00...7F (hex)

# Appendix C

## HERA Background Control

The task of the radiation monitor is a computation of the count rate for each silicon sensor. This algorithm is a part of the data reduction sub-system of the BST-Pad distributed between the front-end and the VME interface. This note helps all experts involved to understand some important software solutions and gives an exercise on the VHDL programming.

### Front-end Firmware

Six front-end boards transmit their intermediate results to the master card. During the H1 sampling phase these data are stored in the TSCD bank #12 making possible the offline background studies, in particular its azimuthal distribution. A strong  $z$ -dependence of the count rate was observed in each  $\phi$ -sector, nevertheless a maximum value over 4 detector planes is being processed. Two independent subroutines (for the even and odd sectors) are running in parallel on each motherboard. As a transmitting protocol a pulse number modulation algorithm was chosen.

For each silicon sensor a variable **Shovel** acquires a number of triggered pads in every bunch crossing. The counter **Basket** is incremented by this number synchronously to the **HERA** clock frequency during the acquisition time denoted by a parameter **Collect**. A signal **Firewood** is always equal to the maximum **Basket** value and determines, therefore, the number of pulses to be sent to the Master card (PNM package).

During a short gap (1 clock period) between two acquisition intervals the PNM package is copied to an **Oven** counter which is decremented afterwards one by one synchronously to the clock frequency until its value reaches a zero. Together with "emptying" the **Oven** content the output clock pulses are generated. This PNM process is blocked by a signal **PH\_Lock** for 4 bunch crossings during a raw data transmission.



```

-----
Shovel <= SUM_of_ONES_8(Sensor);
Collect <= Gate and (not Push);
-----
process(Worker, HERA, Shovel, Collect)
begin
  if (Worker = '1') then
    Basket <= 0;
  elsif (HERA'event and HERA = '0') then
    if (Collect = '1') then
      Basket <= Basket + Shovel;
    else
      null;
    end if;
  end if;
end process;
-----
Firewood <= Basket + Tray;
-----
process(HERA, Timer, Limit, Firewood, Tray, PH_Lock)
begin
  if (HERA'event and HERA = '1') then
    if (Timer = Limit) then
      Oven <= Firewood;
    elsif (Tray > 0 and PH_Lock = '0') then
      Oven <= Oven - 1;
    else
      null;
    end if;
  end if;
end process;
-----
process (Tray, HERA)
begin
  if (Tray > 0) then
    RAD_MON <= HERA;
  else
    RAD_MON <= '0';
  end if;
end process;
-----

```

The acquisition period lasts 50 ms. It is long enough to obtain a reasonable statistics. On the other hand it is short to provide a constant load for the master card - the number of pulses sent out at once should not be too large. The maximum number of integrated hits per 50 ms may reach  $4 \cdot 10^6$  that requires up to 80 MHz carrying frequency for the PNM. The actual bandwidth is limited by the clock frequency of 10 MHz, but the detector is not supposed to work with such a permanent radiation load. In spikes, nevertheless, the rate may exceed  $10^7$  hits per second. In this case the remaining number of pulses **Tray** is added to the new PNM package being prepared.

```
-----
process(HERA, Inhibit, Oven)
begin
  if (HERA'event and HERA = '0') then
    if (Inhibit = '0') then
      Tray <= Oven;
    else
      null;
    end if;
  end if;
end process;
-----
```

```
process(Timer, Gate)
begin
  if (Timer = 0 and Gate = '0') then
    Worker <= '1';
  else
    Worker <= '0';
  end if;
end process;
-----
```

```
process(HERA, Limit, Basket)
begin
  if (HERA'event and HERA = '1') then
    if ((Limit - 7) <= Basket) then
      Overflow <= '1';
    else
      Overflow <= '0';
    end if;
  end if;
end process;
-----
```

All **Basket** counters are cleared in the beginning of a new acquisition interval by help of a **Worker** signal. If any of them exceed a certain value **Limit** before the acquisition interval is finished, signals **Overflow** are generated for the corresponding hybrids and their disjunction **Push** starts the PNM and forces the acquisition timer reset (signal **Door**). Two auxiliary signals **Inhibit** and **Gate** allow for safe condition assignments for better program reliability.

```

-----
Push <= Overflow;
-----
process(Gate, Push)
begin
  if (Gate = '0') then
    Door <= '0';
  elsif(Push'event and Push = '1') then
    Door <= '1';
  end if;
end process;
-----
process(HERA, Door, Limit)
begin
  if (HERA'event and HERA = '0') then
    if (Door = '1') then
      Timer <= Limit - 1;
    else
      Timer <= Timer + 1;
    end if;
  end if;
end process;
-----
process(HERA, Timer, Limit)
begin
  if (HERA'event and HERA = '1') then
    if (Timer = Limit) then
      Inhibit <= '1';
    else
      Inhibit <= '0';
    end if;
  end if;
end process;
-----

```

```

-----
process(HERA, Timer, Limit)
begin
  if (HERA'event and HERA = '1') then
    if (Timer < (Limit - 1)) then
      Gate <= '1';
    else
      Gate <= '0';
    end if;
  end if;
end process;
-----

```

### Master Card Firmware

The subroutine running on the APEX chip of the Master card utilizes twelve counters **Basket** to accumulate PNM packages from the BST-Pad sectors during the acquisition time denoted by a signal **Collect**. Incrementing of those counters is blocked by a signal **PH\_Lock** during the raw data transmission. The acquisition time amounts to one second that normalizes all count rates to one Hertz. Signal **Worker** clears all accumulators in the beginning of a new acquisition interval.

The modulation frequency **Firewood** amounts to a maximum **Basket** rate (0...10 MHz) minus a presettable pedestal value (0...25.5 kHz). The latter allows for rejection of an electronics noise and for using lower trigger thresholds. It is found as:  $f_{ped}(Hz) = 100 \cdot Data$  (dec), where the pedestal data **PED\_REG** (1 byte) is stored at the address *7F* (hex). The default data is zero. To change it via the CAN interface the given address and the new value have to be latched by "Sync" ↓ and "Sync" ↑ respectively while keeping "Csel" = "1" and "Load" = "0".

Mixing of carrier and modulation frequencies is realized with a cyclic counter **FRQ\_CNT** the period of which **Result** (the counter limit in terms of clock pulses) is computed dynamically as an integer quotient of division:

$$Result[clocks] = \frac{f_{carrier}[clocks \cdot sec^{-1}]}{(1 + Firewood)[sec^{-1}]}$$

During every **FRQ\_CNT** cycle a standard (96 ns) pulse is generated and sent to the output. Thus the **RAD\_MON** signal rate obtains discrete values between  $1/2 \cdot f_{clock}$  and  $1/10000000 \cdot f_{clock}$ . A logarithmic scale provides a smooth curve for the plotted rate history. An integrating logics of the central trigger compute a value for the current radiation load of the BST-Pad.

```

-----
process(Worker, RM_int, Collect)
begin
  if (Worker = '1') then
    Basket <= 0;
  elsif (RM_int'event and RM_int = '1') then
    if (Collect = '1') then
      Basket <= Basket + 1;
    else
      null;
    end if;
  end if;
end process;
-----

Firewood <= Basket - Pedestal;
-----

process(Clock)
begin
  if (Clock'event and Clock = '1') then
    Timer <= Timer + 1;
  end if;
end process;
-----

process(Clock, Timer)
begin
  if (Clock'event and Clock = '0') then
    if (Timer < (Limit - 1)) then
      Collect <= '1';
    else
      Collect <= '0';
    end if;
  end if;
end process;
-----

process(Timer, Collect)
begin
  if (Timer = 0 and Collect = '0') then
    Worker <= '1';
  else
    Worker <= '0';
  end if;
end process;
-----

```

```
-----
process(Clock, FRQ_DEL, Result)
begin
  if (Clock'event and Clock = '1') then
    if (FRQ_DEL /= Result) then
      FRQ_CNT <= FRQ_CNT + 1;
    else
      FRQ_CNT <= 0;
    end if;
  end if;
end process;
-----
process(Clock, FRQ_CNT)
begin
  if (Clock'event and Clock = '0') then
    FRQ_DEL <= FRQ_CNT;
  end if;
end process;
-----
process(FRQ_CNT)
begin
  case FRQ_CNT is
    when 1 =>
      RAD_MON <= '1';
    when others =>
      RAD_MON <= '0';
  end case;
end process;
-----
```

# Bibliography

- [1] M. Gell-Mann, "A Schematic Model of Baryons and Mesons", Phys. Lett. 8 (1964) pp. 214-215.
- [2] L. W. Whitlow et al., "Precise Measurements of the Proton and Deuteron Structure Functions from a Global Analysis of the SLAC Deep Inelastic Electron Scattering Cross Sections", Phys. Lett. B 282 (1992) pp. 475-482.
- [3] BCDMS Collaboration, A. C. Benvenuti et al., "A High Statistics Measurement of the Proton Structure Functions  $F_2(x, Q^2)$  and  $R$  from Deep Inelastic Muon Scattering at High  $Q^2$ ", Phys. Lett. B 223 (1989) pp. 485-489.
- [4] H1 Collaboration, I. Abt et al., "Measurement of the Proton Structure Function  $F_2(x, Q^2)$  in the Low- $x$  Region at HERA", Nucl. Phys. B 407 (1993) pp. 515-535.
- [5] ZEUS Collaboration, M. Derrick et al., "Measurement of the Proton Structure Function  $F_2$  in  $ep$  Scattering at HERA", Phys. Lett. B 316 (1993) pp. 412-426.
- [6] G. Herrera Corral, "Review of HERA Experiments", Proc. of the VIII ICFA School "Instrumentation in Elementary Particle Physics", Istanbul, Turkey, June 28 - July 10, 1999, AIP Vol. 536 (2000) pp. 267-287.
- [7] D. H. Perkins, "Neutrino Interactions", Proc. of the XVI Int. Conf. on High Energy Physics, Chicago, USA, September 13-26, 1972, NAL Vol. 4 (1973) pp. 189-247.
- [8] H. Abramowicz, A. Caldwell, "HERA Collider Physics", Reviews of Modern Physics 71 (1999) pp. 1295-1297.
- [9] M. Klein, "On the  $Q^2$ ,  $x$  Range at HERA", Proc. of the Workshop on Physics at HERA, Hamburg, Germany, October 29-30, 1991, HB-Druck Vol. 1 (1992) pp. 71-76.

- [10] A. A. Glazov, "Measurement of the Proton Structure Functions  $F_2(x, Q^2)$  and  $F_L(x, Q^2)$  with the H1 Detector at HERA", DESY-Thesis: 1998-005 (1998) p. 40.
- [11] H1 Collaboration, C. Adloff et al., "Deep-Inelastic Inclusive  $ep$  Scattering at Low  $x$  and Determination of  $\alpha_s$ ", Eur. Phys. J. C 21 (2001) pp. 33-61.
- [12] D. Eckstein, "Messung der Longitudinalen Strukturfunktion  $F_L(x, Q^2)$  mit dem HERA-Experiment H1" DESY-Thesis: 2002-008 (2002) pp. 65-68.
- [13] M. Seidel "Luminosity Upgrade of HERA", Proc. of the Particle Accelerator Conf. New York, U.S.A., March 29 - April 2, 1999, Vol. 1 (1999) pp. 34-36.
- [14] H. Abramowicz, A. Caldwell, "HERA Collider Physics", Reviews of Modern Physics 71 (1999) p. 1400.
- [15] E. Gianfelice-Wendt, "HERA Upgrade Plans", Proc. of the 6-th European Particle Accelerator Conf., Stockholm, Sweden, June 22-26 1998, Vol. 1 (1998) pp. 118-122.
- [16] H1 Calorimeter Group, B. Andrieu et al., "The H1 Liquid Argon Calorimeter System", Nucl. Instr. and Meth. A 336 (1993) pp. 460-498.
- [17] H1 SPACAL Group, R. D. Appuhn et al., "The H1 Lead/Scintillating-Fibre Calorimeter", Nucl. Instr. and Meth. A 386 (1997) pp. 397-408.
- [18] J. Buerger et al., "The Central Jet Chamber of the H1 Experiment", Nucl. Instr. and Meth. A 279 (1989) pp. 217-222.
- [19] H. Henschel, R. Lahman, "The Backward Silicon Tracker of the H1 Experiment at HERA", Nucl. Instr. and Meth. A 453 (2000) pp. 93-97.
- [20] W. Braunschweig et al., "Results from a Test of a Pb-Cu Liquid Argon Calorimeter", Nucl. Instr. and Meth. A 265 (1988) pp. 430-433.
- [21] W. Braunschweig et al., "Performance of a Pb-Cu Liquid Argon Calorimeter with an Iron Streamer Tube Tail Catcher", Nucl. Instr. and Meth. A 275 (1989) pp. 246-257.



- [22] F. Moreau, "The low Noise L1 Trigger of the H1 Lead / Scintillating-Fibre Electromagnetic Calorimeter", Nucl. Phys. B 61B (Proc. Suppl.) (1998) pp. 132-136.
- [23] H1 SPACAL Group, T. Nicholls et al., "Performance of an Electromagnetic Lead / Scintillating-Fibre Calorimeter for the H1 Detector", Nucl. Instr. and Meth. A 374 (1996) p. 155.
- [24] T. Carli et al., "Proposal to Upgrade the LAR Calorimeter Trigger: the Jet Trigger", DESY PRC Report 99-02 (1999), Unpublished.
- [25] M. Cuje et al., "H1 High Luminosity Upgrade 2000 CIP and Level 1 Vertex Trigger", H1 note H1-01/98-535 (1998), Unpublished.
- [26] H1 Collaboration, "Proposal for an Upgrade of the H1 Forward Track Detector for HERA 2000", DESY PRC Report 98-08 (1998), Unpublished.
- [27] G.A. Beck et al., " $e^\pm$  Identification Using the Drift Chambers and Transition Radiators of the H1 Forward Track Detector", Nucl. Instr. and Meth. A 367 (1995) pp. 228-232.
- [28] W. Braunschweig et al., "A Forward Silicon Tracker for H1", DESY PRC Report 99-01 (1999), Unpublished.
- [29] T. Wolf et al., "A Drift Chamber Track Finder for the First Level Trigger of the H1 Experiment", Nucl. Instr. and Meth. A 323 (1992), pp. 537-541.
- [30] S. A. Baird et al., "A Fast Track Trigger with High Resolution for H1", DESY PRC Report 99-06 (1999), Unpublished.
- [31] V. Arkadov, "Measurement of the Structure Functions  $F_2$  and  $F_L$  at Low  $x$ ", Nucl. Phys. B 79 (Proc. Suppl.) (1999) pp. 179-181.
- [32] D. Eckstein, "A New Measurement of the Deep Inelastic Scattering Cross Section and of  $F_L$  at Low  $Q^2$  and Bjorken  $x$  at HERA", Proc. of the 9th Int. Workshop on Deep Inelastic Scattering, Bologna, Italy, April 27 - May 1, 2001, World Scient. (2002), pp. 376-379.
- [33] T. Laštovička, "Measurement of the Inclusive Deep Inelastic Scattering Cross Section at  $Q^2 \sim 1 \text{ GeV}^2$  with the H1 Experiment", Acta Physica Polonica B Vol. 33 (2002) Nr. 10, pp. 2835-2840.

- [34] H1 Collaboration, C. Adloff et al., "Elastic photoproduction of  $J/\Psi$  and  $\Upsilon$  mesons at HERA", Phys. Lett. B 483 (2000) pp. 23-35.
- [35] E. Peppel, "First Results with the Backward Silicon Strip Detector", Nucl. Instr. and Meth. A 409 (1998) pp. 201-203.
- [36] V.Boudry et.al., "The inclusive Electron Trigger for SpaCal: Design and CERN-Test Results". H1 note H1-03/95-430 (1995), Unpublished.
- [37] H1 Collaboration, "Proposal for an Upgrade of the H1 Luminosity System and its Associated Electronics for HERA 2000", DESY PRC Report 98-05 (1998), Unpublished.
- [38] H. C. Schultz-Coulon et al., "A General Scheme for Optimization of Trigger Rates in an Experiment with Limited Bandwidth", IEEE Trans. Nucl. Sci., Vol 46 (1999) pp. 915-919.
- [39] S.Egli et al., "Calculating Event Weights in Case of Downscaling on Trigger Levels 1-4", H1 note H1-04/97-517 (1997), Unpublished.
- [40] A. Glazov et al., "ELAN Triggers in 1998/1999". H1 note H1-07/98-546 (1998), Unpublished.
- [41] H. Henschel et al., "A Silicon Pad Detector L1 Trigger for Deep Inelastic Scattering at Low  $x$  and  $Q^2$ ", H1 note h1-04/92-221 (1992), Unpublished.
- [42] W. J. Haynes et al., "The H1 Silicon Tracker Data Acquisition System", Nucl. Instr. and Meth. A 403 (1998) p. 319.
- [43] I. Tsourine, "Development of a Fast H1 Trigger using Silicon Pad Detectors" Nucl. Instr. and Meth. A 501/1 (2003), pp. 219-221.
- [44] J. Buerger et. al., "Design of a Silicon Backward Tracking Detector and Trigger for the H1 Experiment at the  $ep$  Collider HERA", DESY Preprint 93-002 (1993), p.6.
- [45] Micron Semiconductor Ltd., 1 Royal Buildings, Marlborough Road, Lancing, Sussex, BN15 8UN England, <http://www.micronsemiconductor.co.uk>
- [46] P. P. Allport et al., "FOXJET Biased Microstrip Detectors", Nucl. Instr. and Meth. A 310 (1991), pp. 155-159.
- [47] "Particle Data Group" Phys. Lett. B 170 (1986) p. 43.

- [48] J. L. Matthews, "The Distribution of Electron Energy Losses in Thin Absorbers", Nucl. Instr. and Meth. 180 (1981) pp. 573-579.
- [49] V. Radeka, "Signal, Noise and Resolution in Position-Sensitive Detectors", IEEE Trans. Nucl. Sci. NS-21 (1974) p. 53.
- [50] Ideas ASA, Veritasveien 9, Box 315, N-1323 Hovik, Norway, <http://www.ideas.no>
- [51] Austria Mikro Systeme International AG, Schlo Premstaetten, A-8141 Unterpremstaetten, Austria, <http://www.austriamicrosystems.com>
- [52] Cadence Design Systems Inc., 555 River Oaks Parkway, San Jose, CA 95134, U.S.A., <http://www.cadence.com>
- [53] Altera Corporation, 101 Innovation Drive, San Jose, California 95134, U.S.A., <http://www.altera.com>
- [54] Xilinx Inc., 2100 Logic Drive San Jose, CA 95124-3400, U.S.A., <http://www.xilinx.com>
- [55] IEEE Standard 1076-2002, IEEE, 3 Park Avenue, 17th Floor, New York, New York, 10016-5997 U.S.A., <http://www.ieee.org>
- [56] Koninklijke Philips Electronics N.V., Groenewoudseweg 1, 5621 BA, Eindhoven, Netherlands, <http://www.semiconductors.philips.com>
- [57] SBS Technologies, Memminger Str. 14, D-86159 Augsburg, Germany, <http://www.sbs.com>
- [58] National Instruments Corp., 11500 N Mopac Expwy Austin, TX 78759-3504, U.S.A., <http://www.ni.com>
- [59] Maxim Integrated Products Inc., 120 San Gabriel Drive, Sunnyvale, CA 94086 U.S.A., <http://www.maxim-ic.com>
- [60] Texas Instruments Incorporated, 12500 TI Boulevard, Dallas, TX 75243-4136, U.S.A., <http://www.ti.com>
- [61] IEEE Standard 1149.1-1990, IEEE, 3 Park Avenue, 17th Floor, New York, New York, 10016-5997 U.S.A., <http://www.ieee.org>
- [62] H. Krehbiel, "Standards for the Transmission of Bit Data in the H1 Trigger System through Twisted-Pair Flat Cables", H1 trigger note 12, DESY-F22/H1, (1989), Unpublished.

- [63] C. Beigbeder, D. Breton, "H1 PQZP System", H1-note H1-02/93-269, LAL Orsay (1993), Unpublished.
- [64] The VMEbus International Trade Association, PO Box 19658, Fountain Hills AZ 85269, U.S.A., <http://www.vita.com>
- [65] GMS Instruments Group, Thomas-Mann-Str. 16-20, D-90471 Nuernberg, Germany, <http://www.gossen.de>
- [66] Rohde & Schwarz Group, Muehldorfstrasse 15, 81671 Munich, Germany, <http://www.rohde-schwarz.de>
- [67] K. Stolze, "Untersuchung von Siliziumdetektoren fuer den Backward Silicon Tracker beim HERA Experiment H1", DESY-Dipl. Thesis in german (1993), Unpublished.
- [68] Tektronix GmbH., Vertrieb Stolberger Strasse 200, D-50933 Koeln, Germany, <http://www.tektronix.com>
- [69] LeCroy GmbH., Postfach 103767, D-69027 Heidelberg, Germany, <http://www.lecroy.com>
- [70] CAEN S.p.A., Via Vetraia, 11, 55049 - Viareggio (LU), Italy, <http://www.caen.it>
- [71] M. Kuhlen, "Statistics for Binned Distributions", H1-note H1-01/95-418 (1995), Unpublished.
- [72] W. R. Leo, "Techniques for Nuclear and Particle Physics Experiments", Springer-Verlag (1994), p. 50.
- [73] G. Baricchello et al., "Performance of Long Modules of Silicon Microstrip Detectors", CERN PPE/97-162 (1997), Unpublished.
- [74] D. H. Perkins, "Introduction to High Energy Physics", Addison-Wesley Publishing Company, Inc. 1972, p. 36.
- [75] B.B. Chaudhuri and P. Kundu, "Optimum circular fit to weighted data in multi-dimensional space", Pattern Recogn. Lett. 14 (1993) pp. 1-6.
- [76] V. V. Arkadov, "Measurement of the Deep Inelastic  $eP$  Scattering Cross Section using the Backward Silicon Tracker at the H1 Detector at HERA", DESY-Thesis: 2000-046 (2000) pp. 51-54.

- [77] D. Pitzl, "Shielding against synchrotron radiation", Minutes of Electron Ion Collider Accelerator Workshop, Brookhaven National Laboratory, February 26-27, 2002, Unpublished.
- [78] V. Andreev et. al., "Technical Report on the Beam Induced Backgrounds in the H1 Detector", H1 note H1-10/02-606, DESY Hamburg (2002), p. 6, Unpublished.
- [79] W. Hildesheim, M. Seidel, "An investigation into the radiation damage of the silicon detectors of the H1-PLUG calorimeter within the HERA environment", DESY report 95-139, (1995), p. 13.
- [80] "Stopping Powers for Electrons and Positrons", Report 37 of the International Commission on Radiation Units and Measurements, Bethesda MD, 1984.
- [81] "Radiation Quantities and Units", Report 33 of the International Commission on Radiation Units and Measurements, Bethesda, MD, 1980.
- [82] V. Andreev et. al., "Further Report on the Beam Induced Backgrounds in the H1 Detector", H1 note H1-01/03-607, DESY Hamburg (2003), p. 44, Unpublished.

# Lebenslauf

## Angaben zur Person

Name:	Ilya Petrovich Tsurin
Geburtsdatum:	25.02.1972 in Verhnaya Tura, Sverdlovsk Geb. (UdSSR)
Nationalität:	Russisch
Familienstand:	Ledig
Name des Vaters:	Petr Tsurin
Name der Mutter:	Olga Tsurina

## Ausbildungsweg

Okt 1987 - Mai 1989	Ergänzungsunterricht im Fach Physik an der Staatlichen Universität Novosibirsk
Sep 1989 - Feb 1995	Studium an der Staatlichen Technischen Universität im Ural – Fachrichtung Expe- rimentelle Physik.
Aug 1993 - Feb 1995	Studium am Universitäts-Forschungszentrum des Vereinten Instituts für Kernforschung – Fachrichtung Physik des Atomkerns. Diplom Arbeit am V.I.K. Dubna
Feb 1995	Diplom an der U.S.T.U.
Apr 1995 - Jun 1999	Mitarbeiter im V.I.K. als Ingenieur und seit 1998 als Forscher am Internationalen Projekt "Fobos".
Jul 1999	Beginn der Dissertation bei Prof. Dr. Th. Lohse an der Humboldt Universität zu Berlin unter Betreuung von Dr. M. Klein, DESY-Zeuthen.

# Vorträge

1. *The High Voltage Power Supply System for the FOBOS Forward Array*, International Workshop on Data Acquisition Systems for the Neutron Experiment Facilities (DANEF-97), Dubna, Russland, Juni 2-4, 1997.
2. *The BST-2000 trigger concept*, Workshop on H1 trigger system, Ringberg, Deutschland, Januar 23-26, 2000.
3. *Development of a Track Trigger for H1 using Silicon Pad Detectors*, Deutsche Physikalische Gesellschaft, Bereich Teilchenphysik, Dresden, Deutschland, März 20-24, 2000.
4. *Development of a Fast H1 Trigger using Silicon Pad Detectors*, The 10<sup>th</sup> International Workshop on Vertex Detectors VERTEX-2001, Brunnen, Schweiz, September 23-28, 2001.
5. *Triggering in the Backward Region of H1 using the BST*, Workshop on H1 trigger system, Ringberg, Deutschland, Januar 13-16, 2002.
6. *The upgraded H1 Backward Silicon Tracker*, Technisches Seminar an der Humboldt Universität zu Berlin, Berlin, Deutschland, Januar 18, 2002.
7. *A Silicon Pad Detector for Triggering on Low  $Q^2$  Events*, Deutsche Physikalische Gesellschaft, Bereich Teilchenphysik, Leipzig, Deutschland, März 18-22, 2002.

# Publikationen

1. *The front-end electronics and the data acquisition system of the FOBOS  $4\pi$ -array*, O. V. Strekalovsky et al., Proc. of the 16<sup>th</sup> Internat. Symp. on Nuclear Electronics, Varna, Bulgaria, September 12-18, 1994.
2. *A subnanosecond four-channel KA-251M time-to-number converter*, S. I. Merzlyakov et al., Instruments and Techniques of Experiment, vol.38 (1995) pp. 102-106.
3. *Spectroscopy of correlated fragments from the fission of hot nuclei performed at the FOBOS  $4\pi$ -array*, H.-G. Ortlepp et al., Proc. of the Internat. Conf. Low Energy Nuclear Dynamics (LEND'95), St. Petersburg, Russland, April 18-22, 1995.
4. *The High Voltage Power Supply System for the FOBOS Forward Array*, Yu. A. Astakhov et al., Proc. of the Internat. Workshop on Data Acquisition Systems for Neutron Experimental Facilities (DANEF-97), Dubna, Russland, Juni 2-4, 1997, pp. 321-325.
5. *The Binary and Ternary Decay of Hot Heavy Nuclei Produced in the Reaction  $^{14}\text{N}(34\text{ MeV}) + ^{197}\text{Au}$* , W. Wagner et al., Proc. of the 3<sup>rd</sup> Internat. Conf. Dynamical Aspects of Nuclear Fission, Casta-Paiernicka, Slovak Republic, August 30 - September 4, 1996, pp. 104-112.
6. *The Two-Sn Mode Observed in Cold Fission of Cm and Cf Isotopes*, Yu. V. Pyatkov et al., Proc. of the 4<sup>th</sup> Internat. School - Seminar Heavy Ion Physics, Dubna, Russland, September 22-27, 1997, pp. 720-722.
7. *The  $4\pi$ -fragment spectrometer FOBOS*, H.-G. Ortlepp et al., NIM A403 (1998) pp. 65-97.
8. *Development of a Fast H1 Trigger Using Silicon Pad detectors*, I. P. Tsourine, NIM A501/1 (2003) pp. 219-221.
9. *Photoproduction with a Leading Proton at HERA*, H1 Collaboration, C. Adloff et al. Nucl. Phys. B619 (2001) pp. 3-21.
10. *Measurement of Charged and Neutral Current Cross Sections in Electron-Proton Collisions at high  $Q^2$* , H1 Collaboration, C. Adloff et al., The Eur. Phys. J. C19 (2001) pp. 269-288.



11. *Measurement and QCD Analysis of Jet Cross Sections in Deep-Inelastic Positron-Proton Collisions at  $\sqrt{s}$  of 300 GeV*, H1 Collaboration, C. Adloff et al., The Eur. Phys. J. C19 (2001) pp. 289-311.
12. *Diffraction Jet Production in Deep-Inelastic ep Collisions at HERA*, H1 Collaboration, C. Adloff et al., The Eur. Phys. J. C20 (2001) pp. 29-49.
13. *Searches at HERA for Squarks in R-Parity Violating Supersymmetry*, H1 Collaboration, C. Adloff et al., The Eur. Phys. J. C20 (2001) 4, pp. 639-657.
14. *Deep-Inelastic Inclusive ep Scattering at Low x and a Determination of  $\alpha_s$* , H1 Collaboration, C. Adloff et al., The Eur. Phys. J. C21 (2001) pp. 33-61.
15. *Measurement of Dijet Photoproduction at Small Jet Separation*, H1 Collaboration, C. Adloff et al., The Eur. Phys. J. C24 (2002) 1, pp. 33-41.
16. *Energy Flow and Rapidity Gaps Between Jets in Photoproduction at HERA*, H1 Collaboration, C. Adloff et al., The Eur. Phys. J. C24 (2002) 4, pp. 517-527.
17. *Measurement of Dijet Cross Sections in Photoproduction at HERA*, H1 Collaboration, C. Adloff et al., The Eur. Phys. J. C25 (2002) 1, pp. 13-23.
18. *Inelastic Photoproduction of  $J/\Psi$  Mesons at HERA*, H1 Collaboration, C. Adloff et al., The Eur. Phys. J. C25 (2002) 1, pp. 25-39.
19. *Inelastic Leptoproduction of  $J/\Psi$  Mesons at HERA*, H1 Collaboration, C. Adloff et al., The Eur. Phys. J. C25 (2002) 1, pp. 41-53.
20. *Search for QCD Instanton-Induced Processes in Deep-Inelastic Scattering at HERA*, H1 Collaboration, C. Adloff et al., Eur. Phys. J. C25 (2002) pp. 495-509.
21. *Three-Jet Production in Deep-Inelastic Scattering at HERA*, H1 Collaboration, C. Adloff et al., Phys. Let. B515 (2001) pp. 17-29.
22. *Measurement of Deeply Virtual Compton Scattering at HERA*, H1 Collaboration, C. Adloff et al., Phys. Let. B517 (2001) pp. 47-58.

23. *On the Rise of the Proton Structure Function  $F_2$  Towards Low  $x$ ,*  
H1 Collaboration, C. Adloff et al., Phys. Let. B520 (2001) pp. 183-190.
24.  *$D^{*+-}$  Meson Production in Deep-Inelastic Diffractive Interactions at HERA,*  
H1 Collaboration, C. Adloff et al., Phys. Let. B520 (2001) pp. 191-203.
25. *A Search for Leptoquark Bosons in  $ep$  Collisions at HERA,*  
H1 Collaboration, C. Adloff et al., Phys. Let. B523 (2001) pp. 234-242.
26. *Search for Excited Neutrinos at HERA,*  
H1 Collaboration, C. Adloff et al., Phys. Let. B525 (2002) pp. 9-16.
27. *A Measurement of the  $t$ -Dependence of the Helicity Structure of Diffractive  $\rho$ -Meson Electroproduction at HERA,*  
H1 Collaboration, C. Adloff et al., Phys. Let. B539 (2002) pp. 25-39.
28. *Diffractive Photoproduction of  $\Psi(2S)$  Mesons at HERA,*  
H1 Collaboration, C. Adloff et al., Phys. Let. B541 (2002) pp. 251-264.
29. *Measurement of Inclusive Jet Cross-Sections in Deep-Inelastic  $ep$  Scattering at HERA,*  
H1 Collaboration, C. Adloff et al., Phys. Let. B542 (2002) pp. 193-206.
30. *Search for Odderon-Induced Contributions to Exclusive  $\pi^0$  Photoproduction at HERA,*  
H1 Collaboration, C. Adloff et al., Phys. Let. B544 (2002) pp. 35-43.

# Selbständigkeitserklärung

Hiermit erkläre ich, die vorliegende Arbeit selbständig ohne fremde Hilfe verfasst und nur die abgegebene Literatur und Hilfsmittel verwendet zu haben.

Ilya Tsurin  
15.04.03